SYNTHESIS AND ELECTROCHEMICAL STUDIES OF SPINEL TYPE ANODE MATERIALS FOR LITHIUM-ION BATTERIES

A Thesis Submitted to the
Delhi Technological University
In fulfilment of the requirements for the degree of

DOCTOR OF PHILOSOPHY
in
APPLIED PHYSICS

by

ANCHALI JAIN

(2K18/PHD/AP/14)

Under the Supervision of

Dr. Amrish K. Panwar and Dr. Pawan K. Tyagi

Assistant Professor

DEPARTMENT OF APPLIED PHYSICS

DELHI TECHNOLOGICAL UNIVERSITY

DELHI-110042, INDIA

JANUARY 2024

DELHI TECHNOLOGICAL UNIVERSITY
(Govt. of National Capital Territory of Delhi)
Shahbad Daulatpur, Bawana Road, Delhi-110042

DECLARATION

I, Ms. **Anchali Jain**, hereby certify that the thesis entitled **“Synthesis And Electrochemical Studies of Spinel Type Anode Materials For Lithium-Ion Batteries”** submitted in the fulfilment of the requirements for the award of the degree of Doctor of Philosophy is an authentic record of my research work carried out under the supervision of **Dr. Amrish K. Panwar** and **Dr. Pawan K. Tyagi**. This work in the same form or any other form has not been submitted by me or anyone else earlier for any purpose. Any material borrowed or referred to is duly acknowledged.

Date:
Place: DTU, Delhi

Anchali Jain
(Reg. No. : 2K18/PhD/AP/14)

DELHI TECHNOLOGICAL UNIVERSITY

(Govt. of National Capital Territory of Delhi)
Shahbad Daulatpur, Bawana Road, Delhi-110042

CERTIFICATE

This is to certify that the thesis entitled **“Synthesis And Electrochemical Studies Of Spinel Type Anode Materials For Lithium-Ion Batteries”** with registration number **2K18/PhD/AP/14** being submitted by **Ms. Anchali Jain** to Delhi Technological University India, for the award of the degree of **“Doctor of Philosophy”** is based on the original research work under the supervision of Dr. Amrish K. Panwar and joint supervision of Dr. Pawan K. Tyagi, Department of Applied Physics, Delhi Technological University India. It is further certified that the work embodied in this thesis has not been submitted partially or fully to any other University/Institution for the award of any degree or diploma.

Anchali Jain
(Registration No.: 2K18/PhD/AP/14)

This is certified that the above statement made by the candidate is correct to the best of our knowledge.

Dr. Amrish K. Panwar	**Dr. Pawan K. Tyagi**	**Submitted Through:**
(Supervisor)	(Joint Supervisor)	Prof. A.S. Rao
Assistant Professor	Assistant Professor	Head of Department
Department of Applied Physics	Department of Applied Physics	Department of Applied Physics
Delhi Technological University	Delhi Technological University	Delhi Technological University
Delhi India	Delhi India	Delhi India

Dedicated to….

My beloved family

ACKNOWLEDGEMENTS

This thesis is the result of about five years of work in which I have been supported by many people. It is a pleasant aspect that god has allowed me to express my gratitude for all of them.

First of all, I would like to express my greatest gratitude to my supervisor **Dr. Amrish K. Panwar** for his timely guidance and continued encouragement for the fulfillment of the research work. With great pleasure, I express my heartfelt thankfulness for his patience, advice, fruitful discussions, frequent suggestions, and precious time he spared for me throughout the period of research. I am highly thankful to **Dr. Pawan K. Tyagi, Joint Supervisor**, for his suggestions and support during my research work.

I am highly thankful to **Prof. A.S. Rao, Head of Department, Applied Physics, DTU** for his support of my research work and for providing me with the necessary environment to work in the department. My heartfelt recognition to **Prof. S.C. Sharma**, DRC chairman, and **Prof. Rinku Sharma**, former Head, Department of Applied Physics, and current Dean (PG) DTU for their valuable academic help and suggestions. I am very thankful for the suggestions and support from **Dr. M.S. Mehata** and other faculty members of the Department of Applied Physics. I sincerely thank all non-teaching staff of the Department of Applied Physics for their cooperation and moral support during my research.

Besides this, I am very thankful for the kind support and continuous motivation from my seniors and Ph.D. colleagues**, Dr. Abhishek Bhardwaj, Dr. Snigdha Sharma, Ms. Shivangi Rajput, Mr. Sharad Singh Jadaun, Mr. Rahul Kundra, Mr. Naveen, and**

Mr. Anurag who helped me throughout my research work. I am sincerely thankful to my sister **Dr. Shipra Jain** and my seniors **Dr. Rakesh Saroha, and Dr. Lucky Krishnia** for their helpful discussion to carry out my research work. I am also thankful to the people of the Research Gate community for sparing time and answering solutions to my problems. I gratefully acknowledge the facility support provided by the Lithium-ion Battery Lab at Delhi Technological University for providing me with facilities to carry out my research work.

I am indebted to my parents for everything that they have given me throughout my career. I especially thank my mother **Mrs. Sunita Jain** who always supported me through my best and worst of times. I want to thank my in-laws for their continuous support, encouragement, and timely help throughout my research work. I am blessed to have my husband **Mr. Ashish Jain** who is always there when I need a light in the dark. His continuous understanding and words of encouragement make my dream come true.

Finally, I thank all those who helped and supported me. Thank you so much!

Date: **(Anchali Jain)**

ABSTRACT

With the advancement in technology, the emission of greenhouse gases as well as the depletion of natural resources is escalating and imparting worse effects on the environment. Therefore, today the major concern is how to preserve natural resources. One of the ways is to shift towards renewable, clean, and non-polluted resources using energy storage and conversion technologies such as solar cells, rechargeable batteries, super-capacitors, and many more. Rechargeable batteries are one of the advancing and rapidly growing technology. Moreover, the development of electronic devices such as laptops, iPads, and mobile phones and transportation industries like electric vehicles (EVs), and hybrid electric vehicles (HEVs), are innovating. All these sectors need good storage and conversion devices with high energy density, high power density, durability, and environmental friendliness. Among the energy storage devices, Lithium-ion batteries (LIBs) are fulfilling the demand for renewable and non-renewable energy resources.

The development of LIBs has been started in 1990-1991 with graphite as an anode and oxide-based ($LiCoO_2$) as cathode materials. Till now, in commercialized batteries, graphite has been used as an anode electrode, but still, there is a need to improve the limiting properties of graphite and develop alternative materials. Since the graphitic anode has several disadvantages such as volume expansion (~10%), unstable at high temperatures, and formation of dendrites at higher current rates which restricts its high-power application and escalates the safety issues of LIBs. Recently, Ti-based spinel materials such as $Li_2ZnTi_3O_8$ and other spinel-type transition metal oxides such as $NiMn_2O_4$ have been analyzed as alternative anodes for LIBs. Hence, the research work

reported in this thesis mainly focuses on the synthesis, physicochemical characterizations, and electrochemical analysis of Ti-based and transitional metal oxide-type anode materials.

The research conducted within the thesis framework demonstrates that spinel-type anode material from the Ti-based family, Lithium Zinc Titanate ($Li_2ZnTi_3O_8$), and AB_2O_4 type, Nickel Manganese Oxides ($NiMn_2O_4$) are promising alternate as anode materials in LIBs. The low-cost and facile synthesis routes are used to optimize the structural and morphological properties which leads to stable and advanced anode materials with superior electrochemical performance. These proposed anode materials have the capability to replace the commercialized materials in LIBs.

The results of the current research work have been divided into seven chapters with the following brief details:

Chapter 1 includes the introduction of rechargeable batteries and an overview of Lithium-ion batteries (LIBs) with an explanation of different types of anode materials explored for LIBs. In this chapter, a literature review of spinel-type materials specifically $Li_2ZnTi_3O_8$ and $NiMn_2O_4$ has been described as alternate anode materials for this research work.

Chapter 2 contains the experimental details such as synthesis routes and characterization techniques used in this research work. Synthesis of pristine $Li_2ZnTi_3O_8$, pristine $NiMn_2O_4$, Cr-doped $Li_2ZnTi_3O_8$, MoS_2, and $NiMn_2O_4$-$NiMnO_3$@MoS_2 samples using solid-state, sol-gel and hydrothermal methods have been attempted in this study. This chapter includes a detailed analysis and experimental conditions of the characterization techniques used such as XRD, SEM, TEM, EDX,

TGA, XPS, and A.C./D.C. conductivities. The preparation of electrodes and coin-cell fabrication followed by detailed parameters used for electrochemical characterizations such as Electrochemical Impedance Spectroscopy (EIS), Cyclic Voltammetry (CV), Galvanostatic Charge-Discharge (GCD), and rate performance testing are also reported.

Chapter 3 includes the observed physicochemical and electrochemical results of both pristine $Li_2ZnTi_3O_8$ (LZTO), and $NiMn_2O_4$ (NMO). Both of these spinel-type materials have been prepared using a simple and facile solid-state reaction route followed by calcination at high temperatures in the air atmosphere. XRD results confirm the proper phase of LZTO and NMO is formed with cubic spinel structures showing $P4_332$ and Fd3m space group respectively. Morphological studies are carried out by scanning electron microscope and energy dispersive X-rays, revealing the irregular shape particles and uniform distribution of elements respectively. Conductivity measurements indicate that the LZTO, samples of NMO calcined at 700 ºC and 800 ºC (NMO_700, and NMO_800) attain the conductivity of the order of 10^{-5}, 10^{-7}, and 10^{-6} S/mm respectively. Electrochemical characterizations such as CV, EIS, and GCD depict the potential of both materials as alternative anodes.

Chapter 4 describes the effect on the electrical and cycling performance of $NiMn_2O_4$ (NMO) hexagonal-shaped nanoparticles synthesized using different synthesis routes such as solid-state and sol-gel with varied calcination temperatures. XRD results confirm the highly crystalline cubic spinel structure with zero impurities for all samples, except NMOS_700, which indicates the presence of a slight $NiMnO_3$ phase. Morphological results by SEM and TEM micrographs confirm the formation of hexagonal shape particles of size less than <0.5μm. Electrical measurements depict the

strong dependence of conductivities (σ_{AC} and σ_{DC}) on grain size, grain boundary, and operating temperature. All the samples exhibit conductivities between 10^{-7} - 10^{-3} S/mm with the varied calcination temperature. Electrochemical performances are studied using EIS, CV, and GCD profiles. Sample NMOB_700 and NMOB_800 exhibit the initial discharging capacity of 1104 mAh g^{-1} and 1188 mAh g^{-1} at 100 mA g^{-1} current density. All the samples exhibit above 98% columbic efficiency after two initial cycles and show the reversible nature of $NiMn_2O_4$ and excellent cyclability. The electrochemical results confirm that preparation methods and calcination temperature greatly impact the grain properties of materials.

Chapter 5 deals with the effect of Cr-doping on the $Li_2ZnTi_3O_8$ (LZTO) anode to enhance the electrochemical properties of LIBs. Cr-doped and undoped lithium zinc titanate, $Li_2ZnCr_xTi_{3-x}O_8$ (x =0, 0.1, 0.3, 0.5) has been prepared using a solid-state ball-milling route followed by calcination in the air atmosphere. The cubic spinel structure with the $P4_332$ space group is confirmed through X-ray Diffraction (XRD) for all compositions indicating doping of Cr^{3+} does not cause any changes within the lattice. SEM and TEM revealed the formation of polyhedron-shaped spherical facets in the sub-micron to the nanometer range. The particle size reduces towards the nanometer range as the amount of Cr doping increases and it also decreases the agglomeration of particles. Sample $Li_2ZnCr_{0.3}Ti_{2.7}O_8$ doped with Cr content 0.3 displays higher discharge capacity, better cyclability, and lower polarization among all other Cr-doped samples. $Li_2ZnCr_{0.3}Ti_{2.7}O_8$ delivered excellent rate performances attaining capacities of 251.73±4, 184.34±5, 157.42±5, and 119.03±4 mAh g^{-1} at 0.1C, 0.5C, 1C, and 2C, respectively which is ~10-18% higher than the pristine LZTO sample.

Chapter 6 deals with the synthesis of MoS_2, and $NiMn_2O_4$-$NiMnO_3$@MoS_2 composites using the hydrothermal method and wet chemical mixing. Physicochemical properties such as phase, morphology, and distribution of elements are confirmed using XRD, SEM, and EDX respectively. Electrochemical properties are analyzed using CV, EIS, and GCD analysis. Firstly, MoS_2 is prepared using the hydrothermal method, and its electrochemical properties are studied in brief. In the second section, a composite of $NiMn_2O_4$ is prepared with MoS_2. In the MoS_2 type of composite, the layered structure of MoS_2 provides intercalation of lithium ions without any major volume expansion of $NiMn_2O_4$-$NiMnO_3$ material prepared at 80 ºC using simple and facile wet chemical mixing. Furthermore, NMO nanoparticles occupy the spaces between the MoS_2 nanosheets making both faces accessible to electrolyte penetration. The resulting composite material displayed a stable cyclic voltammogram profile and discharge capacity of 361.54 mAh g^{-1} even after 200 cycles at the current density of 500 mA g^{-1}.

Chapter 7 includes the conclusion and summary of the work done in this research work. The results of the optimized samples have been mentioned in this section. This section also includes the outline of the future scope of the present investigation.

LIST OF PUBLICATIONS

- **Anchali Jain,** Amrish K. Panwar, Pawan K. Tyagi, *"Effect of Cr doping on $Li_2ZnTi_3O_8$ as alternative anode material to enhance electrochemical properties of lithium-ion batteries",* **Journal of Applied Physics A: Materials Science & Processing**, 128, 302, (2022)
- **Anchali Jain,** Amrish K. Panwar, Pawan K. Tyagi, *"Synthesis, characterization, and electrochemical investigation of citric-acid assisted nickel manganese oxide as anode material",* **MRS Advances,** 7, 584-590, (2022)
- **Anchali Jain,** Amrish K. Panwar, Pawan K. Tyagi *"Tuning the electrical and cycling performance of nickel manganese oxide hexagonal-shaped particles via preparation routes for Lithium-ion Batteries"*, **Journal of Physics D: Applied Physics,** 56, 385501, (2023)
- **Anchali Jain,** Amrish K. Panwar, Pawan K. Tyagi, "*Preparation of $NiMn_2O_4$-$NiMnO_3$@MoS_2 nano-composites with enhanced electrochemical performances for Lithium-ion Batteries"*, **Indian Journal of Engineering and Material Sciences,** 30, 689-693, (2023)
- **Anchali Jain,** Amrish K. Panwar, Shivangi Rajput, Seema Singh, Mukul Pastor, *"Electrochemical Studies of hydrothermally synthesized mixed-phase MoS_2 nano-flowers for Lithium-ion Batteries"* (to be communicated)

Conference Attended

- **Anchali Jain,** Amrish K. Panwar, Pawan K. Tyagi, *"Structural, Morphological, and Electrochemical Studies of Complex Spinal titanate* $Li_2ZnTi_3O_8$*"*, **Poster Presented** at the International Conference on Atomic, Molecular, Optical & Nano Physics with Applications **(CAMNP-2019), Springer Proceedings in Physics 271 (2022)**.
- **Anchali Jain,** Amrish K. Panwar, Pawan K. Tyagi, *"Synthesis, characterization, and electrochemical investigation of citric-acid assisted nickel manganese oxide as anode material"* **Oral Presentation** at the International Conference on Advances in Smart Materials & Emerging Technologies **(ASMET-2021)**.
- **Anchali Jain,** Amrish K. Panwar, Pawan K. Tyagi *"Preparation of* $NiMn_2O_4$*-*$NiMnO_3@MoS_2$ *nano-composites with enhanced electrochemical performances for Lithium-ion Batteries"* **Oral Presentation** at the International Conference on Advanced Materials For Emerging Technologies **(ICAMET 2023)**.

Proceedings/Book Chapter

- **Anchali Jain,** Amrish K. Panwar, Pawan K. Tyagi, *"Structural, Morphological, and Electrochemical Studies of Complex Spinal titanate* $Li_2ZnTi_3O_8$*"*, Proceedings of the International Conference on Atomic, Molecular, Optical & Nano Physics with Applications **(CAMNP-2019), Springer Proceedings in Physics 271 (2022)**.

LIST OF FIGURES

LIST OF TABLES

TABLE OF CONTENTS

Chapter 1

Introduction and Literature Review

This chapter includes the introduction and literature review of Lithium-ion Batteries (LIBs), specifically focussed on the types of anode materials developed and used in this research work. The classification of various types of developed anode materials has been reported. Among these developed anode materials, the spinel-type structure shows potential as an alternative anode material. Therefore, an extensive literature review has been carried out for the spinel class of anode materials, especially for the spinel oxides such as $Li_2ZnTi_3O_8$ and $NiMn_2O_4$, since these are considered potential anode materials in this investigation.

1. Introduction and Literature Review

1.1 Background

The global energy consumption is increasing day by day and limited natural resources are depleting with ease of energy utilization. Renewable energy resources such as solar, wind, bio, tidal, geothermal, and many others are being developed to replace conventional sources based on fossil fuels [1-4]. Hence, energy storage devices are emerging solutions in the upcoming technologies to store the energy extracted by renewable energy sources. There are numerous types of energy storage and conversion devices such as batteries, solar cells, supercapacitors, etc. which convert chemical energy into electric energy [5-6]. Among them, batteries prove to be a key component in the electronics as well as transportation industries [1-5]. Nowadays, rechargeable batteries have been considerably incorporated into multiple applications starting from small-scale portable to large-scale energy storage devices such as the electric vehicles (EVs) sector to reduce CO_2 emissions as well as future concerns of global warming [1-6].

Among the existing rechargeable batteries technologies such as lead-acid, Nickel-Cadmium, Nickel-metal hydride, lithium-ion, sodium-ion, etc. have been used from their application point of view [6]–[8]. In these rechargeable battery systems, lithium-ion batteries (LIBs) are extensively studied because of their advantages over other battery systems. The technical battery parameters such as voltage, theoretical capacity, experimental value of specific energy, energy density, and power density for different battery systems are presented in Table 1.1 [6]. From Table 1.1, it is visible that among all rechargeable (secondary) batteries, LIBs attain the highest voltage, energy density, and power density which makes them suitable for industrial as well as transportation applications [6].

Table 1.1 The voltage, theoretical, and experimental values of specific energy and energy densities for the different rechargeable battery systems.

Battery Technology	Nominal Voltage (V)	Theoretical gravimetric specific energy (M J / Kg)	Experimental gravimetric specific energy (M J / Kg)	Experimental energy density (J / m^3)
Pb/acid	2.1	252	35	70
Ni/Cd	1.3	244	35	100
Ni/MH	1.3	240	75	240
Na/S	2.1	792	170	345
$Na/NiCl_2$ (ZEBRA)	2.6	787	115	190
Lithium-ion	4.1	410	150	400

1.2 History and Basics of Lithium-ion Batteries

The discovery of the Li metal as an element was initially reported in, 1817 [9], [10]. The Li metal has the lowest atomic number with the smallest atomic weight (6.95) and electromotive properties [9]. Although Li metal can attain high gravimetric capacity (3860 mAh g^{-1}) as an anode, its disadvantages such as its highly toxic nature, low abundance, dendrite formation, and safety issues make it impossible to use in general batteries [9]–[11]. In the early 1990s, Li-ion batteries came into the light with the development of commercialized $Li_{1-}xCoO_2$/C cells by SONY corporation after many developments in the area [12]–[14]. After the successful innovation of LIBs, the electronics and transportation industry became a fast-growing market due to its low cost, low maintenance, high energy and power densities, longer cycle life, and minimal memory effect over other battery systems [6]–[14]. Especially, in the past decade, the batteries involved in the electric vehicles (EVs) sector are making tremendous progress. Therefore, many studies have been conducted to find the appropriate materials for LIBs.

1.2.1 Working of Lithium-ion Batteries

Figure 1.1 shows the schematic of the working of Lithium-ion Batteries (LIBs) with its charging and discharging process. LIBs are a type of rechargeable (secondary) batteries, consisting of two electrodes (anode, and cathode), an electrolyte, and a separator. The battery system converts electrochemical energy into electrical energy via the flow of electrons outside the circuit and Li^+ ions inside the battery system. As shown in Fig. 1.1, the anode and cathode are dipped in an electrolyte solution and separated by a separator.

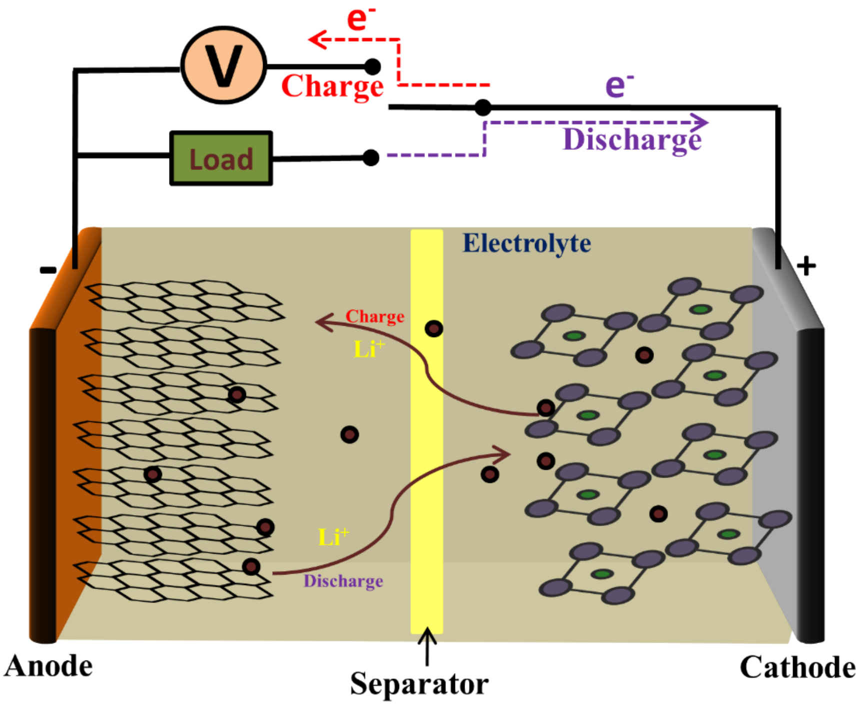

Figure 1.1 Schematic of working LIBs consisting of an anode, and cathode electrodes dipped in an electrolyte solution and separated by a separator.

The process in lithium–ion batteries involves the flow of the lithium-ions between two electrodes moving back and forth through conducting electrolytes repeatedly. During the charging process, the flow of electrons (red dashed lines) and lithium-ions intercalation is from the cathode to the anode when a constant current supply is applied, resulting in the reduction of the cathode as well as oxidation at the anode. This electrochemical process reverses during discharge, lithium-ions de-intercalate from anode to cathode releasing electrons (purple dashed lines) to the external circuit [15]–[17]. The functions of all the components of LIBs are described below [15]–[17]:

- Anode: It is the negative electrode of LIBs at which oxidation occurs by releasing electrons to the external circuit. E.g., graphite, $Li_4Ti_5O_{12,}$ and many more
- Cathode: It is the positive electrode of LIBs at which reduction takes place by gaining electrons from the external circuit. E.g., $LiFe_6PO_4$, $LiCoO_{2,}$ and many more.
- Electrolyte: It is an organic solvent/solid-state material that provides an ionic conduction path between the anode and cathodes of the battery system. E.g., 1 M $LiPF_6$ in EC: DMC with the ratio of 1:1 (by volume) and many more.
- Separator: It is an ionic conductor and has the property to pass ions between both electrodes while it prevents the passage of electrons through it. So, It must be impermeable to electrons that are flowing outside the circuit. E.g., Polyethylene, polypropylene, and many more.

All the components have a significant role in enhancing the capacity (total charge transferred), cyclability (life of the batteries), and performance of LIBs. In this research investigation, the study is focused on the anode materials for LIBs.

1.3 Lithium-ion Batteries Anode Materials and their Classification

In recent years, anode materials have been vigorously studied in terms of longer cyclability, high energy density, lightweight, and variable charging rates. The properties of anodes such as morphology, porosity, and type greatly affect the overall performance of the LIBs system. Hence, the specifications of anode materials for LIBs are as follows [18]–[21]:

1. The anode materials having electrochemical reaction potential close to lithium metal are considered good anode electrodes.
2. To maintain the reversibility of redox reactions in LIBs, there must not be a change in crystal structure during redox reactions.
3. Electronic and ionic conductivity must be high to encourage the fast movement of electrons outside the batteries and higher diffusion of Li^+ within the electrode material.
4. The morphology and structure greatly affect the performance of LIBs. Therefore, the size of active material must be in the submicron–nano range to provide maximum surface area for the interaction of lithium ions.
5. Active electrodes must be dense enough to store a large amount of charge per unit mass.

Therefore, properties of anode materials play a significant role in enhancing the overall electrochemical performance of LIBs. According to the reaction mechanisms, anode materials are classified into three types as depicted in Fig. 1.2 [15], [22].

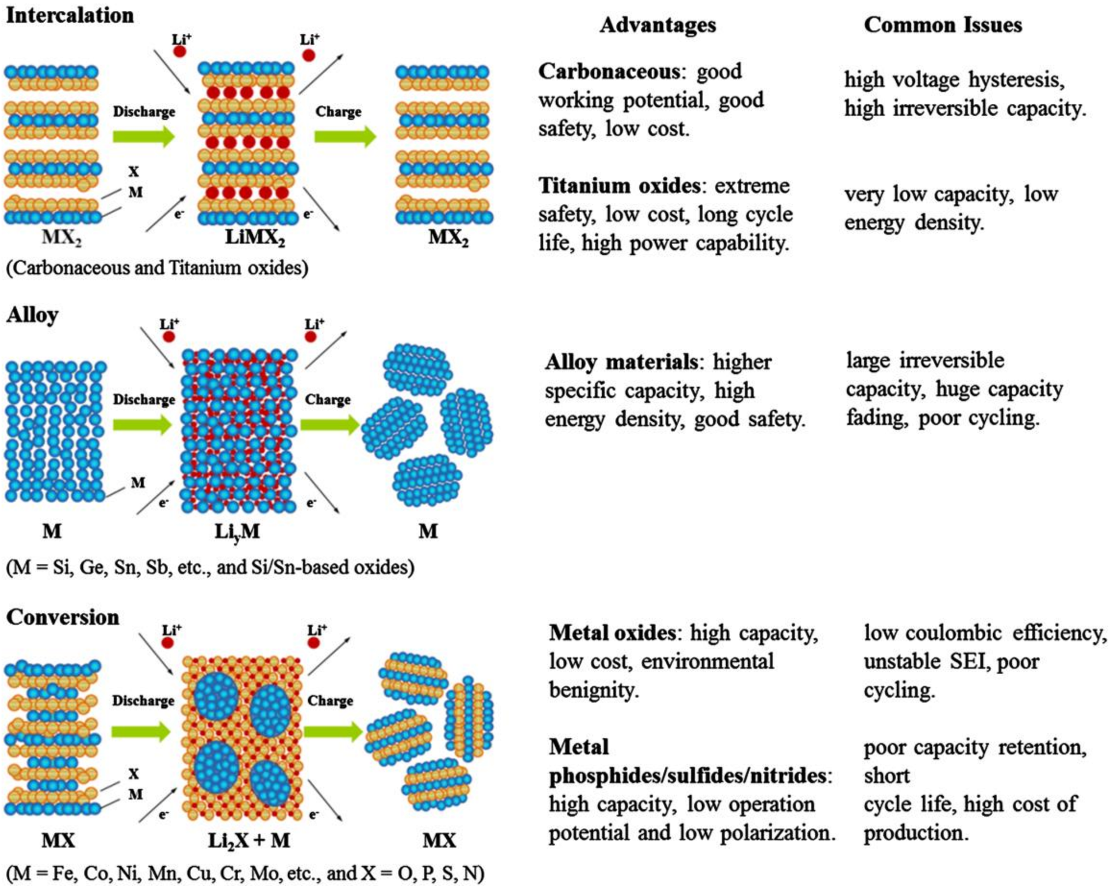

Advantages	Common Issues
Carbonaceous: good working potential, good safety, low cost.	high voltage hysteresis, high irreversible capacity.
Titanium oxides: extreme safety, low cost, long cycle life, high power capability.	very low capacity, low energy density.
Alloy materials: higher specific capacity, high energy density, good safety.	large irreversible capacity, huge capacity fading, poor cycling.
Metal oxides: high capacity, low cost, environmental benignity.	low coulombic efficiency, unstable SEI, poor cycling.
Metal phosphides/sulfides/nitrides: high capacity, low operation potential and low polarization.	poor capacity retention, short cycle life, high cost of production.

Figure 1.2 Schematic of classification of types of anode materials on the basis of lithium storage and their advantages [10].

a) Intercalation (insertion) type: In these types of electrodes transportation of Li^+/e^- is in such a way that they reversibly incorporated into the vacant sites in the host lattice without deteriorating its structure [20], [23]–[26]. That is why in the intercalation mechanism there is minimum volume expansion during redox reactions. Thereby, maintaining the mechanical and electrochemical stability of the electrodes during redox reactions [20], [26]. The anode materials like graphite, $Li_4Ti_5O_{12}$, $Li_2ZnTi_3O_8$, etc. are of intercalation/insertion type electrode material.

b) Alloy: In these types of anode materials, Li-ion is inserted in the crystal structure or reactant phase to form Li-M alloy (where M is Si, Ge, Sn, Bi, etc.) [25]. These types of materials have high specific capacity and moderate operating potentials *vs.* Li/Li^+ but the high volumetric expansion leads to poor rate capability and cyclability as well [25], [27]. Hence, the reaction for alloying and de-alloying can be expressed as equation (1.1):

$$\mathrm{Li} + x\mathrm{M} \leftrightarrow \mathrm{LiM}_x \tag{1.1}$$

where M is Si, Ge, Sn, Bi, etc.

c) Conversion: In conversion-based electrodes, Li^+ fully reduces the host lattice (generally transition metal) reversibly to form nano-domains dispersed in the Li_2O matrix satisfying the following equation (1.2):

$$\mathrm{M}_x\mathrm{X}_y + 2\mathrm{yLi}^+ + 2ye^- \leftrightarrow \mathrm{yLi_2O} + \mathrm{xX} \tag{1.2}$$

where M is transition metals such as Ni, Mn, and Mg, etc. and X can be O, S, and F, etc. [26]–[31]. These reaction-based anode materials attain high capacity but poor kinetics of charge-discharge process is one of the drawbacks [26]–[32]. The materials such as transition metal oxides (CuO, NiO, etc.), metal sulfides, phosphides, and nitrides are of conversion type anode materials.

Table 1.2 summarizes the theoretical capacities of various anode materials category-wise with advantages and problems.

Table 1.2 Standard anode materials used for LIBs [33].

Working anode materials	**Theoretical capacity (mAh g^{-1})**	**Advantages**	**Drawbacks**
Insertion/de-insertion materials **Carbonaceous** Hard carbons CNTS Graphene	200-600 1116 780/1116	Stable working voltage Cheap Good safety	Poor coulombic efficiency Large voltage hysteresis High irreversible capacity
Titanium oxides $Li_4Ti_5O_{12}$ TiO_2	175 330	Excellent cycle life Highly safe Low priced High power capability	Poor capacity Poor energy density
Alloy/de-alloy materials Silicon Germanium Tin Antimony Tin oxide SiO	4212 1624 993 660 790 1600	Higher specific capacities and energy density Eco-friendly	Large irreversible capacity Huge capacity fading Poor cycle performance
Conversion Materials Metal oxides (Fe_2O_3, CuO, NiO, Mn_2O, etc.)	500-1200	High Capacity High energy	Poor coulombic efficiency

Metal phosphides/sulfides/nitrides (MXy: M = Fe, Mn, Ni, etc. and X= P, S, N)	500-1800	Low cost Environmentally compatibility High specific capacity Low operating potential and low polarization than counter oxides	Formation of Solid Electrolyte Interface (SEI) layer Large voltage hysteresis Poor cycle life Poor capacity retention Short cycle life High manufacturing cost

1.4 Carbonaceous Anodes

Carbon-based materials such as graphite, graphene, hard carbon, etc. are promising electrode materials due to their unique physicochemical properties [34]–[38]. For many years graphite has been used as a commercial anode because of its abundance, cheap rate, structure stability, excellent Li^+ reversibility during redox reactions, good theoretical capacity (~372 mAh g^{-1}), good electrical (~10^{-4} S/cm) and thermal (~3000 W/mK) conductivities [39]–[42]. Graphite is a hexagonal structure in which carbon atoms are orderly arranged in a hexagon in the form of graphene layers. Therefore for a typical LIBs system, one Li^+ reversibly intercalates/de-intercalate with six carbon atoms (graphite) forming Li_xC_n (here n = 6) alloys satisfying the following equation (1.3) [15]:

$$\mathrm{C} + x\mathrm{Li} + x\mathrm{e}^- \leftrightarrow \mathrm{Li}_x\mathrm{C}_6 \tag{1.3}$$

However, due to the limited theoretical capacity and low lithiation potential of graphite (0.1 - 0.2 V *vs.* Li/Li^+), two major issues are likely to occur in LIBs. One is its low potential which is closer to the lithium stripping voltage and leads to the formation of lithium dendrite growth which raises safety issues for lithium-ion batteries, specifically at higher current rates [43]–[45]. Another drawback of this very low potential is that it leads to the solid electrolyte interphase (SEI) layer formation on the surface of the graphite which reduces the cycling performance and coloumbic efficiency and degrades the performance of LIBs.

Due to these drawbacks, new materials have been explored by researchers to replace them. Therefore, in this research study, spinel-type anode materials are explored for the improvement in the electrochemical performance of LIBs in terms of cycling stability as well as safety issues.

1.5 Spinel-type electrodes

In general, the spinel-type structure is generalized by the formula $A[B_2]X_4$, which crystallizes in a cubic closed-pack lattice system. Here, X are anions (mainly oxygen) and A and B are divalent (A^{2+}/B^{2+}), trivalent (A^{3+}/B^{3+}), or tetravalent (A^{4+}/B^{4+}) cations like nickel, manganese, titanium, etc. In the structural unit cell, 1/8th of the tetrahedral sites (8a) occupies by the 'A' site and 1/2th of the octahedral sites (16d) occupies by the 'B' site cations in the lattice. The remaining tetrahedral (8b, 48f) and octahedral sites (16c) form interstitial sites in the structure [46]–[48].

The spinel-type transition metal oxides (TMO) based electrodes such as $NiMn_2O_4$, $ZnFe_2O_4$, MnO_2, NiO, Fe_2O_3, etc. belong to the spinel family category and show conversion reaction. However, titanate-based TMOs such as $Li_4Ti_5O_{12}$, $Li_2ZnTi_3O_8$, TiO_2 etc. exhibit spinel structure also and show intercalation mechanism. Therefore, spinel-type TMO can be classified into the following two types of reaction mechanisms [23], [26], [27], [49]:

(1) Conversion reaction: $M_xO_y + 2yLi^+ + 2ye^- \leftrightarrow yLi_2O + xM$ and

(2) Intercalation/deintercalation reaction: $M_xO_y + nLi^+ + ne^- \leftrightarrow Li_nM_xO_y + xM$.

Hence, In this study, spinel-type electrodes based on both reactions mentioned above as $NiMn_2O_4$ and $Li_2ZnTi_3O_8$, respectively, are focused. Therefore, an extensive literature review has been explored for both the anode materials for LIBs and described below.

1.6 Literature Review - Material of Choice

Lithium-ion batteries performance depends on the material structure, properties, morphology as well as synthesis routes. Here, in this literature review advantages, disadvantages, structural, and varied synthesis routes of Titanate-based, $Li_2ZnTi_3O_8$, and mixed metal oxide, $NiMn_2O_4$ anodes has been explored in comparison to other spinel-type anode materials.

1.6.1 $Li_2ZnTi_3O_8$

Over the last few years, researchers are exploring titanate-based anodes like TiO_2, $Li_4Ti_5O_{12}$, $Li_2ZnTi_3O_8$, etc. because of their negligible volume expansion (2-3%) during redox reactions, their variable range of operating potential (1-3 V vs. Li^+/Li), non-toxic nature, low cost, and thermal stability which offers long cycle life and better safety for LIBs [50]–[53]. Among these anodes, $Li_4Ti_5O_{12}$ (LTO) has been explored due to its high operating potential, ~1.55V, which overcomes the safety issues like dendritic growth and SEI formation that occur in graphitic anode [54]–[56]. However, its poor theoretical capacity (~175 mAh g^{-1}), poor electronic conductivity (<10^{-13} S cm^{-1}), and high potential limit its applications towards high power applications [57]–[59].

Here, another class of anode material, $Li_{1+x}[M_2]O_4$ (M=Ti, V, Mn), specifically $Li_2ZnTi_3O_8$ (Lithium Zinc Titanate, LZTO) came into light because of its intermediate voltage plateau (0.5-0.8 V *vs.* Li/Li^+) which is greater than the lowest potential of graphite and lower than high potential of LTO. It avoids the dendrites formation and increases the overall cell voltage. LZTO have relatively high theoretical capacity of 227 mAh g^{-1}, than LTO and maintain same structural stability during charging-discharging process enhancing the energy and power densities while upholding the safety concerns. Furthermore, the negligible decomposition of SEI layer during cycling, non-toxicity, economical and environment friendliness makes LZTO a potential alternative anode for LIBs [60]–[65].

Thus, a new class of ternary lithium spinels, $Li_2MM_3'O_8$ (M= Cu, Zn, Cr, Mn, Mg, and Fe, and M'= Ti and Ge) indicate potential as alternative anode material for LIBs [48]. The $Li_2MM_3'O_8$ spinels are cubic with a space group of $P4_332$. While in the LZTO spinel structure, Li^+ and Ti^{4+} occupy octahedral sites in the ratio of 1:3, and Li^+ and Zn^+ occupy tetrahedral sites in the ratio of 1:1, respectively. Therefore, LZTO can be described by the formula: $(Li_{0.5}Zn_{0.5})_{tet}[Li_{0.5}Ti_{1.5}]_{oct}O_4$, forming a network of the 3D tunnel, providing a multi-channel path for lithium ions insertion and extraction process [66–68]. Despite of these advantages, the 3d-state of titanium with band gap energy of 2-3 eV makes the hindrance to Zn^{2+} located at tetrahedral sites which thereby affects the Li^+ migration. This gives rise to the decrease in LZTO electronic conductivity and diffusivity of Li^+ that limits its practical applications [69]–[72].

Since, LZTO has been prepared using many synthesis techniques as reported in literature and are given below with their advantages and disadvantages.

Table 1.3 Reported synthesis methods and precursors used along with their advantages and disadvantages.

Synthesis Method and reference	**Precursors used**	**Advantages**	**Disadvantages**
Solid-state reaction [61-62], [64], [69], [70], [72]	Zinc acetate, Titanium dioxide, Lithium carbonate	Simple and low-cost method with large scale production & low energy consumption.	Irregular morphology, uncontrollable particle growth and agglomeration in the final product.
Sol-gel synthesis [73]	Zinc acetate, Lithium acetate, Titanium isopropoxide, Titanium butoxide Citric acid	Low synthesis temperature with homogeneous particle distribution good stoichiometry control	High synthesis cost with complexity
Solution combustio [74]	Nitrates of Zinc & Lithium, Titanium source to form its nitrate	The route is easy to control with short heat time and uniform large surface area	Not suitable for mass Production
Molten salt method [74], [75]	Zinc acetate, Lithium hydroxide, Titanium oxide	The time of reaction is fast with control of particle morphology	Proper molten media is difficult to find
Microwave Method [66]	Zinc acetate, Titanium dioxide, Lithium carbonate	Advantage of high-energy radiation and reduces processing times to minute	The size of nanoparticles slight greater with agglomeration

1.6.2 NiMn$_2$O$_4$

TMOs with single metals such as NiO, Co$_3$O$_4$, Mn$_2$O$_3$, etc. show good electrochemical performance due to their multiple oxidation states [76]–[79]. However, they exhibit volume expansion, pulverization, and agglomeration which effects the electronic conductivity, cycling stability, and rate capability of LIBs [76]–[79]. To overcome these drawbacks, one of the best ways is to combine two transition metal oxides to form Mixed-TMOs [80], [81]. The presence of additional material may provide a medium to withstand the volume changes that occur during redox reactions [65-66]. Therefore, another class of spinel-type anode like “AB_2O_4” has been attracted to many researchers as an alternative anode material because of their additional features than traditional TMOs [80]–[82] and are given as;

(i) The presence of two metal elements has variable oxidation states, more active sites, and different expansion coefficients which makes a synergistic effect.

(ii) The complex chemical compositions offer more active material to react with Li ions compared to single metal oxides resulting in higher specific capacities.

(iii) These materials exhibit relatively higher electrical conductivity and lesser activation energy for electron transfer.

(iv) These spinel materials are more environmentally friendly compared to single metal oxides.

Among these AB_2O_4 type spinel, $NiMn_2O_4$ is an emerging spinel-type TMO in which cations occupy tetrahedral and octahedral sites in face-centered cubic (FCC) sublattice [83], [84]. Anion nNi^{2+}, $nMn^{4+,}$ and (2-2n) Mn^{3+} occupy octahedral sites while (1-n) Ni^{2+} and nMn^{2+} ions occupy tetrahedral sites of the lattice [83], [84]. There are many reports of NMO material as a negative temperature coefficient (NTC) [85]–[87], however, there are only few reports regarding its application as an anode for LIBs. Till now, researchers have attempted the synthesis of NMO using limited methods which are tabulated in the Table 1.4:

Table 1.4 Synthesis methods with current density and initial discharge capacity using NMO.

Sample Name	**Synthesis Method & reference**	**Current density**	**Initial discharge capacity**
$NiMn_2O_4$@rGO	Hydrothermal & dipping process [88]	100 mA g^{-1}	1815 mAh g^{-1}
$NiMn_2O_4$	Hydrothermal method [89]	500 mA g^{-1}	1126 mAh g^{-1}
$NiMn_2O_4$/C	Solvothermal method[90]	1000 mA g^{-1}	1617 mAh g^{-1}
Fe-doped $NiMn_2O_4$	Nanocasting method [91]	200 mA g^{-1}	954 mAh g^{-1}
Mesoporous $NiMn_2O_4$	Citric acid-based combustion method [92]	100 mA g^{-1}	983 mAh g^{-1}

Hence, there are various reported methods that indicate excellent results of zero-strain for LZTO and while a few methods to NMO as an anode for LIBs. But still, there is irreversible capacity loss due to the formation of the SEI layer. Therefore, research work is in progress to improve the electrochemical performance using different solutions described below:

(i) Modification in the morphology via varied synthesis routes, which shortens the diffusion path length for Li^+ and improves diffusivity.

(ii) Doping of heterogeneous atoms into tetrahedral/octahedral sites to improve electronic conductivity.

(iii) Coating of different materials on the surface of LZTO/NMO to elude electrolyte interaction and prevent variation in internal resistance and further corrosion.

1.6.3 Coating of materials

Researchers are now focused on increasing or maintaining the structural stability, rate capability, and long cyclability of the anode electrodes. To achieve this, one of the solutions is surface modification of electrode materials. The uniform surface area may lead to more electrochemical reactions and surface/electrolyte reactions resulting in the degradation of the electrodes. Therefore, coating on nano-sized materials either carbon or any other material has many advantages as described in Fig. 1.3. Coating suppresses the unnecessary side reactions with the electrolyte and the cracking of electrodes during the charging-discharging mechanism which increases the rate capability and improves the electrochemical performance of LIBs. Furthermore, the application of coating facilitates more diffusion of Li^+ inside the electrodes thereby enhancing the capacities during the cycling process. The coating can be of two types: either carbon or other materials as described in the section below.

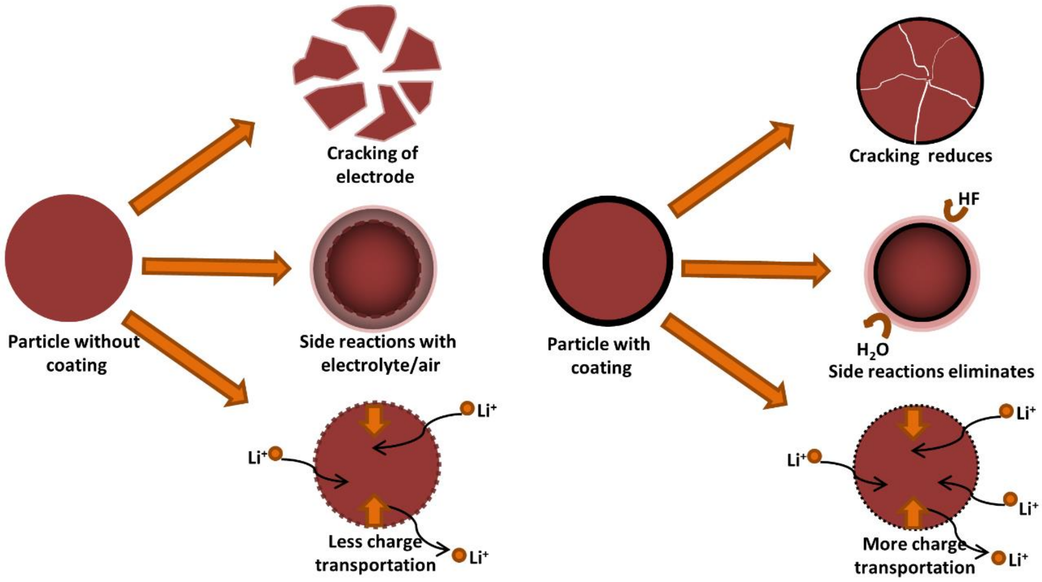

Figure 1.3 Schematic of nanoparticle describing how the coating is advantageous in LIBs.

1.6.3.1 Carbon coating

Coating carbon is among the one of the best approaches to increase the stability and performance of anodes for LIBs. As carbon is in abundance and cheaper than many other materials, it is widely used as a coating agent [62], [70], [93]. Additionally, it has high electronic and ionic conductivity, superior thermal properties, and chemical stability [62], [70], [93]. Furthermore, it also prevents side reactions with the electrolyte during redox reactions thereby resulting an increase the cycle life of electrodes.

Variuos investigations has been attempted on the coating/composites of LZTO material using different carbon sources such as sucrose [62], oxalic acid [62], citric acid [62], phenolic resin [70], alginic acid [94], EDTA [69], fulvic acid [68], β-cyclodextrin [95] and many more.

There are very selected investigation for $NiMn_2O_4$ material coated with carbon using polyacrylonitrile (PAN) [90], and dopamine hydrochloride [83].

1.6.3.2 Coating with Different Materials

Coating with highly conductive material that provide stability between the electrode-electrolyte interfaces have been extensively explored to improve the electrochemical performance of the LIBs. These coating also provides a decrement in polarization and reduction in the charge transfer resistance during redox reactions [60]. Many studies had reported with the varied types of coating as well as composites formation with the LZTO material including $LiCoO_2$ [60], Na_2MoO_4 [96], Lithium magnesium silicate [97], $LiAlO_2$ [72], Li_3PO_4 [98]. However, for $NiMn_2O_4$ spinel, there is only one reported paper with TiO_2 coating [83].

1.6.4 Doping

Another effective strategy to increase the conductivity and electrochemical performance of LZTO/NMO material is doping or substitution. Doping helps in achieving the stability of the structure during the Li^+ interaction and de-intercalation [99]. Additionally, it can also help in accelerating the conductivity of the material resulting better cyclability of the material as an anode. There are many reports of doping of LZTO/NMO materials with different elements such as doping with Ag [99], Al^{3+} [100], Ce^{4+} [101], Nb^{5+} [102], Na [103], Fe [91] etc.

In this research study, spinel type anode materials are explored and hence, synthesize of LZTO and NMO material has been attempted because of their advantages over other materials. Therefore, different material synthesis thechniques, multiple physico-chemial and electrochemical characterizations have been performed to investigate both the materials as anode material.

1.7 Objectives of Research

This investigation is aimed to synthesize alternate anode material for LIBs in place of commercialized graphite material. Hence, the objectives of the present investigation are:

- Synthesis of alternate spinel anode materials such as $Li_2MTi_3O_8$ (where M is Zn, Cr, Co, Fe, Ni, etc.), AMn_2O_4 (where A is Ni, Zn, Cu, etc.), etc. using different synthesis routes such as solid-state method, sol-gel route, urea-assisted auto-combustion method.
- Physico-chemical characterizations of synthesized spinel anodes for structural and morphological analysis using XRD, SEM, EDX, TEM, FTIR, etc., and optimizing the compositions of anodes among different synthesis routes.
- Improvement in the electronic/ionic conductivity of synthesized anode materials on doping/ substitution at anionic or cationic sites with Cr, F, etc elements.
- Enhancement in the electronic/ionic conductivity of synthesized anode materials by the coating of carbon-based materials or other 1D/2D conductive material.
- Electrochemical analysis in terms of Galvanostatic Charge-Discharge (GCD), Cyclic Voltammetry (CV), cyclability, rate performance, and Electrochemical Impedance Spectroscopy (EIS) of synthesized spinel anode materials.

Chapter 2

Experimental and Characterization Techniques

This chapter includes experimental and characterization details used in this study. The overview of synthesis routes of anode materials, electrode materials preparation and fabrication of coin cells for electrochemical testing has been reported. It also includes the theory and working of characterization techniques used in this research work to test the physicochemical and electrochemical performances as an anode.

2.1 Synthesis Techniques

This section includes the various synthesis techniques used to prepare anode materials in this work. Various synthesis routes has been used such as the solid-state reaction route, sol-gel route, and hydrothermal method to prepare the electrode materials. The details of material preparation techniques, and precursors used have been mentioned below.

2.1.1 Mechano-chemical Ball-milling method

The high-energy ball mill method is one of the most widely used in industrial as well as academic R&D laboratories. Due to its simplicity and cost-effectiveness, it is broadly applicable in the synthesis of metal and alloy powders. In this process, mixing and grinding of the precursors are performed at high speed over a long duration of time. After that, as-prepared samples are calcined at high temperatures to get the desired $Li_2ZnTi_3O_8$, and $NiMn_2O_4$ electrode materials. The final product using this method is highly crystalline and attains a small particle size in comparison to other methods. Figure 2.1 shows the schematic of the preparation of samples and equipment used. Pristine $Li_2ZnTi_3O_8$ (LZTO), Cr-doped $Li_2ZnTi_{3-x}Cr_xO_8$ (where x=0.1, 0.2, 0.3, 0.4), and $NiMn_2O_4$ (NMO), were synthesized using mechano-chemical ball-milling method. However, the disadvantage of this method is the high-temperature calcination which increases the crystallite size and irregular particle shape.

All the chemicals used in this research work were of high purity and analytical grade.

2.1.1.1 Preparation of $Li_2ZnTi_3O_8$ (LZTO)

Lithium carbonate (Li_2CO_3), zinc acetate ($Zn(CH_3CO_2)_2.2H_2O$), and titanium dioxide (TiO_2) were used as precursors to prepare pristine LZTO. To prepare Cr-doped LZTO, Chromium oxide (Cr_2O_3) was also used. The stoichiometric amount of all precursors was ball milled for 4 h in the presence of a small quantity of de-ionized water for homogeneous mixing. A 5% excess of lithium source is further added to balance its evaporation at higher temperatures. After mixing, the as-prepared sample was dried at 80 °C for 12 h to remove any H_2O content. The obtained as-prepared dried material was grounded and calcined at 700 °C for 3 h and again treated at 800 °C for another 5 h in air. Lastly, the calcined material was re-grounded and used for further electrode preparation and characterizations.

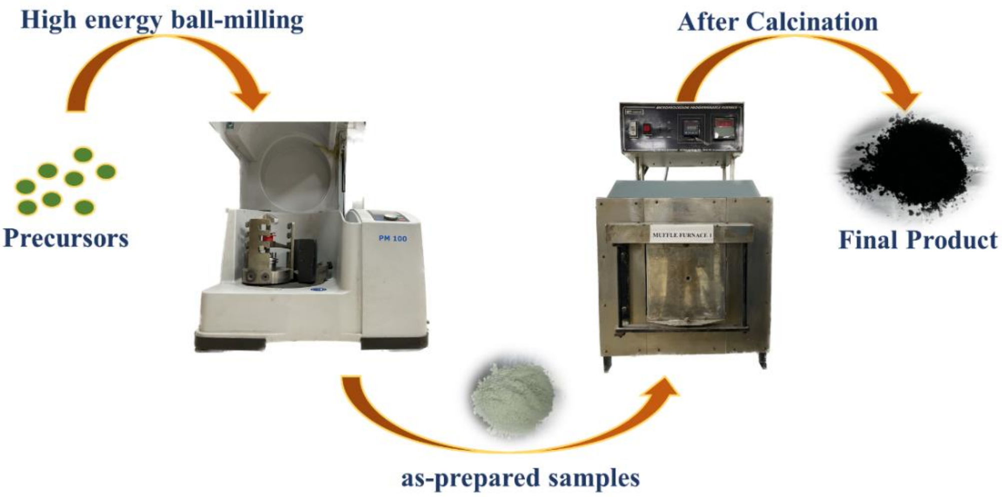

Figure 1.2 Schematic of ball mill method used to prepare pristine $Li_2ZnTi_3O_8$, Cr-doped $Li_2ZnTi_3O_8$, and $NiMn_2O_4$ samples.

2.1.1.2 Preparation of $NiMn_2O_4$ (NMO):

To prepare pristine NMO, a stoichiometric amount of nickel acetate ($Ni(CH_3COO)_2.4H_2O$), and manganese acetate ($Mn(CH_3COO)_2.2H_2O$) was used in the molar ratio of 1:2. The citric acid ($C_6H_8O_7$) was used as a chelating agent keeping in the ratio of 1:1 with metal ions. All these analytical grade precursors were mixed in a high-energy ball mill for 4 h followed by drying at 80 °C to remove any moisture content. After drying, the as-prepared sample was grounded and calcined at two different temperatures of 700 °C and 800 °C for 3 h in an air atmosphere and abbreviated as NMO-700 and NMO-800.

2.1.2 Sol-gel method

Sol-gel method is a wet chemical technique that forms the final product by mixing the atoms/molecule in an aqueous medium. As bond breaking of materials is easy in an aqueous medium in comparison to the solid-state route. Due to this, the temperature required to calcinate the samples is generally lower. However, the shape and size of particles depend on the precursors and solvents used. Figure 2.2 shows the schematic of the synthesis of pristine $NiMn_2O_4$ using the sol-gel route used in this research work.

2.1.2.1 Preparation of $NiMn_2O_4$ (NMO):

Nickel acetate ($Ni(CH_3COO)_2.4H_2O$), manganese acetate ($Mn(CH_3COO)_2.2H_2O$) and citric acid ($C_6H_8O_7$) were mixed in 30 ml de-ionized (DI) water separately under vigorous stirring. Citric acid was used in an equal ratio with metal ions (1:1) as the chelating agent. After the precursors were completely dissolved, both the acetate solutions of nickel acetate and manganese acetate were mixed at a magnetic stirrer for half an hour. Then the citric acid solution was mixed drop by drop with the above acetate solution with continuous stirring for 1 h. Homogeneous mixing of the precursors and citric acid solutions was performed at a temperature of 80 °C. As the solution evaporates slowly, the mixed solution changes its color from soft green to light green during the gelation process and forms a thin gel. Hence, the observed thin gel was dried at 100 °C in a vacuum oven for overnight. The light green fluffy of as-prepared NMO was collected, then it was lightly ground, and further calcined at 700 °C and 800 °C for 3 h in the muffle furnace, and the samples are named NMOS_700 and NMOS_800, respectively. The resultant black-colored powdered samples were collected after calcination and further characterized for anode materials.

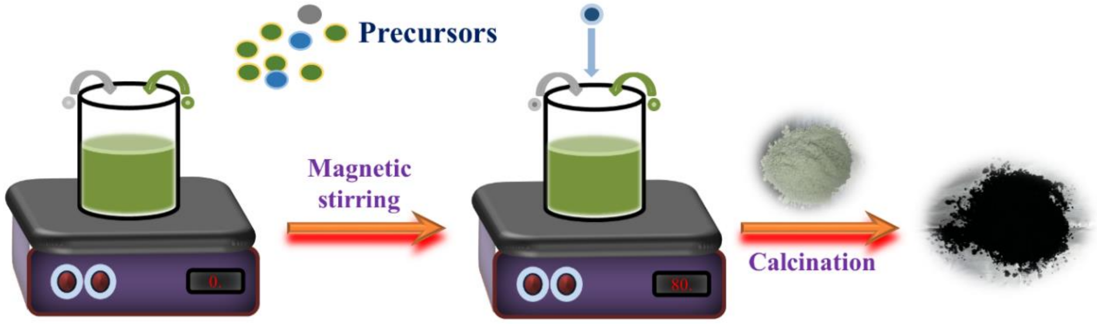

Figure 2.2 Schematic of the sol-gel method used to prepare as-prepared pristine $Li_2ZnTi_3O_8$ and $NiMn_2O_4$ samples.

2.1.3 Hydrothermal method

The hydrothermal method is a wet chemical route in which precursors are mixed in an aqueous medium and transferred in the Teflon-coated flask. That flask was sealed in the stainless-steel autoclave and heated at a particular temperature and time under pressure. In this method, the morphology of the final product can be varied by optimizing the solvent and precursors used. Furthermore, the temperature and operating time has also a vital effect on the morphology of the synthesized materials. In this study, synthesis of MoS_2 nanosheets has also been performed (as shown in Fig. 2.3) using a one-step hydrothermal method which was further used for coating/composite with $NiMn_2O_4$.

2.1.3.1 Preparation of MoS_2

Sheets of 2H/1T type MoS_2 was been prepared using the simple one-step hydrothermal method as shown in Fig. 2.3. Sodium molybdate (Na_2MoO_4) and thiourea (CH_4N_2S) were used as starting materials in a ratio of 1:4 without any further purification. Na_2MoO_4 and CH_4N_2S were separately mixed with 30 ml deionized (DI) water at room temperature for 30 mins. After that, both of the mixtures were mixed for 1 h for the homogeneous solution and transferred to a Teflon-lined stainless steel autoclave for 24 h at 200 ºC. After cooling till room temperature, the black solution was washed with DI and ethanol for four times to remove any impurities and dried at 80 ºC overnight. The as-prepared black sample was collected and used for further characterization.

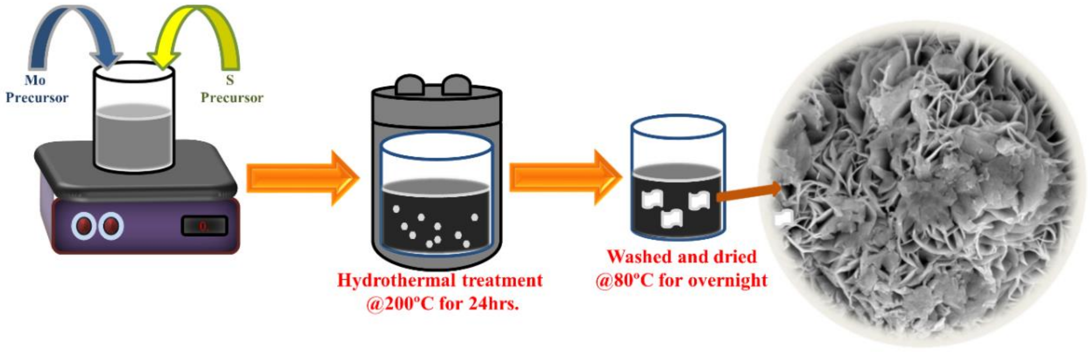

Figure 2.3 Schematic of the preparation of MoS_2 using the hydrothermal method.

2.2 Characterization Techniques

To investigate the properties of as-synthesized materials, various characterizations techniques have been used for structural, morphological, surface, electrical, and electrochemical studies. This section includes the basics, working, and overview of various characterizations. All the techniques used in this research work have been described in Fig. 2.4.

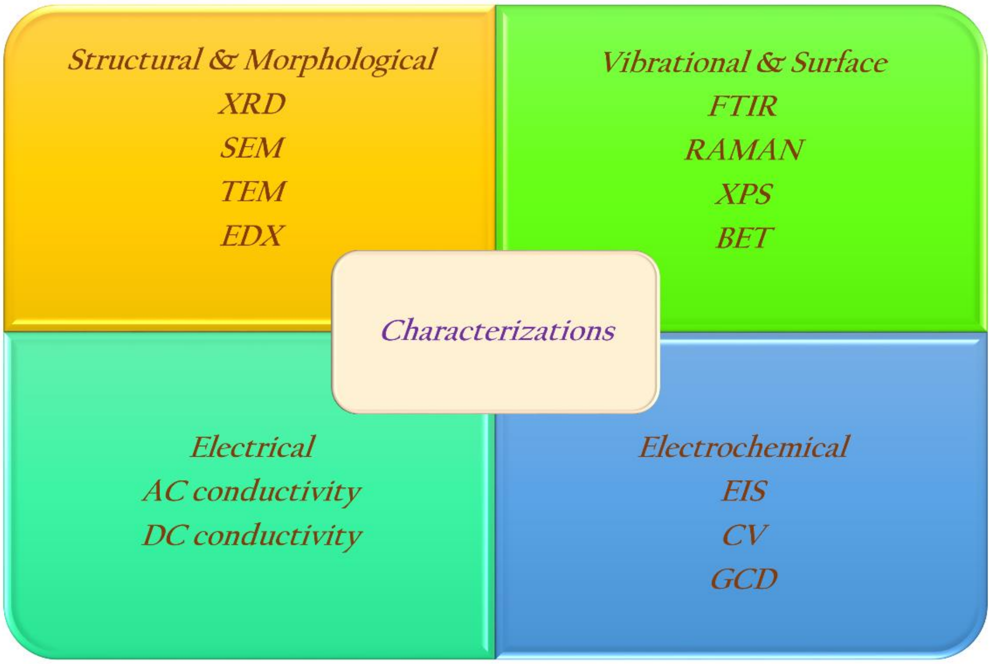

Figure 2.4 Schematic of various types of characterizations used in this research work.

2.2.1 Thermal Characterization

2.2.1.1 Thermogravimetric and Differential Thermal Analysis (TGA and DTA)

Thermogravimetric analysis (TGA) and differential thermal analysis (DTA) is an important thermal characterization that measures the change in mass of the sample is measured as the function of temperature over time. TGA provides the physical information about the measured sample such as phase transitions, absorption, purity, decomposition temperature, and adsorption. Additionally, chemical phenomena such as oxidation, reduction, or decomposition can also be studied in TGA. In the TGA method, a sample is placed on thermobalance and weight/mass of the samples is continuously measured with the rise in temperature in the presence of air or other gaseous environment. The mass of the samples is recorded throughout the experiments.

However, in case of DTA, the temperature difference between the sample and a reference material is recorded against temperature or time. It provides details about the exothermic or endothermic reactions, crystallization, melting and sublimation points of materials. In the present study, Perkin Elmer makes TGA analyzer (Model: TGA 4000) was used. All the as-prepared samples were recorded at 10 ºC/min heating rate up to a temperature of 900 ºC in air.

2.2.2 Structural and Morphological Characterizations

2.2.2.1 X-ray Diffraction (XRD)

X-Ray Diffraction (XRD) is a structural characterization technique used to study crystalline solids which are arranged in the regular order of atoms or molecules. When X-rays of radiation, $\mathrm{Cuk}_{\alpha1}$, of wavelength, 1.540 Å are incident on the crystal lattice, it causes the scattering of waves which are added or cancel out each other constructively or destructively, respectively, in specific directions. From these constructive and destructive interference lattice structures, d-spacing, and arrangement of atoms or molecules can be studied. These directions could be found using Bragg's law:

$$n\lambda = 2dsin\theta \tag{2.1}$$

where n is any integer, λ is the beam wavelength used, d is the interplanar spacing, and θ is the incident angle as depicted in Fig. 2.5.

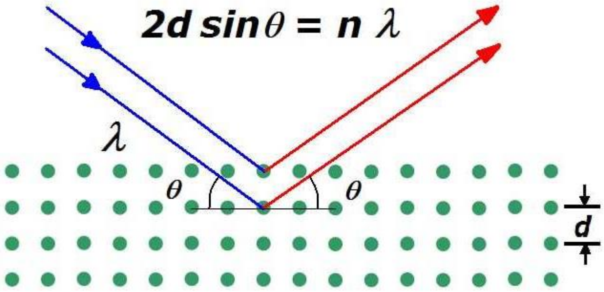

Figure 2.5 Schematic of X-ray diffraction using Bragg's law. Lattice planes are separated by interplanar spacing, d and incident X-rays are diffracted at an angle, θ.

The powdered samples were placed on Rigaku's Ultima IV-Powder X-ray Diffractometer and CuKα_1 of wavelength, 0.154 nm was employed on them and a diffraction pattern was recorded. The observed pattern was compared with JCPDS data using X'Pert high score plus software. Structural analysis was carried out with the use of Rietveld refinement using full-proof software. Rietveld refinement is the mathematical technique used to study and analyze X-ray diffraction data. Using the pre-defined structural model, refinement of the structural parameters such as lattice parameters, atomic positions, and others has been performed. Hence, the refinement was done till the error between the recorded diffraction data was comparable with the theoretical data minimized.

Furthermore, crystallite size has been calculated for dominant peaks using Scherrer's formula:

$$\mathrm{d} = \frac{\mathrm{k}\lambda}{\beta \cos\theta} \tag{2.2}$$

where d is crystallite size (nm), k is shape constant (~0.94), λ is the wavelength of the X-ray (~0.154nm), and β is FWHM corresponding to the grazing angle θ.

2.2.2.2 Scanning Electron Microscopy (SEM)

The study of specimens including its structural, morphological, shape and size of the particles and their distribution were observed as highly magnified images using electron microscopy. When an electron beam is incident on the specimen under study as shown in Fig. 2.6. They are scattered or interacts with the atoms present in the material to produce X-rays, secondary electrons, backscattered electrons, etc. These waves are used to further study the surface morphology using different types of electron microscopy such as SEM, EDX, and TEM.

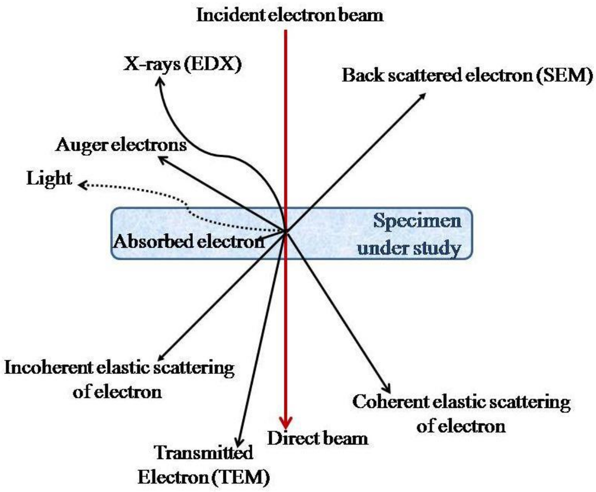

Figure 2.6 Representation of signals occurs after interaction of specimen when incident with an electron beam and used to study the morphological properties of the specimen.

SEM images were recorded using FEI make Nova Nano Scanning Electron Microscope 450. It uses a high-energy electron beam in a raster scan to produce magnified images of the surface of the samples. Using SEM, particles up to the nano range could be viewed easily. When an electron beam is focussed on the surface of the sample which is placed in a high vacuum, the secondary electrons are emitted due to the inelastic interaction. These secondary electrons are collected and reveal the information about the morphology of samples’s surface. The accelerated voltage for the electron gun was kept 30 KV with the resolution of 1.4 nm whereas magnification varies from 35 X to 1,000,000 X. Samples were mounted on the sample holder with gold coating on its surface. The micrographs were taken from low to high magnifications. The average particle size was calculated using the Image J software.

2.2.2.3 Transmission Electron Microscopy (TEM)

Transmission Electron Microscopy (TEM) is a technique to study the size, shape, and morphology of the samples with better magnification. It uses a high voltage and high energy electron beam which falls on the sample surface and transmitted electrons are collected and analyzed to produce images. It consists of an emission source that emits electrons by thermionic/field emission into the vacuum. This source is made up of either tungsten filament or Lanthanum hexaboride (LaB_6). These incident electrons are accelerated with the potential of 100-1000 KV and irradiated on the sample due to which electrons interact and create an image on the screen. Due to the smaller magnitude wavelength of the electrons TEM resolution is of high resolution compared to other microscopy techniques. The powdered sample is dispersed in an aqueous medium and deposited on the Cu grids. This high-resolution TEM technique enables us to analyze the material at the atomic or nano level. In this research work, FEI make Tecnai G220 s-Twin was used to study the morphology, crystallite size, arrangement of atoms through diffraction fringes of the samples, etc.

2.2.2.4 Energy-dispersive X-ray Spectroscopy (EDX)

Energy-Dispersive X-ray Spectroscopy (EDX) is the quantitative technique to determine the various elements present in the prepared samples. It is generally combined with SEM or TEM microscopes. When an electron beam of high energy is incident on the sample, then the atoms acquire high energy. The electrons present in the inner shell of the atoms get excited and ejected from the shell. Hence, it produces an electron-hole which is filled by the electron present in the outer shell thereby emitting X-rays. These emitted X-rays are the characteristics of the atomic structure of the element and are used to identify the element. The energy of emitted X-rays was measured through the detector and hence plotted as the EDX spectrum. In this study, EDX results are combined with the SEM microscopy used.

2.2.3 Vibrational Characterizations

2.2.3.1 Fourier Transform Infrared Spectroscopy (FTIR)

Infrared spectroscopy (IR) is based on the principle that when the sample is irradiated with IR radiation, it absorbs some radiation and some radiations are passed through sample. The passed radiations are recorded through detectors. As the molecules have different structure that produces different spectra leading to distinguish molecules. FTIR is the preferred spectroscopy analysis as it uses the mathematical function that converts the raw data into the IR spectrum. FTIR is used in various fields such as petrochemical, food analysis, organic and polymer science. It is a type of absorption spectroscopy in which bonding between atoms is found via the absorbance of light measured at different wavelengths. In this method, when infrared radiation (IR) is incident to the sample, molecules absorb IR radiation at particular wavelengths which modifies the vibrational energy into the bonds. The energy absorbed is specific for a particular group (or functional group or bond) and useful for qualitative and quantitative analysis. In this study, a PERKIN ELMER make spectrometer was used to record the

Fourier Transform Infrared (FTIR) spectra on a pallet made with a KBr binder in the range of 400-4000 cm^{-1}.

2.2.3.2 Raman Spectroscopy

Raman analysis is a chemical analysis method in which vibrational energy modes of any sample is measured using the scattered light. It describes structural and molecular interaction information on the samples. It is developed on the principle of interaction of light with chemical bonds. When a high-intensity laser light source is incident on the specimen the molecules present in the sample scatter the incident light. The scattered light which have same wavelength as the incident laser source is called Rayleigh scatter. Whlile the small amount of light (approximately 1 in 10 million photons) that is scattered at varied wavelengths is resultant from the chemical bonds present in the sample and known as Raman scatter. The recorded Raman spectra consists of molecular bond vibrations such as C=C, C-C, N-O, etc. with particular intensity and wavelength. Raman spectra is a well defined and unique chemical fingerprint for any specific material that can be used to identify it instantly. Therefore, Raman spectroscopy provides information of the materials consisting of:

1. Chemical structure and phase of the material,
2. Intrinsic stress/strain,
3. Presence of contamination or impurity present,
4. Phase and polymorphism.

In this study, the Raman spectrum is carried out using the Micro-Raman spectrometer Renishaw inVia model with wavelength, 514 nm.

2.2.4 Surface Characterizations

2.2.4.1 Brunauer-Emmett-Teller (BET)

Brunauer-Emmett-Teller (BET) is a scientific technique used to determine the surface area, porosity, and distribution of pore size of solid and porous materials. This technique is based on adsorption of inert gas (such as nitrogen) on the samples's solid surface. The specific surface area in m^2/g is determined by the physisorption of inert gas on the sample surface. It is carried out at a stable temperature based on the inert gas used (such as 77 K for LN_2). The gas molecules are attracted towards the surface of the sample and form a single layer of adsorbed gas. When the gaseous single layer of molecules are formed at the surface of the sample, it is then put into a non-nitrogen atmosphere and further heated. The nitrogen gas molecules which are adsorbed at the surface of the BET sample are released and further quantified. Hence, the surface area and porosity of the sample are calculated. In this research work, BET analysis was performed as surface adsorption of N_2 at 77 K using the Quantachrome NovaWin Surface Analyzer.

2.2.4.2 X-ray Photoelectron Spectroscopy (XPS)

X-ray Photoelectron Spectroscopy (XPS) is a surface quantitative spectroscopic technique used to determine the chemistry and atomic composition of the samples. It is used to determine the electronic states of the elements present in the sample. It is based on the principle of the photoelectric effect in which electron population spectra are obtained when irradiated with X-rays. When a sample is irradiated with monochromatic K_α radiation of X-rays, it is absorbed, resulting in photoelectron emission from the sample. These emitted photoelectrons are further collected and measured to characterize the elements. If the energy of the X-ray photon (E_{photon}) is higher than the binding energy of the electron ($E_{binding}$) then the remaining energy will be utilized as the kinetic energy of the ejected electron $E_{kinetic}$ and given in equation (2.3);

$$E_{kinetic} + \phi = E_{photon} - E_{binding} \tag{2.3}$$

where ϕ is the work function. Its binding energy can be calculated by measuring the kinetic energy of the electron and it is the characteristics of the electronic configuration present in the atom. An XPS spectra is created by plotting the number of electrons *vs.* their binding energy. Here each atom has a unique XPS spectra. Therefore, XPS can be used to measure following properties;

1. The elemental composition of the surface,
2. The experiential formula of pure materials,
3. The electronic or chemical state of each element present on the surface,
4. The homogeneity of elemental composition using mapping,
5. The depth profiling

In this study, a wide range XPS spectra has been observed in the energy range of 0-1200eV using monochromatic Al K_α X-ray source by Thermoscientific NEXA Surface Analyser. The produced X-rays fall on the powdered sample placed on the sample stage. XPS analysis is performed under an ultrahigh vacuum to avoid the loss of electron energy by interacting with residual gaseous molecules.

2.2.5 Electrical Characterizations

In this section, D.C. and A.C. conductivity has been discussed. Furthermore, the preparation of materials for the testing is also mentioned below.

For A.C. and D.C. measurements, all the samples were mixed separately with the polyvinyl alcohol (PVA, 2.5wt%) and pressed into circular discs of 10 mm with the help of a hydraulic press by applying a pressure of 7 Tons. To remove the PVA, pellets were heated at 250 °C for 2-3 h in air. Further, electrical contacts were made using the silver (Ag) coating on the surface of the pellets. Ag paste was applied on both sides of pellets were dried at 150 °C for 1 h in the air to remove any moisture content.

2.2.5.1 D.C. Conductivity Measurements

It is an electrical technique used to calculate the bulk D.C. resistances of the samples. The D.C. conductivity (σ_{DC}), and D.C. Resistance (R_{DC}) were measured using the Kiethley 6430 sub-Femtoamp source meter at room temperature. Temperature-dependent studies were also carried out using the same setup to observe the activation energy (E_a) for all the prepared samples. All sample voltage and current values were recorded from -10 to 10 V at room temperature and I-V curves were plotted to calculate the D.C. resistances. The recorded I-V curves follow the Ohm's law as given in equation (2.4) below:

$$V = I * R \tag{2.4}$$

where V is the applied voltage, I is the flow of current through the sample and R is the resistance. The slope calculated from the current-voltage curves gives the value of the D.C. resistances and D.C. conductivity (σ_{DC}) which is calculated using the equation (2.5) described as:

$$\sigma_{DC} = \frac{L}{R\,A} \tag{2.5}$$

where L is the pellet thickness, R is the D.C. resistance, and A is the area of the pellet in cm, ohms, and cm^2 respectively.

To calculate the activation energy, the Arrhenius equation (2.6) was used and is given below:

$$\sigma = \sigma_0 \exp(\frac{-E_a}{K_B T}) \tag{2.6}$$

Where E_a is the activation energy, σ is electronic conductivity, T is temperature, and K_B is the Boltzmann constant in eV, S/cm, K, and JK^{-1} respectively.

2.2.5.2 A.C. Conductivity Measurements

In an A.C. analysis, R is replaced by the impedance Z which is the combination of the overall resistances and reactance given by the relation:

$$Z = Re(Z) + Im(Z) \tag{2.7}$$

where Re(Z) and Im(Z) is the real part and imaginary part of the Z, respectively, which are plotted in the complex plane known as Nyquist plot. From this analysis, we can find out about the conduction mechanism through grain resistances (R_g) and grain-boundary resistances (R_{gb}). The Cole-Cole or complex impedance plots of the sample pallets were used to study the conduction mechanism. A.C. conductivity for all the samples was calculated by the equation (2.5) and named as σ_{AC}.

In this work, A.C. conductivity is sobserved using complex impedance spectroscopy by a HIOKI make LCR meter (model: IM3536) in which measurement of cell impedance/admittance is recorded over a frequency range of 4 Hz-8 MHz and temperature 28-250 °C.

2.2.6 Electrochemical Characterizations

In this section, the preparation of electrodes, coin cell fabrication, and their characterizations have been thoroughly described.

2.2.6.1 Electrodes fabrication

All the electrodes were fabricated using the same technique. Working material, carbon black, and polyvinylidene fluoride (PVDF) were mixed in the ratio of 70:20:10 or 80:10:10. The uniform mixture of the slurry was prepared using N-Methyl-2-Pyrolodone (NMP) as solvent. The slurry was prepared after the mixing for 5-6 h. The prepared slurry was uniformly coated at the copper (Cu) current collector using Gelon Group make Automatic Coating Unit (Model No.: GN-VC-10H). All the electrodes were dried at 120 ºC overnight in a vacuum oven. The dried electrodes were cut with the electrode cutter of diameter 16 mm and pressed using a Gelon Group make Rolling Pressing Machine (Model No.: GN-RPM-100) for a uniform surface. The weight and thickness of electrodes were measured and again dried at 60 ºC to remove any moisture content before transferring it to the MBraun make glove box work station model LAB star under Ar atmosphere with O_2 and H_2O levels less than 0.5 ppm.

2.2.6.2 Coin Cell Fabrication

Coin cell CR2016 half-cell assembly for electrochemical measurements of all the materials are used in this research work. After the transfer of electrodes, coin cells were assembled as shown in Fig. 2.7. All the dried and weighed 16 mm electrodes were used as working electrode. Polypropylene sheet Celgard 2400 was used as separator and Lithium metal was used as the counter/reference electrode. 1 M $LiPF_6$ in EC: DMC with the ratio of 1:1 (by volume) was used to make aqueous electrolyte. After the assembling of all the parts of the coin-cell, it was pressed and crimped using the Gelon Group make manual coin-cell crimping machine (Model No.: GN-CCH 20). The H_2O and O_2 levels of the glove box were kept at less than 0.5 ppm throughout the procedure of making half-cells. After that, all the cells remained at rest till the constant open circuit voltage (OCV) was achieved in them for further testing such as CV, EIS and GCD etc.

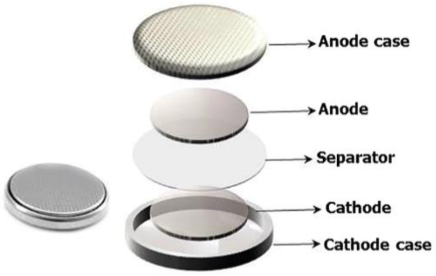

Figure 2.7 Coin-cell assembly used to fabricate Li-ion cell.

2.2.6.3 Electrochemical Impedance Spectroscopy (EIS) Measurements

Electrochemical Impedance Spectroscopy (EIS) is an electrochemical technique that measures the opposition exerted by the electrochemical system when A.C. sinusoidal input is applied. When an A.C. voltage is applied, the resistances are replaced by impedances (Z) consisting of real and imaginary parts of Z. When real (Z) and -Im(Z) are plotted at the x-axis and y-axis respectively, the plot is known as the Nyquist Plot. The Nyquist plot is used to analyze the mechanism involved inside the LIBs which contain semi-circle and straight lines in the high-frequency and low-frequency range respectively. In LIBs, various impedances are responsible in different frequency region due to electrochemical reactions. These impedances are occurred due to the conduction of Li^+ through electrolyte solution and SEI layer, charge transfer between the electrodes, and diffusion of lithium-ions through the electrode materials.

The semi-circle intersect at the x-axis in the high-frequency region corresponds to the resistance between the electrolyte and electrode materials and is named ohmic resistance (R_s). The mid-frequency semicircle occurs due to the electrochemical reactions between the electrode/electrolyte interfaces and is indicated by the charge-transfer resistance (R_{ct}). This value of all the resistances is calculated using the fitting with an equivalent circuit model that consists of the R, C, and L. But in the case of LIBs, CPE (constant phase element) and W (Warburg resistance) are also set to find the diffusion kinetics. CPE shows the non-ideal behavior of the capacitor, which is formed between the electrode and electrolyte. Furthermore, Warburg impedance shows lithium diffusion in the low-frequency region. The basic circuit model known as the Randles model contains series connection of polarization resistor R_1 and bulk resistor R_2 with parallel connection of double layer capacitance (C). In this study, the measurement of EIS has been carried out using BIOLOGIC make model VMP3 multi-channel potentiostat/Galvanostat. An A.C. input signal of magnitude 5 mV in the frequency range of 100 KHz – 10 MHz is used to study EIS for all the freshly prepared cells. The impedance data was further analyzed using EC-Lab software and an EIS analyzer for fitting circuits.

2.2.6.4 Cyclic Voltammetry (CV) Measurements

Cyclic voltammetry (CV) is a fundamental technique to study the reduction and oxidation of electrode molecules. Additionally, it also tells about the number of electrons that shuttle between the anode and cathode during the redox reactions. Furthermore, diffusion coefficient, polarization, reversible or irreversible nature, and diffusive/capacitive/pseudocapacitive behavior of reactants could be studied using this powerful technique. It works on the principle of linear sweep voltammetry in which potential between the working electrode and reference electrode swept linearly in time and corresponding working electrode current is recorded. During the CV testing, the voltage is swept between the range E_1 (lower limit of voltage range) to E_2 (upper limit of voltage range) and reverted from E_2 to E_1 and current is recorded for multiple cycles. Hence, the plotting of the current vs. voltage gives the cyclic voltammogram as shown in Fig.2.8.

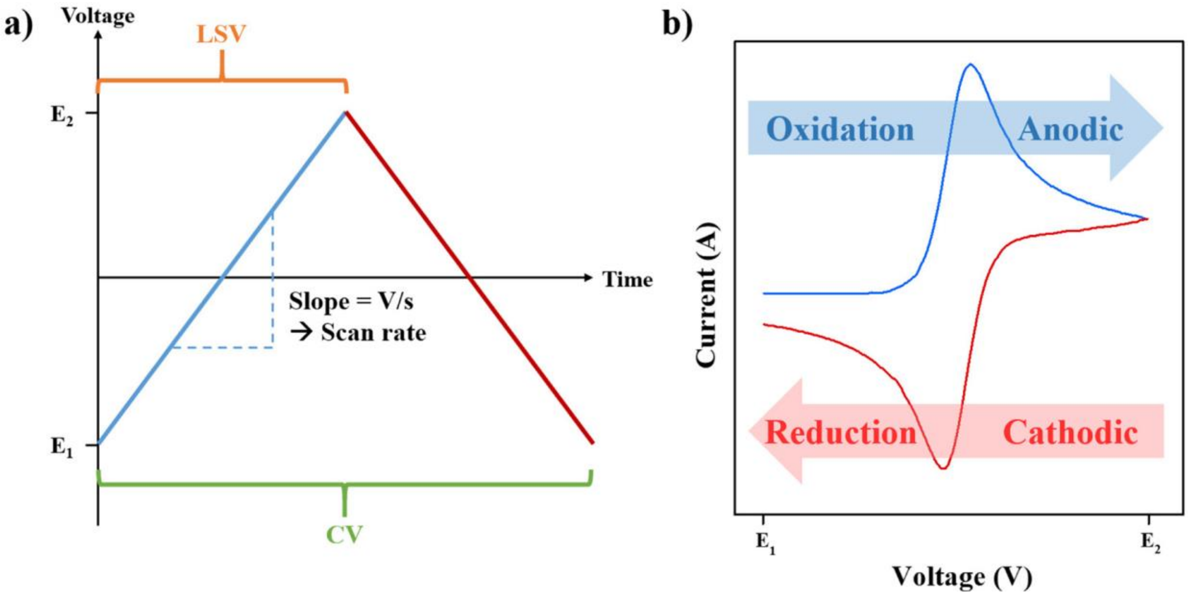

Figure 2.8 (a) Cyclic voltammetry input experimental profile at constant potential and fixed scan rate (mV s^{-1}) **(b)** Cyclic voltammetry output profile.

The cyclic voltammetry is useful:

- To identify whether the particular redox reaction is reversible or not,
- To find out the coulombic efficiency by integrating the total area under the peak,
- To study the change in current response with scan rate and calculate the charge storage mechanism.

Scan rate test: When electrodes are subjected to different scan rates (varied from lower to higher values), higher currents are observed in case of reversible reactions. However, if there is a presence of a quasi-reversible nature, there is a gradual peak shift to a higher potential. By changing the scan rate, the kinetics of the electrochemical redox reaction can be studied. In this work two studies have been focused are given below:

1. The Randles-Sevcik equation (2.8) is used to calculate diffusion coefficient as described below;

   $$\mathrm{I_p} = 2.69 \times 10^5\ \mathrm{n}^{3/2}\ \mathrm{A\ C\ D}^{1/2}\ v^{1/2} \tag{2.8}$$

   Where I_p is peak current, A is the area of the electrode, $v^{1/2}$ is scan rate, C is the analyte bulk concentration, and D is the diffusion coefficient in mA, cm^2, mV s^{-1}, mol cm^{-1}, and cm^2s^{-1} respectively and n is the total number of electrons involved in the redox reaction. For reversible reactions, the plot of peak current (I_p) and scam rate ($v^{1/2}$) must be linear. While for quasi-reversible reactions, the relationship linearity does not hold.

2. The study of faradaic and non-faradaic currents can also be calculated using a scan rate study. Since, the current obeys the power law given in equation (2.9):

   $$i = av^b \tag{2.9}$$

   where i is current in mA, v is scan rate in mV s^{-1}, a and b are constant values. The total b value explains whether the current contribution is diffusion or capacitive controlled. On taking the logarithmic of equation (2.9) on both sides and the plots is shown in Fig. 2.9 (a)

   $$\log i = \log av^b \tag{2.10}$$

$$\log i = \log a + log v^{b} \tag{2.11}$$

$$\log i = \log a + b \log v \tag{2.12}$$

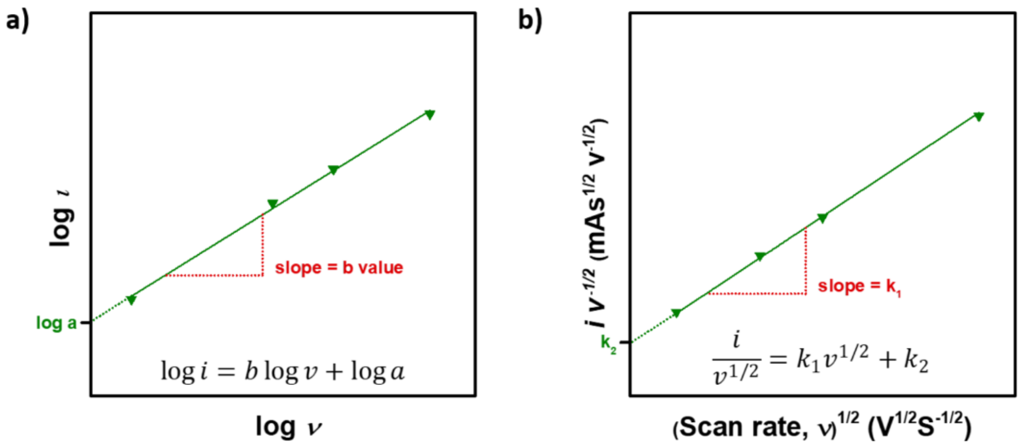

Figure 2.9 (a) Plot between the logarithmic scan rate and current for a particular anodic/cathodic peak to calculate the value of b, **(b)** Plot between the between $v^{1/2}$ and i(V)/$v^{1/2}$ to calculate the current contributions.

The slope calculated using the plot shown in Fig. 2.9 (a) is *b* value which is between 0.5 and 1 depicting diffusion and capacitive controlled respectively. Therefore, at specific potential, the total current can be determined using the equation (2.13):

$$i(V) = K_1 v + K_2 v^{1/2} \tag{2.13}$$

where K_1v and K_2v represent the capacitive current and diffusion-controlled current respectively. The values of K_1 and K_2 can be found using the plot between $v^{1/2}$ and *i*(V)/$v^{1/2}$. The percentage of capacitive and diffusive contributions for a particular scan rate is calculated and studied in this report.

In this research investigation, cyclic voltammetry is performed using BIOLOGIC make multi-channel VMP3 workstation and analyzed using EC-Lab software. All the assembled cells were subject to the cyclic voltammetry test in the voltage window of 0.01-3.0 V with the varied scan rate ranging between 0.1-0.5 mV s^{-1}.

2.2.6.5 Galvanostatic Charge-Discharge (GCD) testing Measurements

In this method, charge-discharge cycles of prepared cells are measured when a constant current is applied and potential is determined as a function of time. The voltage is measured between the two electrodes, working and reference electrode. When constant current is applied via two terminals of the cell. According to the Ohm's law, as the current varies, the input/output profile of the Galvanostatioc Charge-Discharge (GCD) testing will be given as display in Fig. 2.10 (a-b).

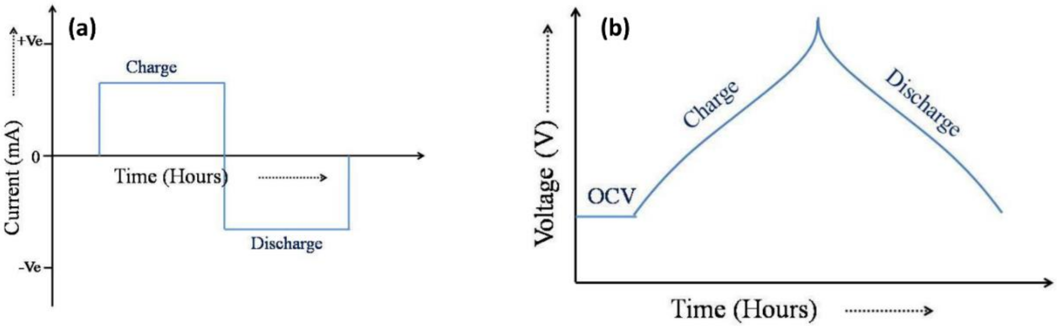

Figure 2.10 (a) Applied input current with time, and **(b)** output charge-discharge profile of galvanostatic charge-discharge measurements.

When the current is applied redox reactions take place at the electrode-electrolyte interface which can be used to study the electrode kinetics. The direction of the current is reversed when it reaches to the potential limit and thus the charge–discharge capacity, cycle life, and rate capability of the material could be observed using this test. All the freshly prepared CR2016 cells were subjected to GCD testing with variable current density/C-rate in the particular potential window. BIOLOGIC make VMP3 multi-channel potentiostat/galvanostat and Neware Battery Testing System (BTS software 8.0) was used to conduct the GCD measurements, cycling performance, and rate capability test.

Chapter 3

Structural, Morphological and Electrochemical studies of $Li_2ZnTi_3O_8$ and $NiMn_2O_4$ using solid-state reaction route

This chapter includes the physicochemical and electrochemical results of the $Li_2ZnTi_3O_8$, and $NiMn_2O_4$ synthesized via a solid-state reaction route. The explanation of each material is given in two separate sections.

3.1 Introduction

Now a days, world's research has been shifting from bulk materials to nanomaterials due to the various advantages of nanomaterials such as excessive surface area, ultimate strength, exceptional conductivity, and many other characteristics [104]. Hence, there is utmost need of nanostructured materials that are applicable in various fields of technologies, however, tremendous advancement has been shown by energy storage devices such as rechargeable batteries.

As commercialized graphite has many disadvantages, therefore, various materials are investigated as anode material for LIBs. Among them, $Li_2MTi_3O_8$; where M may be Zn, Co, Ni, or Mg, etc. has received considerable attention due to its non-polluting nature, safety measures, and low cost as compared to LTO containing less lithium content [48], [97]. Lithium Zinc Titanate ($Li_2ZnTi_3O_8$) cubic spinel material is based on intercalation mechanism and it displays better properties as an alternative prospect of anode material (other than LTO) owing to high theoretical capacity, 227 mAh g^{-1}, lowering in the de-intercalation plateau, 0.5-0.8V *vs.* Li/Li^+, high electronic conductivity, and low cost [56], [63], [66].

Another type of anode material which is based on conversion reactions are metal oxides (AB_2O_4 type) such as $MgFe_2O_4$ [105], $NiCo_2O_4$ [106], $NiFe_2O_4$ [107], $ZnMn_2O_4$ [108], etc. These materials shows the potential to be good ordinate of graphitic anode due to their high capacity (<1000 mAh g^{-1}), thermal stability, cost-effectiveness, synergistically effective mixed cations valance states, and non-toxic nature [105]–[108]. Among these spinel oxides, nickel-manganese oxide ($NiMn_2O_4$) is considered a promising electrode because it can deliver high theoretical capacity (~922 mAh g^{-1}), multiple active sites due to the presence of Mn, and environment benignity [89], [92].

Additionally, the anode materials synthesized at the nano-level offers an approach to enhance the energy/power densities, cyclability, safety, and efficiency of LIBs. Although, the LIBs performance also influenced by contact area between electrodes and electrolyte. As the nanostructured materials possess a large surface-to-volume ratio in comparison to bulk materials, which further enhances the reaction between the electrode-electrolyte interface. The diffusivity of Li^+ with active material increases as the electrode/electrolyte contact area exposes more and thereby escalates the specific capacities at higher current rates [33], [104]. Moreover, the nano-sized materials facilitate shorter path length for Li-ions which improve the rate capability of batteries during the intercalation/de-intercalation process [33], [104]. Furthermore, the nanomaterials can sustain volume expansion and maintain stable cycle performance at variable current rates. [33].

Hence, in this section of this chapter, the structural, morphological, electrical, and electrochemical results have been explained. Solid-state reaction route has been used to synthesize nano-structure of lithium zinc Titanate, $Li_2ZnTi_3O_8$ (LZTO), and $NiMn_2O_4$ (NMO) as mentioned in chapter 2; section 2.1.1.1 and section 2.1.1.2, respectively. For the synthesis of NMO, citric acid was used as a chelating agent because it produces a complex compound with metal ions and stabilize the NMO structure. Hence, NMO material is prepared with two different calcination temperatures, while LZTO is prepared by double calcination process to investigate Physico-chemical, electrical, and electrochemical characterizations as mentioned in chapter 2; section 2.2.

3.2 Part A : Structural, Morphological, and Electrochemical Studies of Complex Spinel Titanate $Li_2ZnTi_3O_8$

3.2.1 Results and Discussions

3.2.1.1 Thermogravimetric and Differential Thermal Analysis (TGA and DTA)

Figure 3.1 shows the results of TGA and DTA of the as-prepared ball milled sample with the precursors: Li_2CO_3, $Zn(CH_3COO)_2.2H_2O$, TiO_2) to analyze the formation mechanism of the $Li_2ZnTi_3O_8$ (LZTO) material. From the TGA curve, it can be observe that there is a slight mass loss (~7.23%) up to 175 °C, it is accompanied by an endothermic peak around 335 °C which is related to the desorption or removal of moisture present in the sample. The gradual decrement in the weight loss in percentage could be seen till 700 °C with the increment in temperature that is accompanied with broad exothermic peaks. These peaks are due to the carbon dioxide (CO_2) loss from Li_2CO_3 as related by the chemical reaction involved in this whole process as given in equation (3.1) [109];

$$\mathrm{Li_2CO_3 + ZnO + 3TiO_2 \rightarrow Li_2ZnTi_3O_8 + \ CO_2 \uparrow} \tag{3.1}$$

Beyond 700 °C, there is no weight loss which confirms that no further reaction occurs after 700 °C and LZTO phase formation has started.

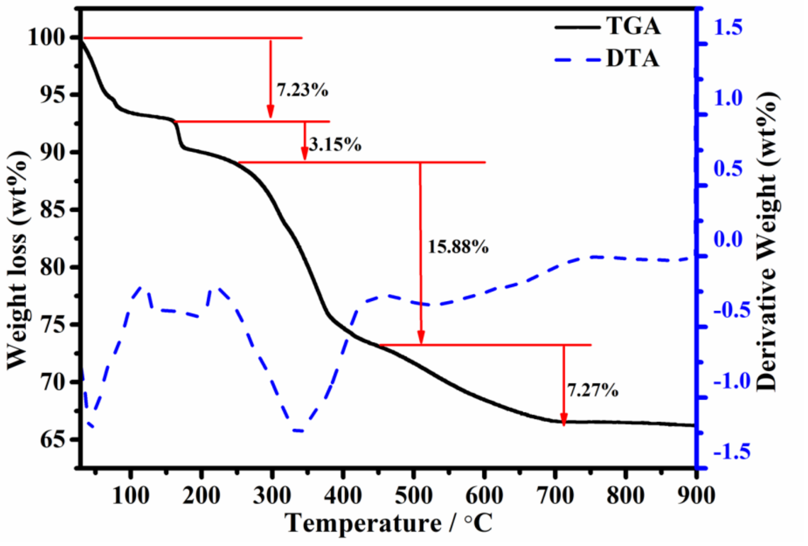

Figure 3.1 TGA and DTA curve of as-prepared ball-milled LZTO sample recorded from room temperature to 900 °C at a rise rate of 10 °C min^{-1} in the air atmosphere.

3.2.1.2 X-ray Diffraction Analysis (XRD)

XRD pattern of calcined $Li_2ZnTi_3O_8$ (LZTO) nano-material synthesized using solid-state reaction route is displayed in Fig. 3.2(a). All the sharp and intense peaks of the LZTO material are in correspondence to the cubic spinel structure matching with JCPDS #086-1512 file and shows $P4_332$ space group. Hence, the crystalline nature of calcined LZTO material could be confirm from the sharp diffraction peaks with no presence of any impurities. The crystallite size of the LZTO is calculated using Scherrer's equation (2.2) as described in chapter 2; section 2.2.2.1 and it is observes as 36.78 nm. Rietveld refinement of LZTO XRD pattern has been also performed for structural analysis using the $P4_332$ space group structure model via full-proof software as display in Fig. 3.2(b).

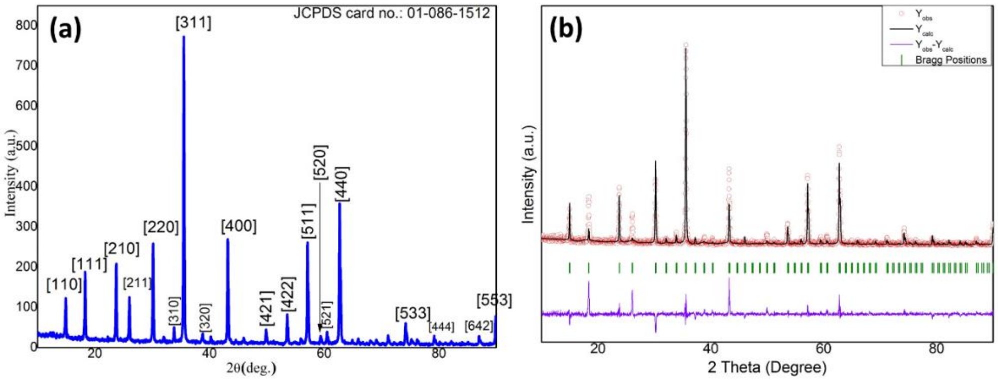

Figure 3.2 (a) XRD pattern of calcined $Li_2ZnTi_3O_8$ (LZTO) recorded in 2θ range of 10º to 90º at room temperature, and (b) Rietveld analysis of observed LZTO XRD pattern performed using full-proof software.

Table 3.1 summarizes the corresponding atomic positions, lattice parameters, and accuracy of the simulations performed. The goodness of fit is estimated as 1.80 which indicates the refinement results are acceptable. The lattice constant ‘a’ of the synthesized LZTO is found to be 8.3693 Å with corresponding volume, 586.24 Å^3 after Rietveld refinement which is consistent with actual parameters.

Table 3.1 Structural parameters result for synthesized $Li_2ZnTi_3O_8$ sample with corresponding goodness of fit (ζ = 1.8).

Wyckoff position	Atom	x	y	z	Occupancy
8c	Li	0.01131	0.01131	0.01131	0.5
4b	Li	0.62500	0.62500	0.62500	1
12d	Ti	0.38043	0.86957	0.12500	1
8c	Zn	0.01131	0.01131	0.01131	0.5
24e	O	0.93750	0.11142	0.35362	1
8c	O	0.39379	0.39379	0.39379	0.39379

3.2.1.3 Scanning Electron Microscopy (SEM) and Energy Dispersive X-ray Analysis (EDX)

Figure 3.3 (a-c) shows the observed SEM micrographs for LZTO material calcined at 800 ºC temperature at different magnifications. Hence, SEM micrographs depicts the irregular shape of particles in the sub-micron range. Also, a slight presence of agglomeration can be seen in the calcined LZTO material. The average particle sizes are calculated using ImageJ software and observed in the order of 100-200 nm. Figure 3.3 (d) shows the elemental composition analysed using EDX analysis.

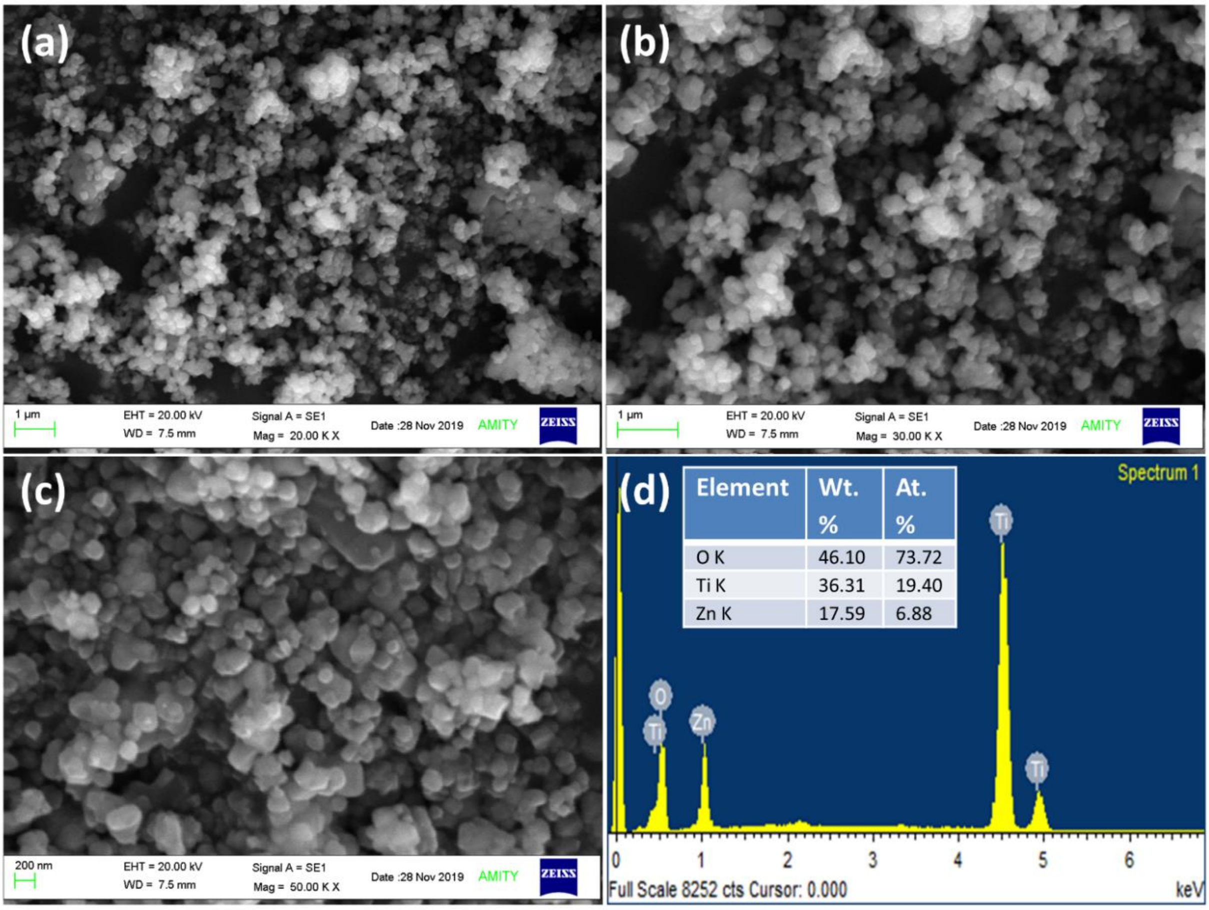

Element	Wt. %	At. %
O K	46.10	73.72
Ti K	36.31	19.40
Zn K	17.59	6.88

Figure 3.3 (a-c) SEM micrographs observed at different magnifications, and **(d)** EDX spectrum for calcined LZTO.

The observed atomic% and weight % ratio of elements: Zn, Ti, and O are displayed in the inset table in Fig. 3.3 (d), which indicate the presence of Zn, Ti, and O in the synthesized LZTO material.

3.2.1.4 Electrical Measurements

D.C. resistance (R_{DC}) is calculated from the I-V curve of synthesized LZTO material as shown in Fig. 3.4 (a) which is in the order of ~10^7 Ohms. The range of voltage signal for the data collection is kept from -10 V to 10 V. Figure 3.4 (b) illustrates an Arrhenius plot, which is potted between ln σ_{DC} and the reciprocal of absolute temperature to calculate the activation energy (E_a) from the slope. The electronic conductivity and activation energy is calculated using the equation (2.5) and equation (2.6) respectively as described in chapter 2; section 2.2.5.1. The calculated electronic conductivity and activation energy of the sample are found to be in the order of 10^{-8} S cm^{-1} and 10^{-4} eV, respectively.

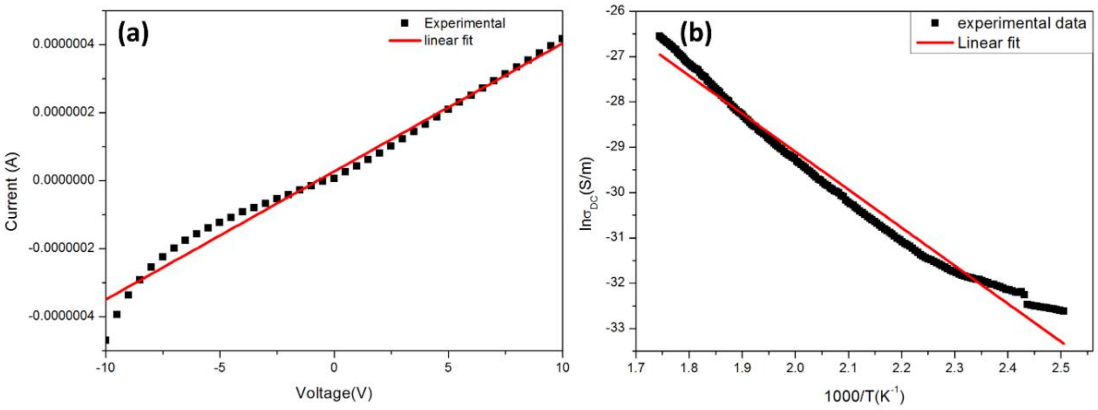

Figure 3.4 (a) I-V curve of LZTO material recorded from -10 to 10 V, (b) Arrhenius Plot between 1000/T and ln σ_{DC}.

3.2.1.5 Electrochemical Measurements

Cyclic voltammetry (CV) measurements provide information regarding redox reactions within the cell. Figure 3.5 (a) depicts the CV curves of pristine LZTO material recorded in the potential window of 0.05 - 3.0 V for a scanning rate of 0.5 mV s^{-1}. A cathodic and anodic pair of peaks in the voltage between 1.0 - 2.0 V is observed and it is associated with the reaction of the Ti^{3+}/Ti^{4+} redox couple [61]. For the subsequent cycles, there is a shifting in the cathodic peak towards the higher potential which indicates the phase transition from spinel to rock salt structure [75]. Furthermore, a cathodic peak below 0.5±0.05 V is also observed, related to multiple restorations of Ti^{4+} [75]. Figure 3.4 (b) displays the charge-discharge curves of synthesized electrodes for 20 cycles at a current rate of 0.1 C in the potential window of 0.05 to 3.0 V. The voltage plateaus for the charge-discharge curve follow the potential peaks of voltammogram curves (Fig. 3.5 (a)). Galvanostatic charge and discharge (GCD) capacities are observed to be 240.2±10 mAh g^{-1} and 267.43±10 mAh g^{-1}, respectively, as recorded at 0.1 C for the first cycle.

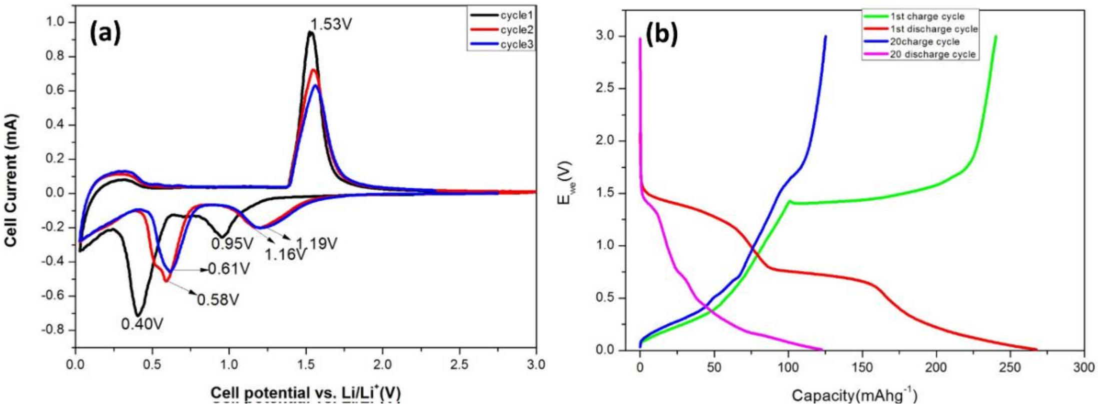

Figure 3.5 Electrochemical performances of $Li_2ZnTi_3O_8$ material. (a) CV curves of LZTO recorded at a 0.05 mVs^{-1} scan rate, (b) GCD performance recorded within the potential window of 0.05-3.0 V.

EIS measurements show the mechanism of the charge transfer and Li^+ diffusion behavior. Figure 3.6 (a) shows the Nyquist plot of synthesized LZTO material of freshly prepared cells in the frequency ranging between 100 kHz to 10 mHz. Here, a semi-circle in the high-frequency region is associated with the charge transfer resistance between electrode-electrolyte interfaces. While, the low-frequency region, consisting of a straight line, is related to the diffusion of Li^+ within active material [73]. The enlarged image of spectra with a fitted equivalent circuit diagram is shown in Fig. 3.6 (a), which includes Re as charge-transfer resistance, Rs as electrolyte resistance, W as Warburg resistance, and CPE as constant phase element. After linear fitting, Re and Rs are 3.013 ohms and 72.82 ohms respectively, which depicts the good electronic conductivity of LZTO material [61], [62], [73], [75].

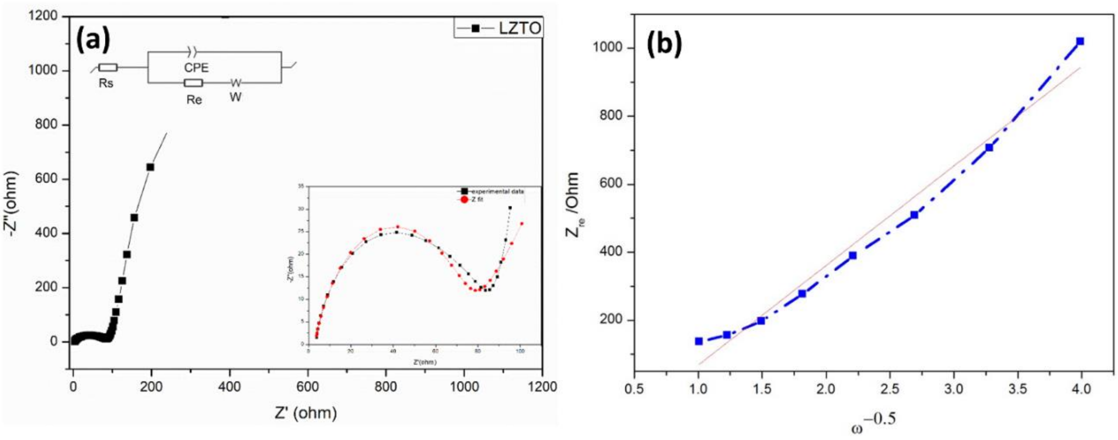

Figure 3.6 EIS results of LZTO **(a)** Nyquist curve recorded at 5 mV AC amplitude, **(b)** Plot between frequency and real of Z (Z') in the low-frequency region.

To calculate the diffusion coefficient (D_{Li+}), the following equation (3.2) was used:

$$D_{Li^+} = \frac{R^2T^2}{2A^2n^4F^4C^2\sigma^2} \tag{3.2}$$

where D_{Li+}, T, R, A, n, F, and C are the diffusion coefficient of Li^+ ions (cm^2/s), absolute temperature (K), gas constant (8.3145 J $mol^{-1}K^{-1}$), surface area of the electrode used (2.0096 cm^2), number of electrons involved in a redox reaction, Faraday constant, and concentration of lithium ions respectively.

Warburg factor (σ) which is related using the following equation (3.3):

$$Z_{re} = R_e + R_{ct} + \sigma\omega^{-0.5} \tag{3.3}$$

Figure 3.6 (b) shows the plot between Z_{re} and $\omega^{-0.5}$. From the above equations (3.2) and (3.3), the diffusion coefficient (D_{Li+}) was found to be approx. 10^{-17} cm^2 s^{-1}.

Hence, in this section, physico-chemical, electrical and electrochemical properties of spinel type $Li_2ZnTi_3O_8$ (LZTO) material have been studied. XRD and rietveld results confirm the formation of pure and crystalline phases of LZTO. SEM analysis shows that the LZTO particles are uneven in shape with an average particle size of 100-200nm. Conductivity measurements shows that the LZTO has higher conductivity (~10^{-8} S/cm) in comparison to other Titanate materials. Electrochemical studies show that LZTO has a reasonable discharge plateau (~0.5 V) as well as high capacity and demonstrate that it has potential to use as alternative anode material for LIBs.

3.3 Part B: Synthesis, characterization, and electrochemical investigation of citric-acid-assisted nickel manganese oxide ($NiMn_2O_4$) as anode material.

3.3.1 Results and Discussions

3.3.1.1 Thermogravimetric and Differential Thermal Analysis (TGA and DTA)

For $NiMn_2O_4$ (NMO) samples prepared by ball-milling synthesis route, TGA and DTA has been carried out in the temperature range of room temperature (RT) to 800 ºC at a scan rate of 10 ºC/min. in air atmosphere as shown in Fig. 3.7. From Fig. 3.7, it can be observe that at 100 °C – 150 °C temperature interval, there is an initial small mass loss of 5.2% which is accompanied with an endothermic peak of 103 ºC corresponding to the evaporation of absorbed H_2O content by the precursors. Following, a gradual mass loss of 24.1% accompanied by an intense exothermic peak at 309 ºC mainly corresponds to the oxidation of residual carbon as the temperature rises to 350 ºC in the sample of NMO. After that, there is a sharp mass loss till 700 ºC, which can be associated with the decomposition of metal acetic salts. Beyond 700 ºC, a stable platform appears which indicates there is no further reduction in mass, indicating the optimum temperature for the formation of the NMO phase.

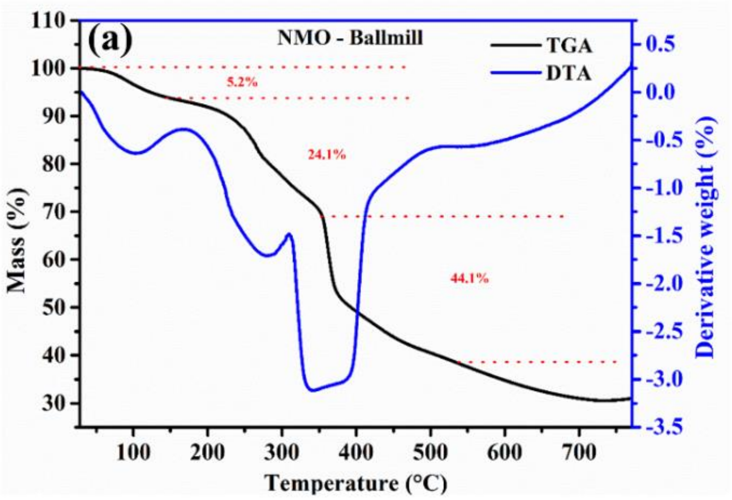

Figure 3.7 TGA and DTA plot of as-prepared NMO ball-milled sample heated from room temperature to 800 °C at a rise rate of 10 °C min^{-1} in the air atmosphere.

3.3.1.2 X-ray Diffraction Analysis (XRD)

Figure 3.8 (a) displays the XRD patterns to confirm the crystallinity and structure of the NMO samples calcined at 700 °C (NMO_700) and 800 °C (NMO_800). All the diffracted peaks are well indexed to cubic symmetry with JCPDS file no.: 071-0852 and *Fd3m* space group. The reflections (311), (440), (511), (220), (400), (222), (422), and (111) corresponding to NMO are present in both samples. Sharp and narrow peaks confirm zero impurity, as well as, indicate the crystalline nature of both samples. Additionally, NMO_800 exhibits more intense and sharper peaks as compared to NMO_700 depicting that calcination temperature improves the crystallinity of the material which consequently may improve the structural stability of NMO during electrochemical reactions.

Figure 3.8 (b-c) shows the Rietveld refinement plots obtained after using the cubic spinel structure in the *Fd3m* space group model. FullProf program suite was used to perform the rietveld refinement. Initial structural parameters were taken from the

JCPDS card (#071-0852) for the NiMn$_2$O$_4$ phase for the refinement. The value of goodness of fitting (ζ) is estimated as approaching unity which indicates that the refinement results are reliable. All the structural parameters after refinement are tabulated in Table 3.2.

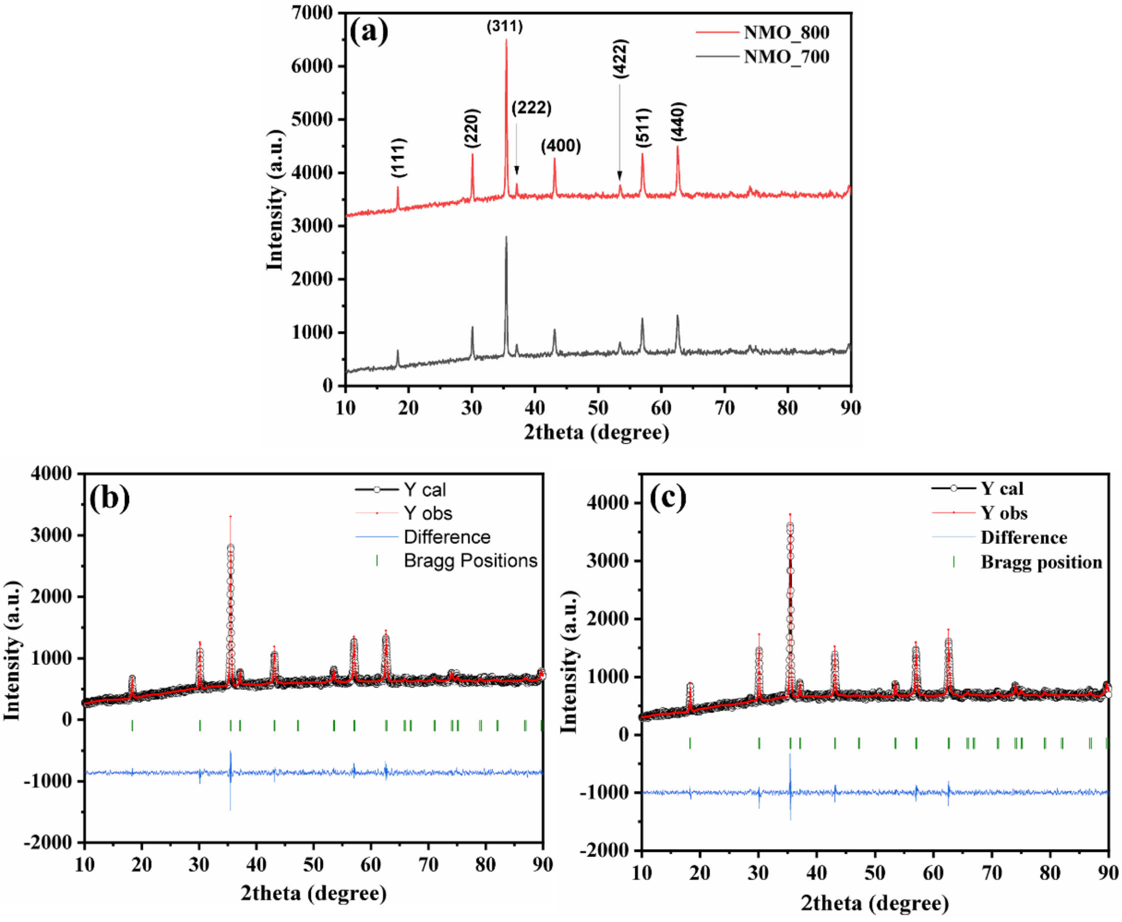

Figure 3.8 (a) XRD patterns recorded from 10-90º 2θ at room temperature, and (**b-c)** Rietveld Analysis of observed XRD pattern of NiMn$_2$O$_4$ calcined at two different temperatures 700 and 800 °C.

Furthermore, Scherrer’s equation (2.2) as mentioned in chapter 2; section 2.2.2.1 is used to calculate the crystallite size corresponding to the dominant peak (311) and is tabulated in Table 3.2. It can be observe that as the calcination temperature increases crystallite size increases which is consistent.

Table 3.2 Structural Parameters of NMO samples refined using Rietveld analysis.

Sample	**Crystallite size (nm)**	**a=b=c (Å)**	**V ($Å^3$)**	χ^2	**R_{wp}**	**R_{exp}**	**R_f**	**R_b**
NMO_700	36.31	8.389	590.487	1.38	21.3	18.1	6.15	6.20
NMO_800	60.51	8.393	591.277	1.43	19.8	16.5	4.92	4.59

3.3.1.3 Scanning Electron Microscopy Analysis (SEM)

Citric Acid and calcination temperature have a major role in the formation as well as the morphology of synthesized products. Figure 3.7 (a-b) and (c-d) illustrate the observed SEM micrographs of NMO_700 and NMO_800 at different magnifications respectively. It can be observed from Fig. 3.9 (b) that NMO_700 has an unsystematic shape of nanoparticles which could be due to the lower calcination temperature. Additionally, nanoparticles form globular clusters of microdimensions. Whereas, NMO_800 (Fig. 3.9 (d)) micrographs displayed relatively smooth boundaries and nearly spherical-shaped particles with less agglomeration. Additionally, the mean particle size effectively reduces to <1μm which could be helpful for the Li^+ mechanism inside the electrodes. However, Fig. 3.9(b) shows that NMO_700 nanoparticles are connected, which could be further advantageous for the flow of e^-/Li^+ during redox reactions.

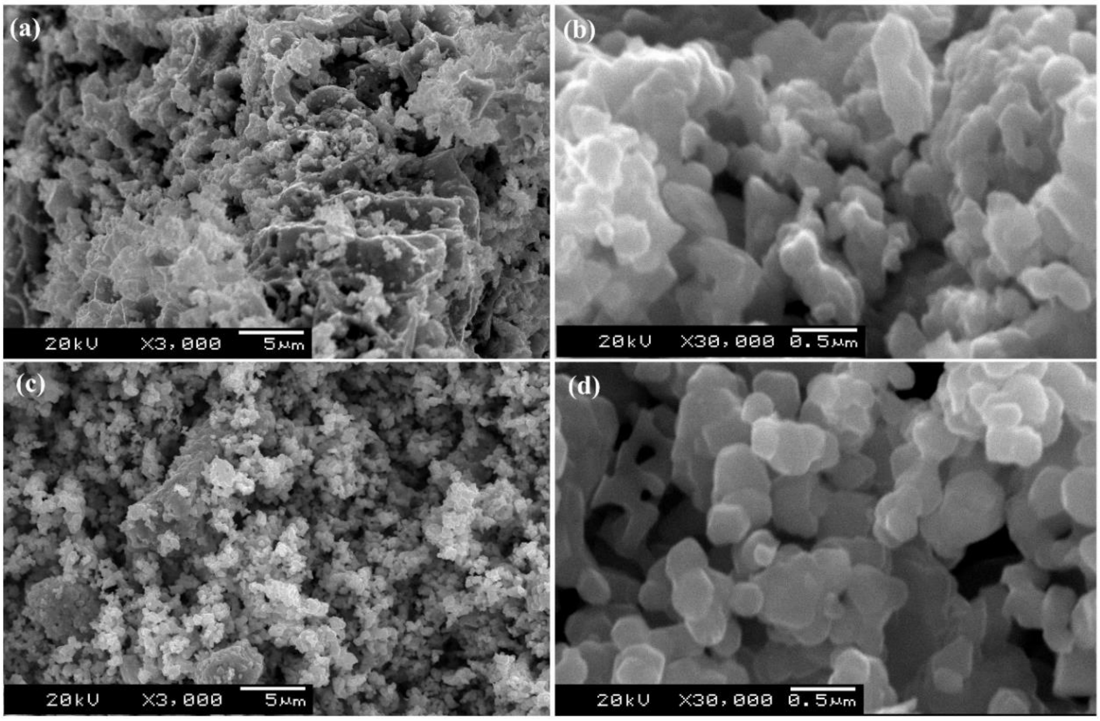

Figure 3.9 SEM micrographs of calcined **(a-b)** NMO_700, and **(c-d)** NMO_800 samples at varied magnifications.

3.3.1.4 Temperature–dependent electrical measurements

Figure 3.10 (a) displays the I-V curve for both NMO samples recorded at room temperature. The value of the calculated D.C. resistance (R_{DC}) using the slope of the I-V curve is tabulated in Table 3.3. Furthermore, corresponding D.C. conductivity (σ_{DC}) is calculated using the equation (2.5) as mentioned in chapter 2; section 2.2.5.1. The calculated value of conductivity using equation (2.5) is tabulated in Table 3.3 which depicts that as the calcination temperature rises, the conductivity of NMO samples is enhanced which could be helpful in the flow of e^-/Li^+ inside the electrode. Furthermore, the temperature-dependent resistivity (ρ_{DC}) is measured for both the NMO samples from room temperature to 480 ºK. Figure 3.10 (b) shows the plot of ρ_{DC} against temperature. In addition, as the calcination temperature of NMO samples increases from 700 ºC to 800 ºC, the value of resistivity decreases. However, for both samples, the value ρ_{DC} decreases to a particular temperature and then remains constant with temperature increments. This behavior of NMO samples is described as a Negative Temperature Coefficient (NTC) and also depicts the conduction mechanism of charge carriers between Mn^{3+} and Mn^{4+} ions at octahedral sites[85], [110]. Table 3.3 displays the initial values of ρ_{DC}, which is due to the presence of impurities, and voids [110]. The difference in initial resistivity could be confirmed from SEM images which show that irregular grain boundaries of NMO_700 give the medium for electrons to move freely and attain high resistivity compared to NMO_800 which had an even particle shape and defined grain boundaries. Furthermore, the linear decrease in resistivity for both samples could be due to the thermally activated hopping mechanism [85], [110]. In general, cations Mn^{3+} occupy tetrahedral sites (A sites) while if Ni^{2+} <1.0, it occupies A sites, and Mn^{3+}/Ni^{2+} occupy octahedral sites (B sites) but as the temperature rises, B sites are occupied by Ni^{2+} and Mn^{3+} dissociate into Mn^{2+} and Mn^{4+}. The converted Mn^{2+} ions drift to the A site and Mn^{3+}/Mn^{4+} occupies octahedral sites which improve electrical conductivity and simultaneously improve electrochemical properties [85], [110]. Moreover, the Activation energy (E_a) is calculated using the Arrhenius equation (2.6) as described in chapter 2 section; 2.2.5.1. The Arrhenius plot between ln conductivity and temperature in kelvin is shown in Fig. 3.10 (c) from which the calculated activation energy (E_a) are 0.370 eV and 0.378 eV for NMO_700 and

NMO_800 samples respectively.

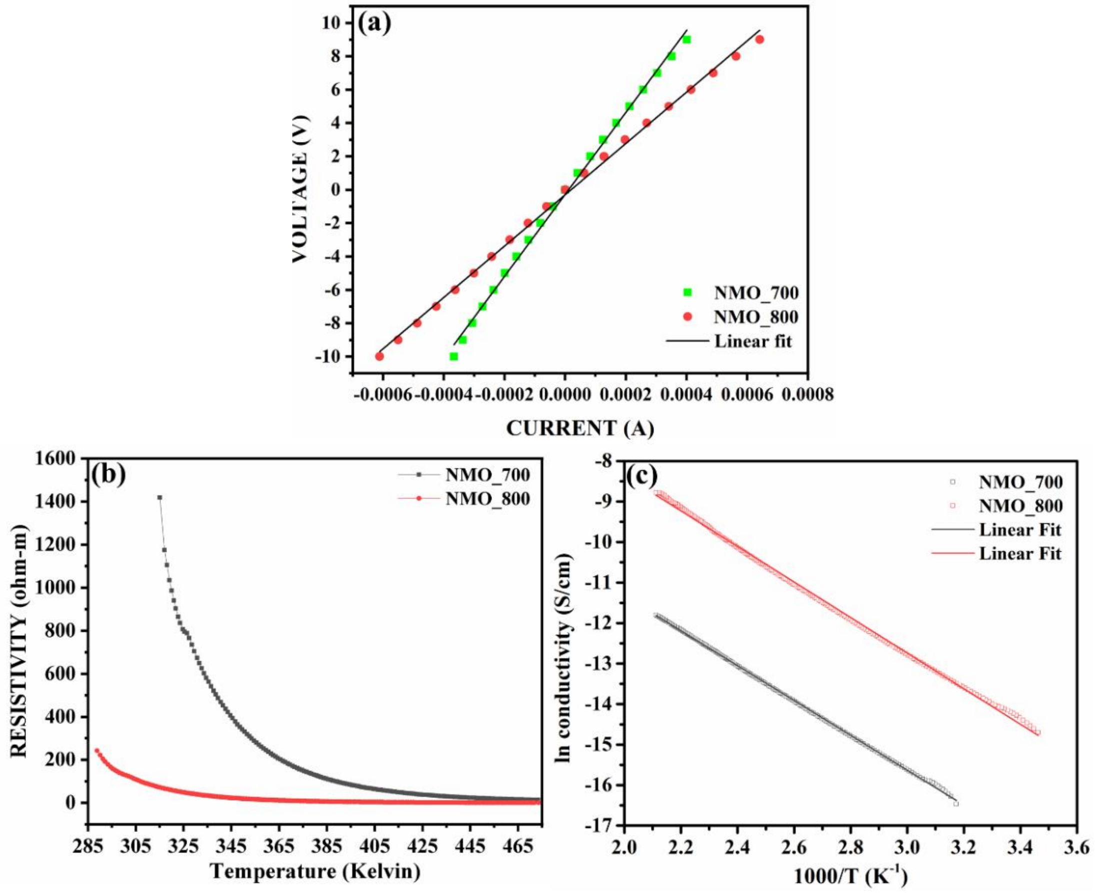

Figure 3.10 Electrical measurements of synthesized $NiMn_2O_4$ samples: **(a)** Current-Voltage (I-V) curve at room temperature, **(b)** Plot of resistivity with temperature varies from 285 K to 485 K, and **(c)** Arrhenius Plot of calcined $NiMn_2O_4$ samples.

Table 3.3 Electrical Parameters of calcined $NiMn_2O_4$ samples.

Sample	**R_{DC} (KΩ)**	**σ_{DC} (S/mm)**	**ρ_{DC} (Ω-m)**	**ρ_{DC} (405 K) (Ω-m)**	**E_a (eV)**
NMO_700	24.5	7.74 X 10^{-7}	1418.61 (315ºK)	62.76	0.370
NMO_800	15.38	1.38 X 10^{-6}	242.22 (288.8ºK)	7.44	0.378

3.3.1.5 Electrochemical Measurements

From the electrical studies, it is confirmed that, calcination as well as high working temperatures of $NiMn_2O_4$ greatly affect the electrical performance which could be beneficial to test this material as an anode. Therefore, to study the electrode material and lithium ions kinetics as well as the redox reactions performance, measurements such as CV and EIS are performed and studied on half-cell assembly.

3.3.1.5.1 Cyclic Voltammetry (CV) Analysis

The electrochemical properties of both samples are characterized using Cyclic Voltammograms recorded at a scanning rate of 0.1 mV s^{-1} from 0.01-3.0 V volatage range. Figure 3.11 (a) shows the CV curves for the 1st and 2nd cycles of both NMO samples. In the initial anodic scan, a broad peak around 0.8-1.3 V is observed in the case of NMO_800 while two broad oxidation peaks around ~1.0 V and ~2.0 V in NMO_700 which could be related to the oxidation of Mn and Ni to Mn^{3+} and Ni^{2+} respectively [88], [90]. In both cases, during the first discharge scan, a peak around ~0.5 V is associated with the formation of the Li_2O matrix as well as the reduction of $NiMn_2O_4$ to metallic Ni and Mn [90]. Additionally, the second peak around ~0.3 V is attributed to the irreversible decomposition of electrolytes to form SEI layer [92]. From CV curves, it can be seen that with the increment in cycle, there is a shift in cathodic peaks towards lower voltage values which could be ascribed to the different electrochemical reactions. The energy density of the lithium-ion battery could be affected by the de-lithiation potential. The lower the negative electrode potential the higher the output voltage. Hence, CV curves confirm that $NiMn_2O_4$ can attain capable results as an anode for LIBs. Furthermore, from cycle 1 the sharp and high magnitude of current in NMO_800 depicts better structural stability as well as electrochemical performance as compared to NMO_700. The active electrodes undergo the following electrochemical reactions which can be summarized in equations (3.4 - 3.7);

$$NiMn_2O_4 + 8Li^+ + 8e^- \rightarrow Ni + 2Mn + 4Li_2O \quad (3.4)$$

$$Ni + Li_2O \leftrightarrow NiO + 2Li^+ + 2e^- \quad (3.5)$$

$$Mn + Li_2O \leftrightarrow MnO + 2Li^+ + 2e^- \quad (3.6)$$

$$2MnO + \frac{1}{3} Li_2O \rightarrow \frac{1}{3} Mn_3O_4 + \frac{2}{3} Li^+ + \frac{2}{3} e^- \quad (3.7)$$

Columbic Efficiency (C.E.) from 2nd cycle is calculated using CV curves by taking the numerical integration of discharge-charge current and described in equation (3.8);

$$CE = \frac{\int I_{discharge}\, dt}{\int I_{charge}\, dt} \quad (3.8)$$

Table 3.4 shows the calculated C.E. values. Interestingly, both the samples show almost similar C.E. i.e., 92.14% and 92.06% for NMO_700 and NMO_800 samples respectively. Therefore, it can be concluded that the efficiency of both samples is nearly the same irrespective of the morphology of the samples. Additionally, this high value of C.E. shows that the $NiMn_2O_4$ electrodes possess a reversible nature when used as anode for LIBs.

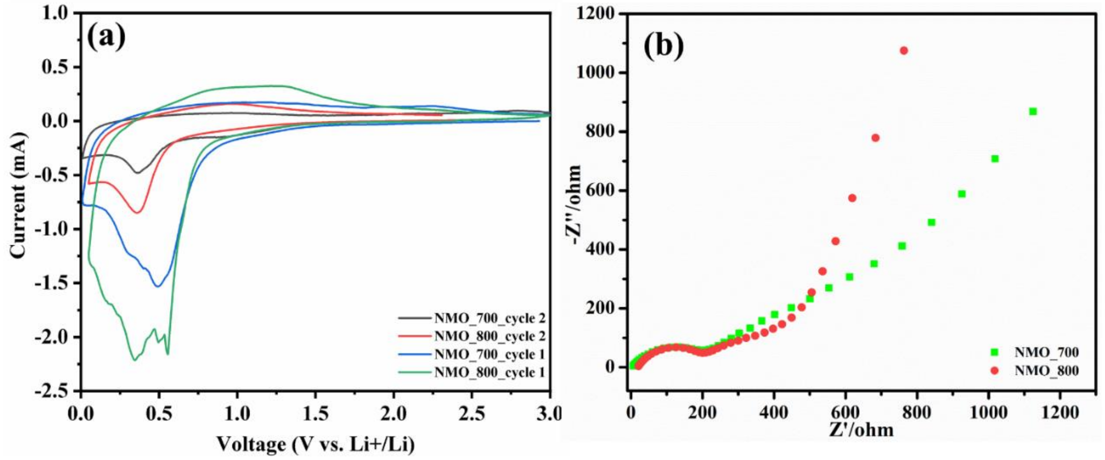

Figure 3.11 (a) CV curves recorded at a voltage range from 0.05-3.0 V with a scan rate of 0.1 mV s^{-1} **(b)** EIS/Nyquist curves recorded at an AC amplitude of 5 mV.

3.3.1.5.2 Electrochemical Impedance Spectroscopy (EIS) Analysis

The interfacial reactions which are occurring at the electrode surface are studied using EIS measurements. Figure 3.12 (b) displays the EIS/Nyquist spectra of freshly prepared cells recorded in the scanning frequency range of 10 mHz-100 kHz with an input 5 mV AC voltage. From the plots, it can be noted there is a semi-circle in the high-frequency region and a following straight line in the low-frequency region. The Z' axis-intercept in the high-frequency region gives the ohmic resistance (R_s) between the electrode and electrolyte. Electrochemical reactions occur at the electrode and electrolyte material is denoted by charge-transfer resistance (R_c). The fitted values of R_s and R_c for both the NMO samples are tabulated in Table 3.4. It can be observed that NMO_800 has low charge-transfer resistance between the electrode material and electrolyte which suggests higher electrochemical activity in comparison to NMO_700. However, NMO_700 has a lower value of ohmic resistance which suggests the thin SEI layer formation and diffusion of Li^+/e^- is high in comparison to NMO_800. Therefore, it can be concluded that the calcination temperature affects the electrochemical properties of $NiMn_2O_4$ material and it must be optimized for higher efficiency.

Table 3.4 Calculated CV and EIS parameters are for $NiMn_2O_4$ samples.

Sample	**Columbic Efficiency (from CV curves)**	**R_c (Ω)**	**R_s (Ω)**
NMO_700	92.14%	226.44	3.52
NMO_800	92.06%	204.09	18.64

Therefore, in this section ball-mill route synthesized spinel type $NiMn_2O_4$ (NMO) material shows promising results as anode materials for LIBs. XRD results confirms the formation of pure and crystalline phases of NMO. Rietveld results shows that calcination temperature have no effect on the structural properties of NMO material. SEM studies displays NMO_700 and NMO_800 nanoparticles are uneven in shape. Conductivity measurements of NMO material shows conductive nature with presence of the negative temperature coefficient (NTC) behaviour. Electrochemical studies such as CV and EIS demonstrate that NMO material have potential to use as alternative anode materials for LIBs.

Chapter 4

Investigation of the electrical and cycling performance of $NiMn_2O_4$ anode material synthesized via different routes

In this study, simple and effective solid-state and sol-gel routes are attempted to synthesize Nickel Manganese Oxide, $NiMn_2O_4$ (NMO). Structural, morphological, electrical, and electrochemical properties are investigated with calcination temperatures. All the samples prepared by both of these synthesis routes exhibit above 98% columbic efficiency after two initial cycles and show the reversible nature of $NiMn_2O_4$ and excellent cyclability. The electrochemical results confirm that preparation methods and calcination temperature have a great impact on the electrochemical performance as anode

4.1 Introduction

Mixed transition metal oxides such as $ZnMn_2O_4$ [111], $NiCo_2O_4$ [112], $ZnFe_2O_4$ [113], and many more have also been studied as anode material for LIBs. Among them, Ni-Mn-based mixed metal oxides have been explored as the anode electrode for LIBs applications [88], [90], [114], [115]. However, like other metal oxides, Ni-Mn-based oxides still show poor conductivity, low structural stability, and large capacity loss. Since, preparation techniques have a constructive effect on the electrode's properties, structure, and morphologies which play an important role in the electrical properties of spinel-type metal oxides thereby affecting the electrochemical performance of LIBs. Hence, in this investigation $NiMn_2O_4$ based anode material is synthesized using different synthesis techniques at different temperatures.

One synthesis method used is solid-state route, in which repeated grinding and high-temperature calcination were performed. Another method used is Sol-gel synthesis in which the mixing of precursors is carried out in atomic level. However, the formation of a proper phase depend on many parameters such as chelating agent (citric acid, ascorbic acid, adipic acid), acidic nature, and pH value. Here, citric acid has been used for chelation because of its outstanding chelating capability with a wide range of cations.

In this chapter, the presented work is focused on the formation of nickel manganese oxide, $NiMn_2O_4$ (NMO), and $NiMn_2O_4/NiMnO_3$ using different synthesis routes including the inexpensive, and simple sol-gel methods followed by thermal treatment. Here, the results of the same material synthesized by the solid-state chelation method are compared with sol-gel method. However, there are limited reports regarding the solid-state chelation methods for this anode material for LIBs. Therefore, in this study, the citric acid effect on the morphological, electrical, and electrochemical properties of NMO has been studied. Since citric acid produces a complex compound with metal ions and changes the structural as well as morphological properties of as-prepared anode material. In general, NMO compounds have been used as an application of supercapacitors but there are few reports of this compound as an anode without any carbon additive for LIBs. The effect of the synthesis route and calcination temperature on the crystallinity, particle size, morphology, electrical conductivities, and electrochemical properties is investigated in this study. Synthesis details of Nickel Manganese Oxide ($NiMn_2O_4$, NMO) prepared by solid-state reaction route and sol-gel route has been mentioned in Chapter 2 section 2.1.1.2 and 2.1.2.1 respectively. Physico-chemical, electrical, and electrochemical characterizations of NMO material are performed as mentioned in Chapter 2 section 2.2.

4.2 Results and Discussions

4.2.1 Thermogravimetric and Differential Thermal Analysis (TGA and DTA)

Figure 4.1 shows the weight/mass loss with the temperature for Thermogravimetric analysis (TGA) and the derivative of weight vs. temperature for Differential Thermal Analysis (DTA) of the sol-gel prepared sample. It is seen that there is an abrupt mass loss in the temperature range from 150 ºC to 300 ºC, which could be ascribed to the rapid elimination due to the removal of CO_2, water content, and acetic salts. These results suggested that the wet chemical route decreases the temperature for calcination. However, from the solid-state route, it is confirmed that 700 °C is the minimum temperature for the formation of the crystalline $NiMn_2O_4$ phase. To analyze the phase formation using XRD, as-prepared samples were calcined at two different temperatures 700 °C and 800 °C for 3 h in air, and named NMO-700 and NMO-800 respectively to obtain the pure and crystalline samples.

Comparatively, the TGA/DTA plot of solid-state prepared NMO samples has been discussed in Chapter 3 section 3.2.2.1 and samples calcined at 700 ºC and 800 ºC for 3 h in air has been named as NMOB_700 and NMOB_800 respectively.

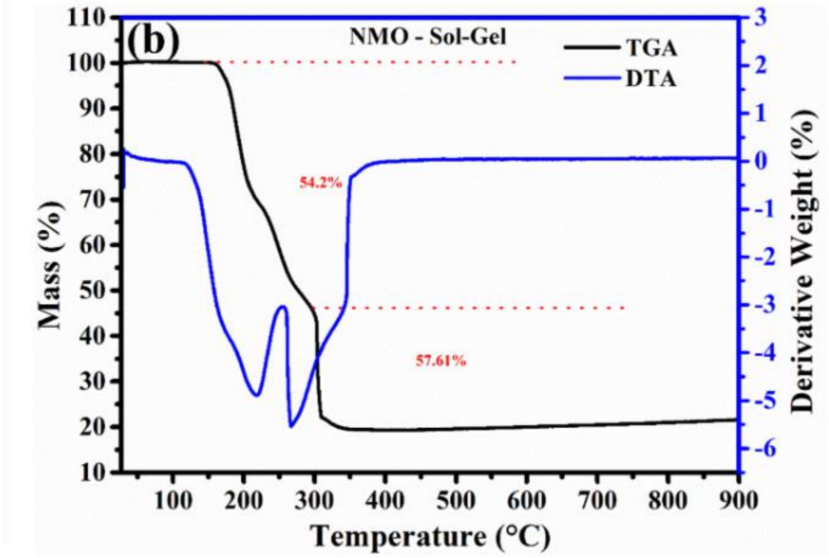

Figure 4.1 TGA and DTA curve of as-synthesized $NiMn_2O_4$ using sol-gel route from room temperature to 800 ºC in air.

4.2.2 X-ray Diffraction Analysis (XRD)

XRD analysis (Fig. 4.2 (a)) confirms the structure and phase composition of all calcined samples: NMOS_700, NMOS_800, NMOB_700, and NMOS_800. All the major diffraction peaks match with the reference pattern, JCPDS file No. 01-071-0852, it confirms the cubic phase with the Fd3m space group. However, material synthesized using the sol-gel method, NMOS_700, shows the weak peaks of the $NiMnO_3$ phase which are indexed to the rhombohedral ilmenite phase (JCPDS No. 00-048-1330). The

$NiMnO_3$ phase for NMOS_800 has been eliminated as the calcination temperature alleviates. It can be observed that all the peaks exhibit a sharp intense nature illustrating proper crystallinity without any presence of impurity peaks. Crystallite size corresponding to the major peak, (311) for all the samples is calculated by applying the Scherrer equation (2.2) as mentioned in chapter 2 section 2.2.2.1. For sol-gel samples, crystallite size advances from 40.31 nm to 60.46 nm with the increased calcination temperature. Similarly, for ball-milled samples, crystallite size increases from 36.31 nm to 60.51 nm. In both the cases, as the temperature of the calcination rises, crystallite size increases. Furthermore, the crystalline phase formation of $NiMn_2O_4$ and $NiMn_2O_4/NiMnO_3$, without any additive would be helpful in the enhanced electrochemical performance of LIBs.

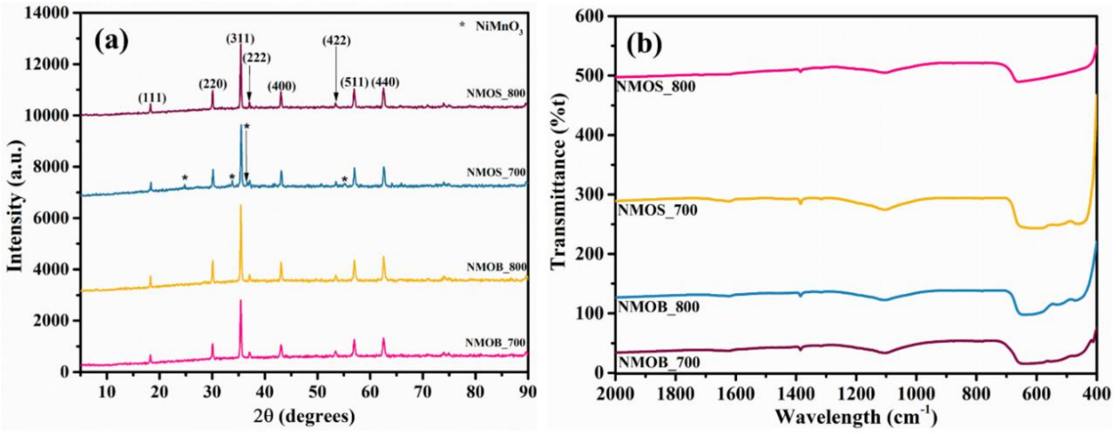

Figure 4.2 (a) XRD pattern recorded in the range of 5-90°, and **(b)** FTIR spectrum recorded from 400 cm^{-1} to 2000 cm^{-1} at room temperature, for NMOB_700, NMOB_800, NMOS_700, and NMOS_800 samples.

4.2.3 Fourier Transform Infrared Spectroscopy (FTIR)

The chelation of nickel and manganese ions with citric acid is studied using the FTIR spectrum as shown in Fig. 4.2(b) measured in a wide range of 400-2000 cm^{-1} for both the samples NMOB_700, NMOB_800, NMOS_700, and NMO_800. The small peak around ~1624 cm^{-1} can be associated with the O-H stretching vibrations of the adsorbed H_2O molecules present on the surface of NMO [84], [116], [117]. The intense FTIR peak at ~1102 cm^{-1}, can be indexed to a couple of C-(OH) and C-O-H bending present in citric acid [118]. This confirms the chelation of Ni^{2+} and Mn^{2+} ions from the complex citrate formation is achieved during the synthesis process [118] . The bands observed below 1000 cm^{-1} are related to $NiMn_2O_4$ and $NiMnO_3$ phases [84]. The broad peaks around 600 cm^{-1} and 400 cm^{-1} are associated with the vibration mode of $Mn^{3+}–O^{2-}$ and $Ni^{2+}– O^{2-}$ groups, corresponding to tetrahedral and octahedral sites of metal oxides confirming the formation of $NiMn_2O_4$ [84], [116]–[118].

4.2.4 Scanning Electron Microscopy (SEM), Transmission Electron Microscopy (TEM) and Energy Dispersive X-ray Spectroscopy (EDX) Analysis

Scanning Electron Microscopy (SEM) micrographs describe the morphology of calcined samples: NMOS_700, NMOS_800, NMOB_700, and NMOS_800 as shown in Fig. 4.3 (a-h). here, Fig. 4.3 (a-d) displays the SEM images of the $NiMn_2O_4$ samples (NMOB_700 and NMOB_800) prepared via a solid-state route depicting the agglomerated particles are irregular and elongated in shape. Consequently, for material synthesized at 700 °C using a sol-gel route, cuboid-type cluster formation of particles is observed as shown in Fig. 4.3 (e-f). The cuboid-type shape could be advantageous for the transport of Li^+ during the electrochemical reactions. However, in the case of sample NMOS_800, as the calcination temperature increases, the formation of the dense blocks-like structure with agglomerated morphology is observed (Fig. 4.3 (g-h)). In both preparation routes, with the increment in the calcination temperature (Fig. 4.3

(c-d) (g-h), fine edges can be observed in microparticles with the absence of cluster formation which could further enhance the Li^+ movement within the electrode.

High Resolution – Transmission Electron Microscopy (HR-TEM) images of NMO samples synthesized using solid-state route (NMOB_700 and NMOB_800) and sol-gel route (NMOS_700 and NMOS_800) are shown in Fig. 4.4 (a-f) and 4.4 (g-l) respectively. It is evident from TEM images that as the calcination temperature increases, the elongated particles are modified into hexagonal-shaped particles irrespective of the synthesis route. Furthermore, for both synthesis routes, measured particle size increases from <100 nm to <0.5 µm, which is also evident from XRD crystallite size results. From Fig. 4.4 (e, h, k), fine-edged particles are seen in all the samples. The TEM images in Fig. 4.4 (c, f, i, l) depict~~s~~ the zoomed images of the corresponding diffraction fringes pattern and clear lattice fringes are visible with a lattice spacing of 0.48 nm, 0.29 nm, 0.2 nm, and 0.48 nm corresponding to (111), (220), (400), and (111) planes, for NMOB_700, NMOB_800, NMOS_700, and NMOS_800 samples, respectively, confirming the majority phase formation of $NiMn_2O_4$ in all the samples.

To study the elemental composition and proper distribution of elements, Energy Dispersive X-ray Spectroscopy (EDX) is also performed for all the $NiMn_2O_4$ samples. Figure 4.5 (a-b) shows EDX mapping of Ni, Mn, and O elements for the sample area, suggesting the proper formation and uniform distribution.

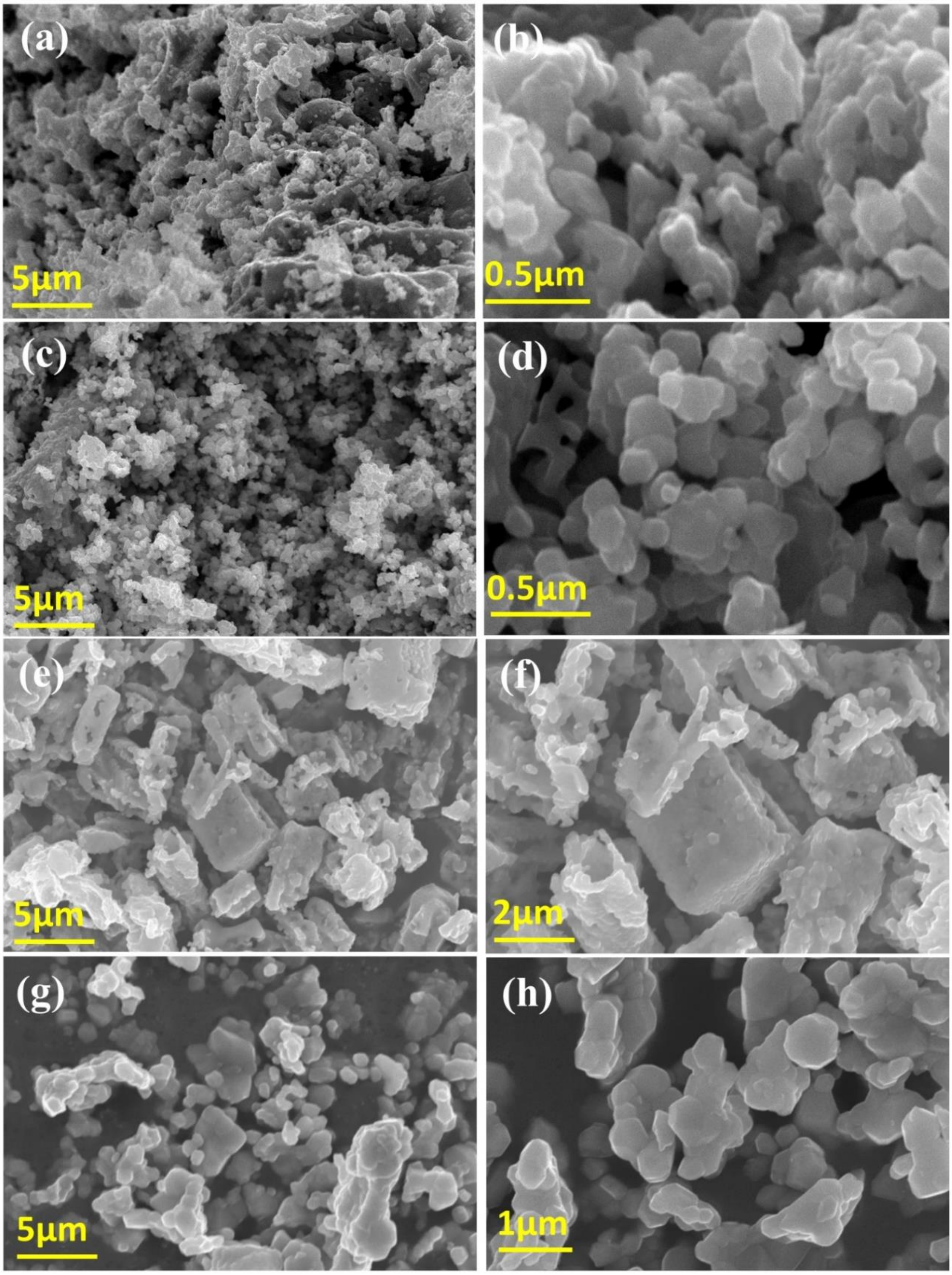

Figure 4.3 SEM micrographs observed at different magnifications for **(a-b)** NMOB_700, **(c-d)** NMOB_800, **(e-f)** NMOS_700, and **(g-h)** NMOS_800 samples.

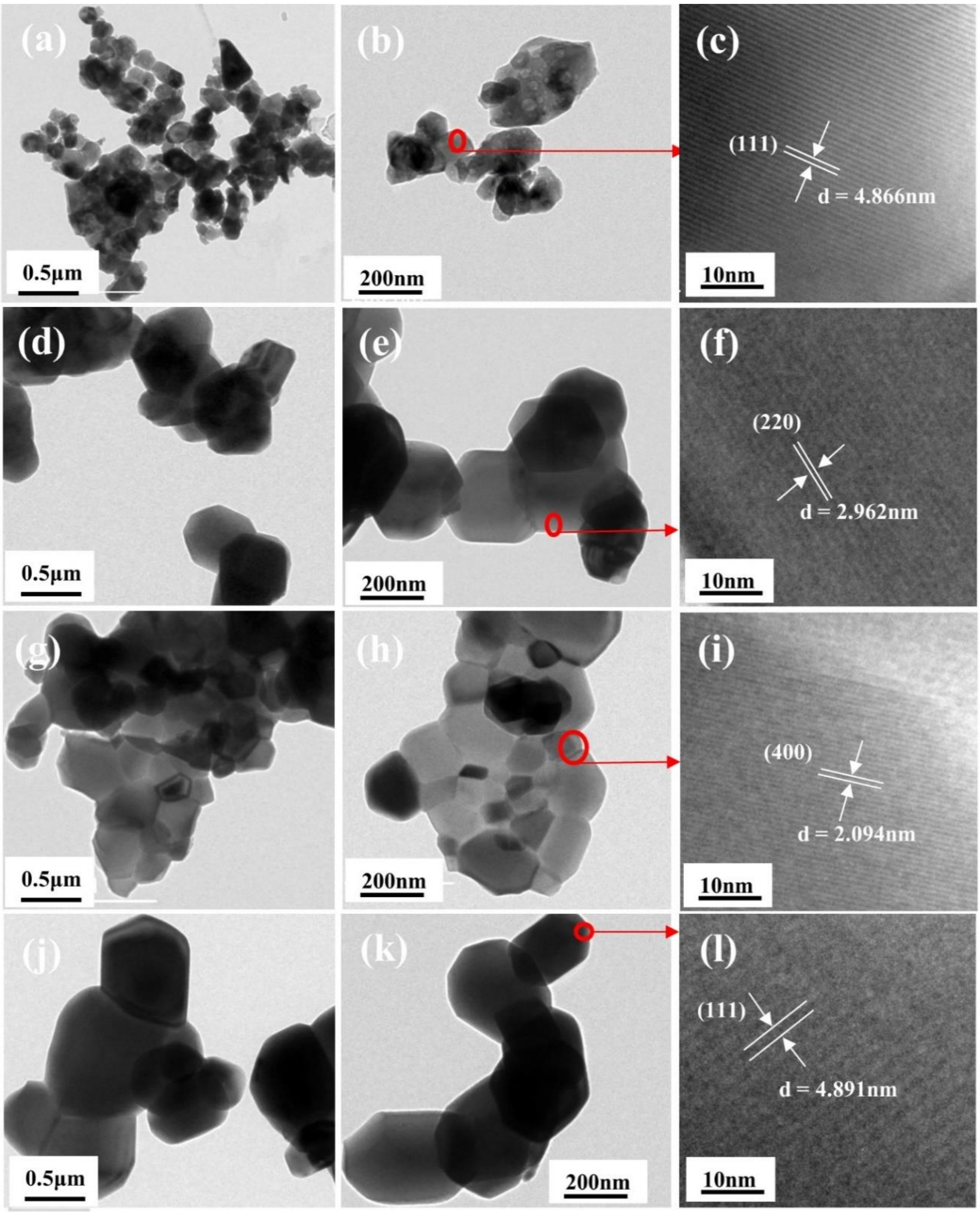

Figure 4.4 TEM micrographs and diffraction fringes observed at different magnifications for **(a-c)** NMOB_700 **(d-f) N**MOB_800 **(g-i)** NMOS_700 **(j-l)** NMOS_800 samples.

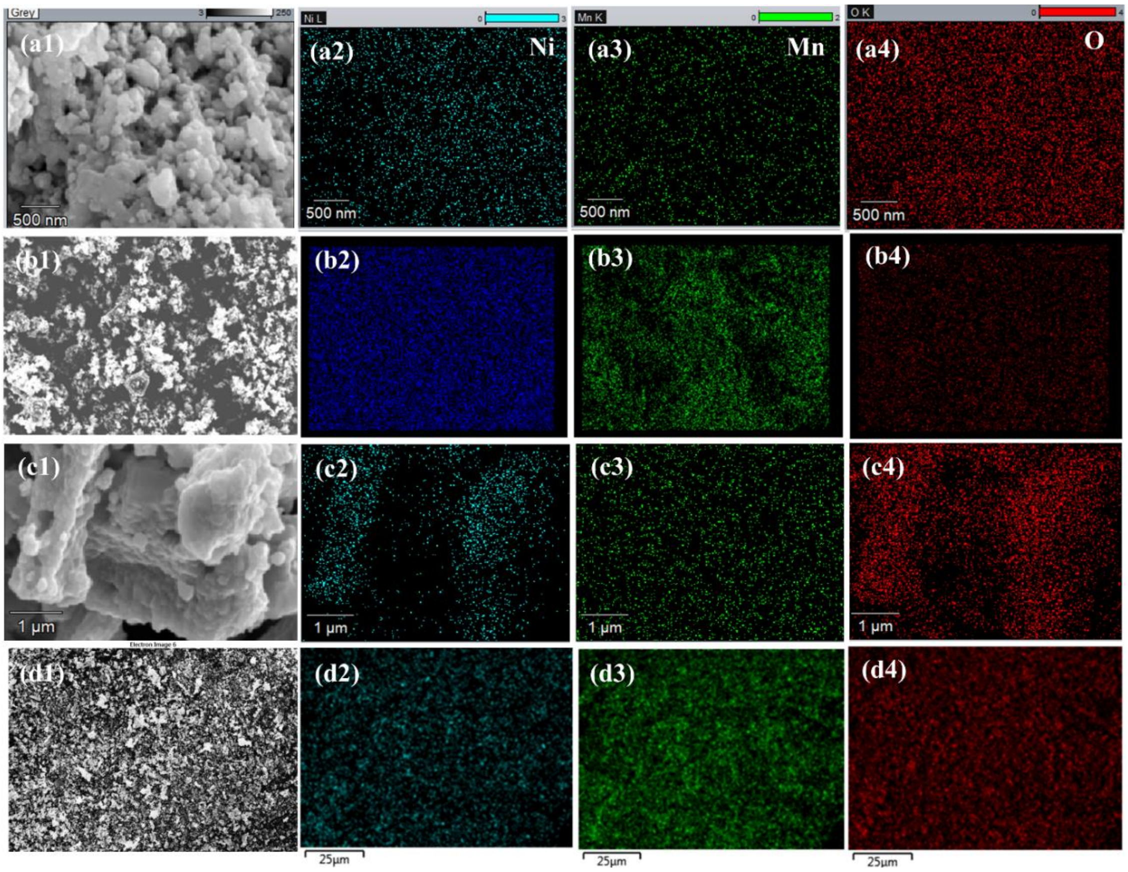

Figure 4.5 EDX mapping recorded for **(a1-a4)** NMOB_700 **(b1-b4)** NMOB_800 **(c1-c4)** NMOS_700 **(d1-d4)** NMOS_800 samples.

4.2.5 Surface Analysis

X-ray Photoelectron Spectroscopy (XPS) is investigated to further study the chemical composition and oxidation states present in all the $NiMn_2O_4$ samples. Figure 4.6 (a-d) shows the high-resolution XPS spectrum for NMOB_700, NMOB_800, NMOS_700, and NMOS_800 samples respectively. The wide scan survey spectra in the range of 0-1200 eV reveal the presence of characteristic peaks of Mn (2p), Ni (2p), O (1s), and C (1s) states as displayed in Fig. 4.6 (a1-d1). All the samples exhibit a similar distribution of energies within this wide range of 0-1200 eV which suggests the formation of pure $NiMn_2O_4$ irrespective of synthesis routes. The C (1s) peak (Fig. 4.6 (a1-d1)) in all the

NMO samples originated due to the formation of MnC_2O_4 in the synthesis process [117]. While, Mn (2p) core level spectrum (Fig. 4.6 (a2-d2)) displays two major peaks at energies ~641.3 eV and ~653.1eV for all the samples which are assigned to Mn $2p_{3/2}$ and Mn $2p_{1/2}$ respectively [90], [117]. After de-convolution and fitting, new peaks are observed at binding energies ~641.3 eV and ~653.1 eV, these are related to Mn^{2+} [88]. Furthermore, peaks centered at ~643.5 eV and ~656.6 eV are related to Mn^{3+} and Mn^{4+} oxidation states, respectively [88], [92]. The spin-orbital splitting of Mn (2p) doublet is about ~11.6 eV which is ascribed to Mn^{3+} and Mn^{4+} state in all the NMO samples [84], [92], [115]. Similarly, Fig. 4.6 (a3-d3) exhibits, the Ni (2p) spectrum of the Ni^{2+} and Ni^{3+} spin orbitals characteristic, while peaks at ~861.1 eV and ~879.6 eV are ascribed to shake-up peaks of Ni $2p_{3/2}$ and Ni $2p_{1/2}$ edges, respectively [88], [90], [117]. The difference of ~6.6 eV between the $2p_{3/2}$ and its shake-up peak in Ni core spectra reveals the electronic hybridization of p and 3d orbital, revealing the existence of Ni atom in the divalent form [89]. To further confirm, the de-convoluted peaks at ~854.7 eV and ~872.3 eV are related to Ni^{2+} while others at ~860.0 eV and ~879.5 eV are assigned to Ni^{3+} states [88], [90], [117]. Figure 4.6 (a4-d4) shows the fitted O (1s) spectra in which peaks at ~529.4 eV and ~530.9 eV corresponded to the metal-oxygen (M-O-M) bonds and lattice oxides (O^{2-}) present in NMO samples [84], [89], [92], [117]. Therefore, according to XPS analysis, the existence of Mn^{3+}/Mn^{2+} and Ni^{3+}/Ni^{2+} confirms the $NiMn_2O_4$ composition. Also the presence of Ni, Mn and O is also consistent with EDX and XRD results. These multiple oxidation states involved in the redox reactions would provide a synergistic effect on the electrical and electrochemical performance.

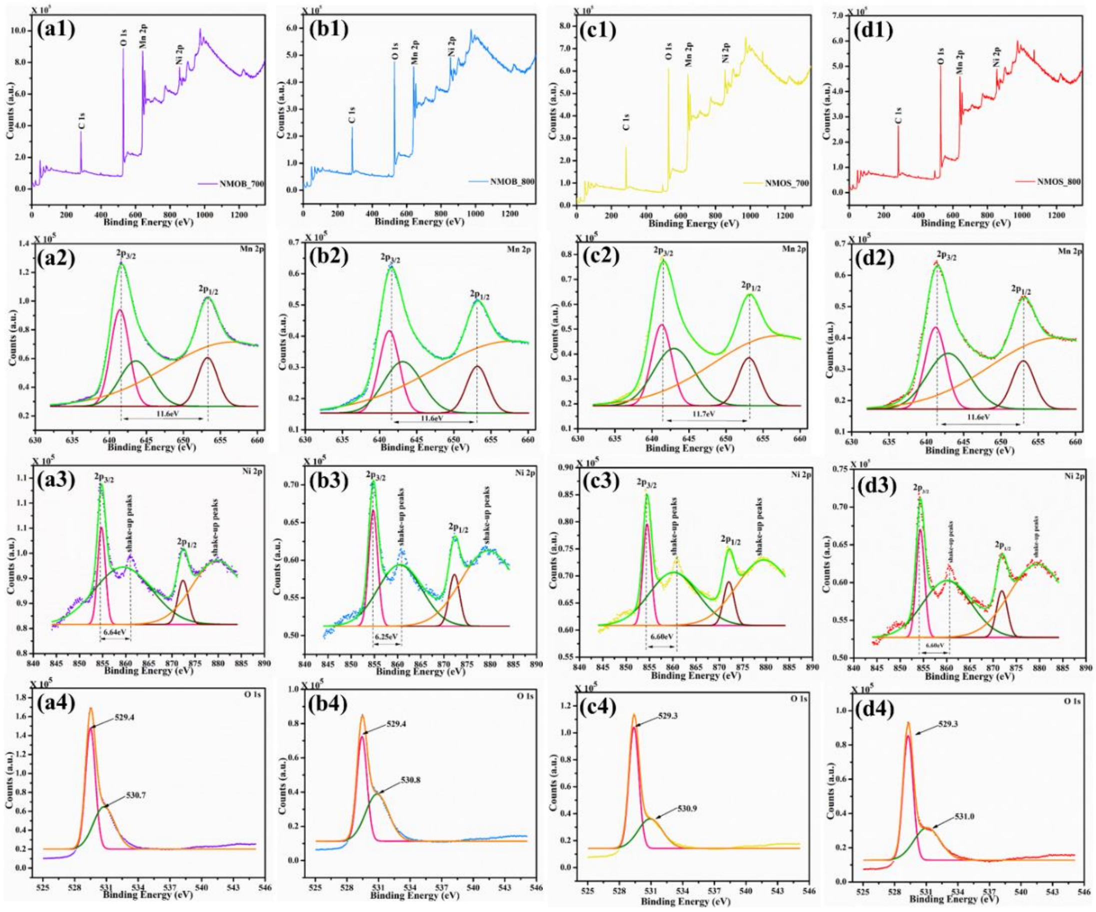

Figure 4.6 XPS survey, Mn (2p), Ni (2p), and O (1s) spectrum recorded for (a1-a4) NMOB_700, (b1-b4) NMOB_800, (c1-c4) NMOS_700, and (d1-d4) NMOS_800 samples.

Brunauer-Emmett-Teller (BET) measurement is also conducted to further analyze the surface area using the N_2 adsorption-desorption isotherms as shown in Fig. 4.7. As the calcination temperature increases from 700 ºC to 800 ºC, the surface area decreases for the samples prepared by both the routes. The surface area varies from 6.1 $m^2 gm^{-1}$ to 4.8 $m^2 gm^{-1}$ and 9.4 $m^2 gm^{-1}$ to 3.8 $m^2 gm^{-1}$ for sol-gel and ball-mill synthesized samples, respectively with the varied calcination temperature. The higher surface area provides more active sites for Li^+ and electrolyte interaction during the charge-discharge process and thus improves electrochemical performance. Furthermore, Table 4.1 also shows the relation between the crystallite size and surface area, depicting the relation with XRD results. For sol-gel samples, the presence of hysteresis loops is due to the collapsing of the structure on increasing temperature, which is visible in the SEM results also. Therefore, the BET surface area results indicate that there is a significant effect of synthesis routes on the surface, thereby improving the cycle/rate performance of $NiMn_2O_4$.

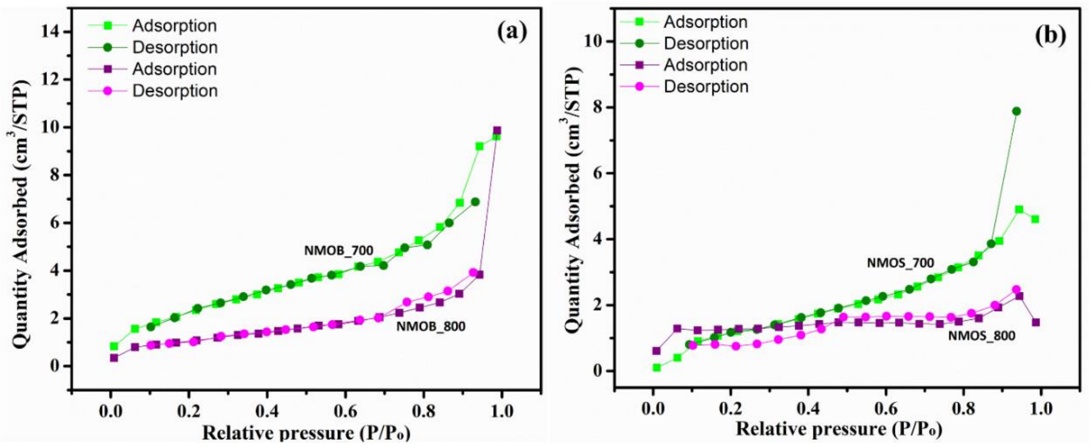

Figure 4.7 N_2 adsorption-desorption isotherms for (a) ball-mill synthesized NMOB_700 and NMOB_800 samples, and (b) sol-gel synthesized NMOS_700 and NMOS_800 samples.

Table 4.1 BET surface area with corresponding XRD crystallite size of ball-milled and sol-gel synthesized samples.

Sample	XRD Crystallite size (nm)	BET surface area (m^2/gm)
NMOS_700	40.31	6.14
NMOS_800	60.46	4.88
NMOB_700	36.31	9.43
NMOB_800	60.51	3.80

4.2.6 Electrical measurements

It is an essential requirement for LIBs to work in harsh environmental conditions (such as in higher temperature regions), therefore, electrode materials that could attain excellent conductivities at higher operating temperatures are more useful. Additionally, for the spinel family (AB_2O_4-type), the distribution of cations at A and B sites strongly depends on the synthesis routes, calcination, and operating temperatures. Therefore, A.C. and D.C. electrical measurements are performed at pallets of each sample from room temperature (RT) to 200 ºC and 250 ºC, respectively, as shown in Fig. 4.8(a-f). The electrical conductivities are calculated and tabulated in Table 4.2 using the equation (2.5) as described in chapter 2; section 2.2.5.1; where σ is electrical conductivity (A.C./D.C.) in S/cm.

4.2.6.1 D.C. conductivity measurements

To study the D.C. electrical conductivity, the value of activation energies (E_a) is calculated using Arrhenius plots. Figure 4.8(e) shows the linear Arrhenius plot between ln conductivity ($\ln\sigma$) *vs.* temperature (1000/T) from which E_a is calculated using the corresponding Arrhenius equation (2.6) as mentioned in chater 2; section 2.2.5.1. From Table 4.2, it can be seen that the approximated value of activation energy (E_a) is ~0.37eV. However, there is a slight increase in the value of E_a at higher calcined temperatures which could be due to the increment in particle/crystallite size [120], [121]. To calculate D.C. resistance (R_{DC}), V-I curves for all samples are recorded at room temperature from the potential window of -10.0 V to -10.0 V as shown in Fig. 4.8(f). R_{DC} is calculated using the slope of the fitted curve and correspondingly D.C. conductivity (σ_{DC}) is calculated using the equation (2.5) as mentioned in chapter 2; section 2.2.5.1 and tabulated in Table 4.2. It can be seen that for both the synthesis routes σ_{DC} values lie in the range of ~10^{-8} to 10^{-6} S/cm which is due to the hopping of charge carriers between Mn^{3+} and Mn^{4+} ions in the octahedral sites [85]. Furthermore, in both synthesis routes, on increasing calcination temperature, the value of R_{DC} decreases thereby increasing σ_{DC}. Since at higher calcination temperatures, pores as well as voids in the crystal lattice reduces which gives the formation of a larger grain size as it could be confirmed from SEM particle size. This larger grain size affects the reduction in the grain boundary barrier as well as bulk resistances and gives rise to electron scattering loss conditions. Due to this electron scattering, hopping between the charge carriers increases and consequently decreases the resistivity [110], [122]. This result shows that morphology and grain size are major factors that affect the conductivity and can further be confirmed from A.C. measurements.

4.2.6.2 A.C. Conductivity measurements

The cole-cole or complex impedance plots of NMO pallets are studied to understand the conduction mechanism. Figure 4.8(a-d) shows the temperature dependence plot between real of Z (Z’) *vs.* imaginary of Z (Z”) for all the calcined samples and displays two overlapping semicircles as shown in the insets of each Fig. 4.8(a-d), It may be associated with the two resistances. The small semi-circle at high frequencies is associated with the parallel combination of grain capacitance (C_g) and resistance (R_g), while the large semicircle at low frequencies depicts the grain boundary capacitance (C_{gb}) and resistance (R_{gb}) [85], [123]. An equivalent circuit of RC combination has been fitted and is shown in the inset of Fig. 4.8(a) for the observed data with variable temperature. The intercept values of Z’ on the Z’ axis are studied and the value of σ_{AC} is calculated using the equation (2.5) as mentioned in chapter 2; section 2.2.5.1 and tabulated in Table 4.2. The value of resistances reduces as the operating temperature rises from 28 to 150 ºC for all the samples. This, in turn, decreases the relaxation time with enhancement in conductivity following the negative temperature coefficient (NTC) behavior for $NiMn_2O_4$ spinel [85]. However, the small value of R_g confirms that the major conduction is through grain boundaries. Furthermore, the diameter of the semicircle at the high-frequency region for sol-gel route samples was found to be smaller and hence reduce the total area under the curve, which indicates that the conduction in sol-gel (NMOS) samples is predominantly through grains that are also densely interconnected as compared to ball-mill samples as confirmed from TEM micrographs. Additionally, a reduction in the grain resistance with temperature variations also causes an increment in conductivity. Interestingly, at room temperature, NMOB_700 samples show a high value of grain-boundary resistance (50.05 **Ω**) and a low value of grain resistance (7.78 K**Ω**) compared to other prepared samples due to which it has a higher value of conductivity ($2.42 \text{ X } 10^{-5}$ S/cm). This variation of conductivity for NMOB_700 confirms that the calcination temperature has a major role in the conduction process for spinel structures. From the above results, it is inferred that the $NiMn_2O_4$ could be used as an anode electrode as it can still provide high conduction at the RT and higher operating temperatures which is needed in today's environment. However, the variation in conductivity depends on the sample preparation routes as well as grain size and grain boundary could greatly affect the conduction phenomena of Li^+ and e^- in LIBs.

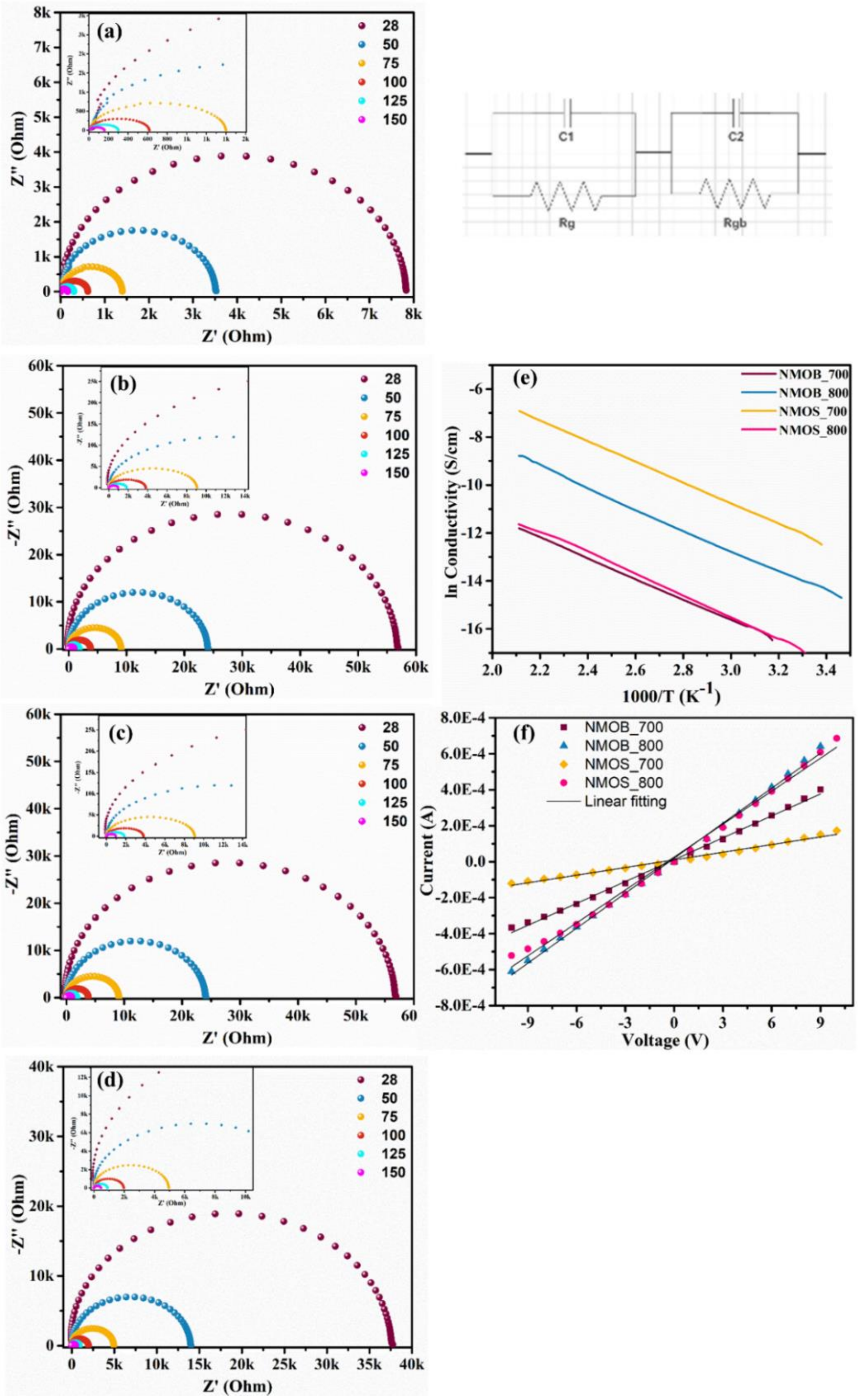

Figure 4.8 A.C. conductivity measurements: (a-d). Complex Impedance Spectroscopy plots measured from ambient temperature to 250 °C in the frequency range of 4 Hz to 8 MHz: (a) NMOB_700, (b) NMOB_800, (c) NMOS_700, (d) NMOS_800, and D.C. conductivity measurements: (e) Arrhenius plot recorded from room temperature to 200 °C of all NMO pallets (f) V-I curves of calcined NMO pallets recorded at ambient temperature in the voltage range of -10 – 10 V.

Table 4.2 A.C. and D.C. electrical parameters of calcined $NiMn_2O_4$ pallets at different temperatures ranging from RT (28 °C) to 150 °C with errors, 2-15%.

Sample	**R_{DC} (KΩ)**	**E_a (eV)**	**σ_{DC} (S/cm)**	**R_{DC}**			**σ_{AC} (S/cm)**
				T (°C)	**R_{gb} (KΩ)**	**R_g (Ω)**	
NMOB_700	24.5	0.3710	7.74 X 10^{-8}	28	7.78	50.05	2.42 x 10^{-5}
				50	3.56	37.32	5.29 x 10^{-5}
				75	1.42	14.50	1.33 x 10^{-4}
				100	0.66	10.03	2.86 x 10^{-4}
				125	0.33	8.20	5.78 x 10^{-3}
				150	0.17	14.93	1.11 x10^{-3}
NMOB_800	15.38	0.3785	1.38 X 10^{-7}	28	53.9	35.47	3.28 x 10^{-6}
				50	22.3	39.01	7.93 x 10^{-6}
				75	8.04	32.33	2.20 x 10^{-5}
				100	3.40	26.85	5.20 x 10^{-5}
				125	1.53	13.21	1.15 x 10^{-4}
				150	0.79	10.68	2.24 x 10^{-4}
NMOS_700	70.4	0.3719	9.6 X 10^{-7}	28	57.8	34.31	4.09 x 10^{-6}
				50	24.2	34.29	9.78 x 10^{-6}
				75	8.79	31.50	2.69 x 10^{-5}
				100	3.85	24.86	6.15 x 10^{-5}
				125	1.86	14.71	1.27 x 10^{-4}
				150	1.01	10.83	2.34 x 10^{-4}
NMOS_800	16.37	0.3872	5.72 X 10^{-6}	28	38.6	33.36	3.69 x 10^{-6}
				50	14.3	34.31	9.99 x 10^{-6}
				75	5.00	24.88	2.85 x 10^{-5}
				100	2.01	14.15	7.08 x 10^{-5}
				125	0.95	10.34	1.50 x 10^{-4}
				150	0.50	8.78	2.84 x 10^{-4}

4.2.7 Electrochemical Measurements

4.2.7.1 Cyclic Voltammetry (CV) Analysis

To understand the electrochemical redox mechanism of hexagonal shape NMO particles, cyclic voltammetry (CV) results of all the samples are measured in the potential range of 0.01-2.0 V at a 0.1 mV/s scan rate as shown in Fig. 4.9(a-b) for 1st and 3rd cycle. In the first anodic cycle, two broad oxidation peaks are observed around ~2.0 V and ~1.3 V for all the samples. These peaks could be attributed to the oxidation of metallic Ni and Mn to Ni^{2+}, and Mn^{3+}, respectively as well as the decomposition of Li_2O [90], [92], [114], [124]. This process can be expressed using the following electrochemical reaction (equation (4.1-4.2)) [90], [114]:

$$Ni + Li_2O \leftrightarrow NiO + 2Li^+ + 2e^- \tag{4.1}$$

$$Mn + Li_2O \leftrightarrow MnO + 2Li^+ + 2e^- \tag{4.2}$$

Consequently, for cathodic scan, there are peaks corresponding to ~0.3 - 0.7 V which could be associated with the overlapped electrochemical reactions of the reduction of Mn^{3+} and Ni^{2+} to Mn and Ni, amorphous Li_2O, and the formation of SEI layer [83], [90], [92], [114], [124]. The corresponding redox equation (4.6) is given in equation (4.3) [90], [92]:

$$NiMn_2O_4 + 8Li^+ + 8e^- \rightarrow Ni + 2Mn + 4Li_2O \tag{4.3}$$

For the third cycle, all the samples show slight shift peaks, which depicts the presence of the insertion mechanism of Li^+ [124]. Hence, reversible reactions take place in the charge-discharge mechanism which could be represented by the following equation (4.4) [90]:

$$2MnO + \frac{1}{3}\ Li_2O\ \rightarrow \frac{1}{3}Mn_3O_4\ + \frac{2}{3}\ Li^+ + \frac{2}{3}e^- \qquad (4.4)$$

Furthermore, it is observed that the value of peak current increases as the calcination temperature increases for both the 1st and 3rd cycle, which shows the electrochemical stability is improved. Also, the higher values of cathodic current than anodic current indicate that the electrodes resist de-insert Li^+ compared to insertion [92]. Here, it is noticed that the intensity of peaks in the case of sol-gel samples for any particular temperature is higher in comparison to ball-milled samples for 1st cycle. However, the case is reversed in cycle 3. Additionally, from the 3rd cycle, it can be seen that the multiple peaks diminished and current intensities decreased as the cycle increased depicting the variation in redox reaction behavior, which thereby may affect the initial and subsequent columbic efficiency as well as rate capability of LIBs [125], [126]. Therefore, it is revealed that the synthesis routes could make significant changes in the electrochemical performance of LIBs.

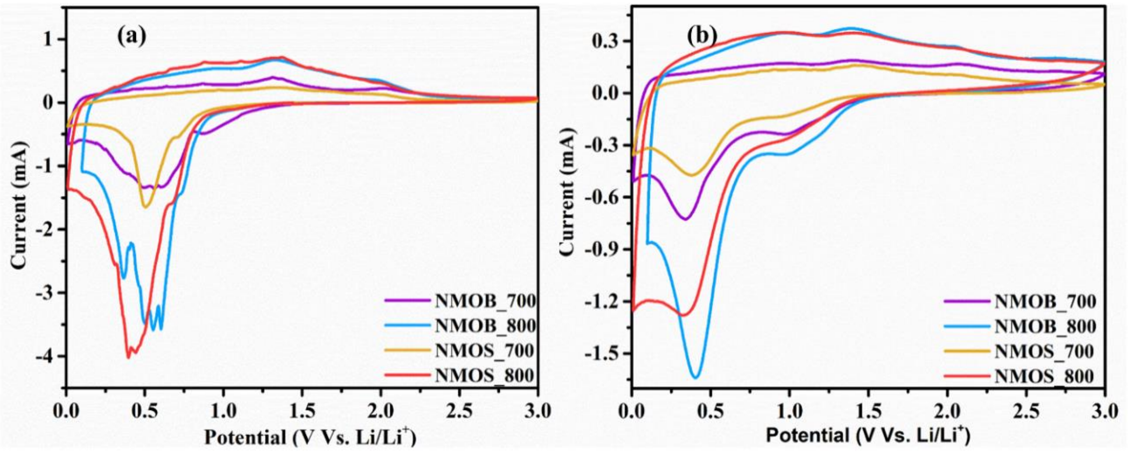

Figure 4.9 CV curves of the synthesized NMOB_700, NMOB_800, NMOS_700, and NMOS_800 samples were recorded within the potential window (0.01-3.0 V) with a 0.1 mV/s scan rate **(a)** for the 1st cycle, and **(b)** for the 3rd cycle.

4.2.7.2 Electrochemical Impedance Spectroscopy (EIS) Analysis

To understand the electrochemical behavior occurring at the electrode-electrolyte surface Electrochemical Impedance Spectroscopy (EIS) has been performed. Figure 4.10 (a-b) presented the Nyquist plots of all the samples before the 1st and after the 200th cycles, respectively together with an equivalent circuit model used for fitting. From initial curves, high-frequency semi-circles represent the SEI film resistance and/or contact resistance (R_s) while a mid-frequency semicircle depicts the charge transfer resistance (R_{ct}) [79], [127]. In the low-frequency region, the oblique line depicts the diffusion of lithium ions into the active material [127]. After the equivalent circuit fitting, Table 4.3 displays the fitted resistance values.

It can be observed that the value of R_s and R_{ct} shows unpredictable variations before and after cycling which could be ascribed to the electrochemical reactions occurring at the electrode interface. Samples prepared using a ball mill show higher resistance values in comparison to sol-gel. Additionally, for ball-milled samples, the value of R_{ct} drastically increases as calcination temperature rises. This indicates that due to the larger particle size in NMOB_800, the diffusion path length for Li^+ is extended, thereby affecting its charge-discharge profiles [79].

Contrary, in sol-gel route samples, NMOS_700 shows a lower value of R_s predicting the formation of the thinnest SEI layer which could thereby escalate the initial capacity of the electrode. However, the value of R_{ct} is nearly the same for all the electrodes except NMOB_800 which shows a much higher value which could result in the slower transfer rate of Li^+/e^- and affect the electrochemical performances. Interestingly, the value of Rs increases with cycles, which indicates the growth of SEI.

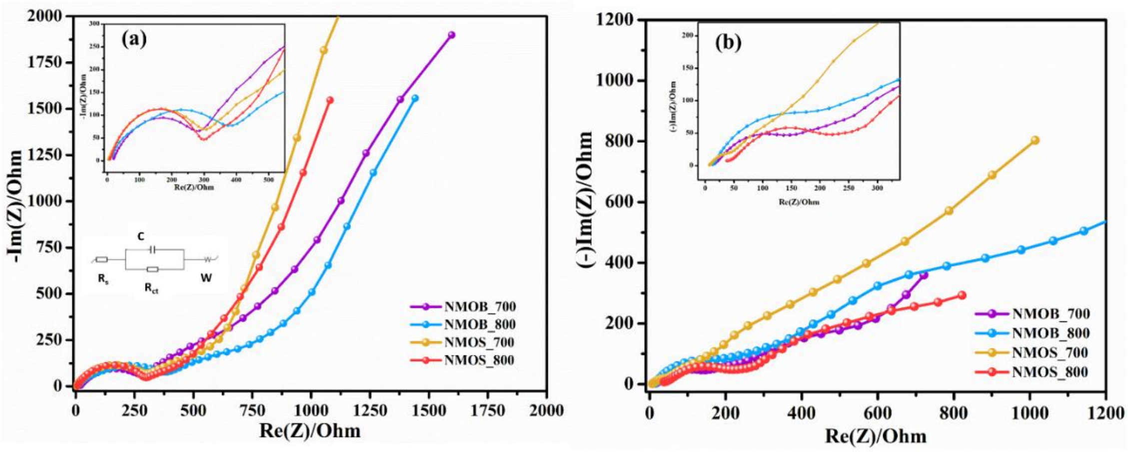

Figure 4.10 Nyquist plots of the NMOB_700, NMOB_800, NMOS_700, and NMOS_800 and recorded at 10 mHz-100 KHz with AC amplitude voltage of 5 mV (a) before 1st cycle, and (b) after 200th cycles, with inset showing an enlarged image of curves.

Table 4.3 EIS analysis of electrodes at 1st and after the 200th cycle recorded from 100 KHz to 10 mHz with the AC amplitude of 5 mV.

Sample	**R_s /Ω (1st cycle)**	**R_{ct}/Ω (1st cycle)**	**R_s /Ω (200th cycle)**	**R_{ct}/Ω (200th cycle)**
NMOB_700	17.80	276.36	10.51	298.85
NMOB_800	6.58	435.39	12.67	335.35
NMOS_700	3.06	286.01	6.81	61.795
NMOS_800	7.78	274.54	37.85	228.3

4.2.7.3 Galvanostatic Charge-Discharge (GCD) Analysis

Figure 4.11 (a-d) displays the 1st, 2nd, 20th, and 50th galvanostatic charge-discharge cycles of all samples recorded at a current density of 100 mA g^{-1} between the potential ranges of 0.01-3.0 V. Furthermore, Fig. 4.11 (e-h) displays the corresponding cycling performance and columbic efficiency for 200 cycles. During the initial discharging, two voltage plateaus are seen at ~0.7V and ~0.5 which follow the CV curve and depict the reduction of Mn^{3+} and Ni^{2+} to Mn, Ni, and amorphous Li_2O. The initial discharge capacity for NMOB_700, NMOB_800, NMOS_700, and NMOS_800 is found to be 1104.02 mAh g^{-1}, 1188.34 mA h g^{-1}, 1661.96, and 1140 mAh g^{-1}with corresponding columbic efficiency of around 57.4%, 54.4%, 57.1%, and 49.9% respectively at the current density of 100 mA g^{-1}. The initial discharge capacities surpass the theoretical capacity (921.93 mAh g^{-1}) following the irreversible capacity loss of around 42.5%, 45.5%, 42.8%, and 50.1% for NMOB_700, NMOB_800, NMOS_700, and NMOS_800 respectively which could be associated with the initial growth of SEI layer, irreversible reactions occurring at the surface, and electrolyte decomposition which instigate the irreversible capacity [128], [129]. It is noteworthy that the CE after the initial cycle begins to rise which shows that the insertion/de-insertion of Li$^+$ in the electrode approaches a stable state. Even after 200 cycles, the discharge capacity is found to be 363, 259, 383, and 183 mAh g^{-1} for NMOB_700, NMOB_800, NMOS_700, and NMOS_800, respectively.

Figure 4.12 (a) shows the cycling performance of the as-prepared NMOB_700, NMOB_800, NMOS_700, and NMOS_800 fresh cells operated at a constant current density of 500 mAh g^{-1} from 0.01-3.0 V potential window for 200 cycles. The first cycle discharge capacities are found to be 1448, 1144, 1529, and 1058 mAh g^{-1} (with ±10-15 mAh g^{-1}) for NMOB_700, NMOB_800, NMOS_700, and NMOS_800 respectively. Among all electrodes, NMOS_700 and NMOB_700 show excellent behaviour compared to others which could be due to the morphologies and crystallinity of the cuboid-like and hexagonal structure of particles. Additionally, the presence of more active sites and Li$^+$ contact at the surface as confirmed through BET, offers higher discharge capacity. In the case of NMOS_700, there is a gradual decrease of discharge capacity (~ 240 mAh g^{-1}) till 60 cycles, afterward, a stable and slight increase in capacity can be seen which reaches the value of 296 mAh g^{-1} within 200 cycles. This rise in capacity could be due to the presence of a slight $NiMnO_3$ phase or more reactive sites might be activated during electrochemical reactions [130]. In contrast, NMOB_700 shows a decrease in the discharge capacity up to 249 mAh g^{-1} till 117 cycles which shows a slightly improved initial performance when compared to NMOS_700. However, the capacity increases to 260 mAh g^{-1} for 200 cycles in the case of NMOB_700. Furthermore, NMOS_800 discharge capacity gradually decreases for a current density of 500 mAh g^{-1}. Additionally, NMOB_800 does not show stable behavior as its capacity increases/decreases over 200 cycles, because of its high R_{ct} values. The observed capacities of NMOB_800 and NMOS_800 are 89, 30 mAh g^{-1} after 200 cycles. From GCD curves, it can be concluded that at lower calcination temperatures, NMO shows better electrochemical performance compared to samples calcined at higher temperatures. However, the slight impurity of the $NiMnO_3$ phase in the NMOS_700 phase is beneficial as compared to the single crystalline phase NMOB_700.

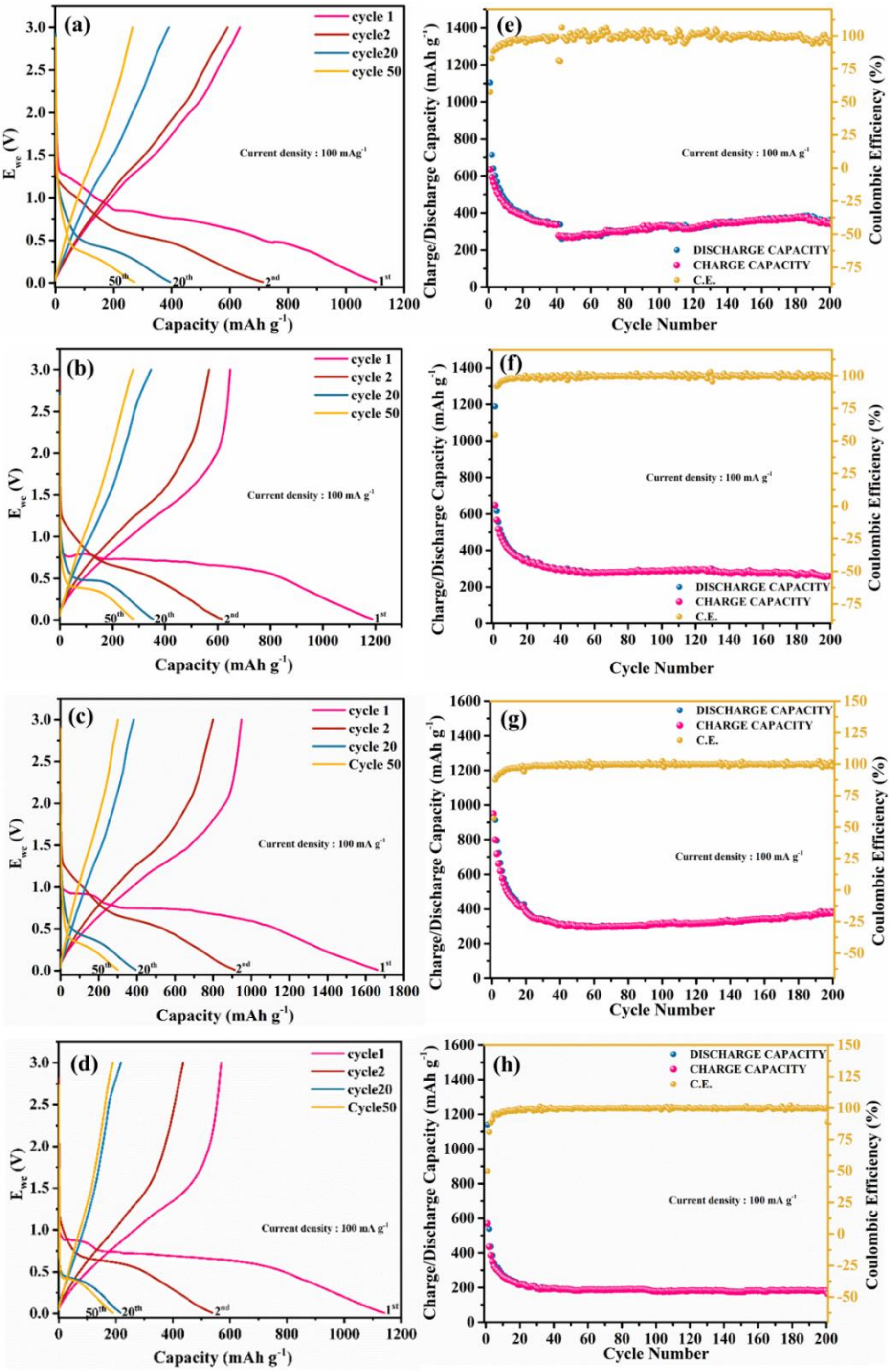

Figure 4.11 (a-d) Charge-discharge cycles and **(e-h)** Cycling curves recorded at 100 mA g^{-1} current density for NMOB_700, NMOB_800, NMOS_700, and NMOS_800 respectively.

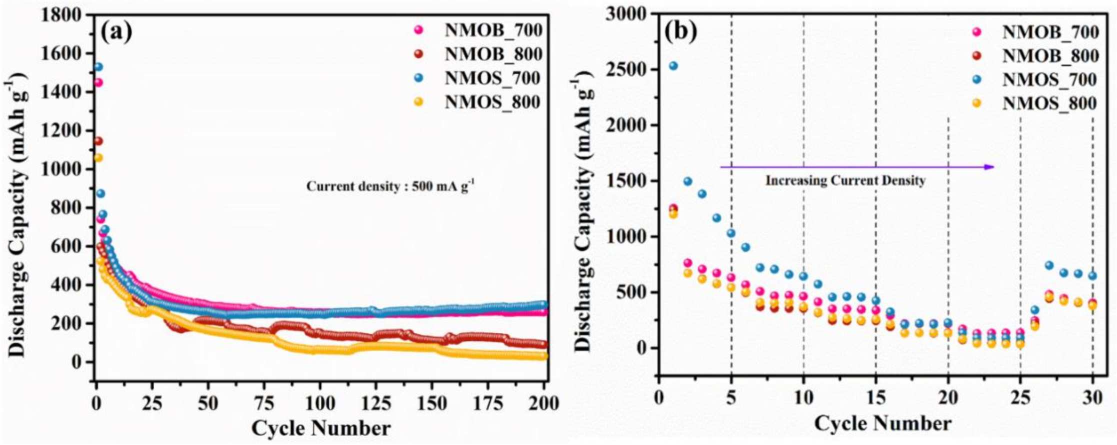

Figure 4.12 (a) Cycling performances of all samples recorded in 0.01-3.0 V voltage window at 500 mA g^{-1} current density and, (b) Rate test graph for the varied current densities from 50 mA g^{-1} to 1000 mA g^{-1} of $NiMn_2O_4$ electrodes.

To study whether the electrodes could operate at variable current rates, rate performance tests of fabricated cells are also measured from lower to higher current rates ranging from 50 to 1000 mA g^{-1} as displayed in Fig. 4.12 (b). Excellent reversibility can be seen even when the current densities reverted from 1000 mA g^{-1} to 50 mA g^{-1}. Among all, NMOS_700 exhibits outstanding rate performance exhibiting the initial discharge capacities of 2531.9, 903.7, 572.0, 323.01, and 135.6 mAh g^{-1}at 50, 100, 200, 500, and 1000 mA g^{-1}, respectively. As the current density is returned to 50 mA g^{-1}, it can still retain 647.07 mAh g^{-1} even after 29 cycles. The results indicate that even after the electrode was operated at high current densities, the structure maintained its stability and electrochemical performance.

Hence. in this section, structural, morphological and electrochemical studies of $NiMn_2O_4$ via two different synthesis routes has been studied. XRD confirms all the samples attain cubic structure with *Fd3m* space group. Additionally, crystallite size in both cases increases as the calcination temperature increases. Morphological analysis confirms the hexagonal-shaped nanoparticles irrespective of synthesis routes. XPS results shows the involvement of multiple oxidation states of Mn and Ni in all the prepared samples. BET confirms as the calcination temperature escalates, surface area is also decreases. AC electrical results confirmed that the major conduction phenomena that occur in all the samples are due to the grain boundaries. Among all samples, the sol–gel synthesized mixed phase sample (NMOS_700, $NiMn_2O_4$-$NiMnO_3$) shows excellent cycling performance due to the mixed phase, morphology, and higher surface area which allows more Li^+ interaction.

Chapter 5

Effect of Cr doping on the $Li_2ZnTi_3O_8$ electrochemical properties as anode

In this chapter, structural, morphological, electrical, and electrochemical studies of Cr-doped and undoped lithium zinc titanate (LZTO), $Li_2ZnCr_xTi_{3-x}O_8$ (x =0, 0.1, 0.3, 0.5) has been investigated as alternative anode using a simple and facile high-temperature solid-state ball-milling route.

5.1 Introduction

Lithium Zinc Titanate (LZTO) has many advantages but still it shows disadvantages such as its poor electronic and ionic conductivity. Therefore, numerous efforts have been made to advance its conductivity and electrochemical performance using different approaches such as preparation of nano-sized material, coating with conductive material, and doping of other ions at different sites like Ag^+ [99], Al^{3+} [100], Cu^{2+} [131], Na^+ [103], Ce^{4+} [101] and many more. Doping can modify the bonding between the atoms by changing its length and strength, introducing the defects/voids into the lattice structure, and also building up the path for lithium-ion diffusion which improvises the migration of Li^+ and e^- within the lattice structure, thereby varying the electronic/ionic conductivity, diffusion coefficient and stability of the materials as well as enhancing the overall electrochemical performance of LIBs [53].

In this study, the synthesis of $Li_2ZnTi_{3-x}Cr_xO_8$(x=0, 0.1, 0.3, 0.5) has been attempted using a solid-state route, and its structural, morphological, and electrochemical properties are reported. The solid-state reaction method is chosen because of its low synthesis cost and simple reaction route. The effect of chromium dopant has been studied at the Ti site over other metal ions, due to its advantages of similar ionic radii with Ti^{4+} as well as the doping of Cr in place of Ti^{3+}/Ti^{4+} in the crystal structure provides more structural stability over octahedral sites in the spinel structure [53]. Synthesis of Cr-doped and pristine Lithium Zinc Titanate ($Li_2ZnTi_3O_8$, LZTO) has been carried out by solid-state reaction route as mentioned in Chapter 2 section 2.1.1.1. Physico-chemical, electrical, and electrochemical characterizations of Cr-doped and pristine LZTO material are performed as mentioned in Chapter 2 section 2.2.

5.2 Result and Discussion

5.2.1 Thermogravimetric and Differential Thermal Analysis (TGA and DTA)

To study the formation mechanism of the LZTO material sample, an as-prepared ball-milled sample was examined by TGA / DTA, and results are discussed in Chapter 3 section 3.1.2.1.

5.2.2 X-ray Diffraction (XRD) Analysis

XRD was performed out to confirm the structural formation and crystalline nature of the samples. Figure 5.1(a) displays the XRD pattern of pristine $Li_2ZnTi_3O_8$ (LZTO) and Cr-doped $Li_2ZnTi_3O_8$, all peaks are well indexed to cubic spinel system matching with JCPDS card no. #086-1512 and confirming the space group, $P4_332$. All the diffraction peaks are sharp indicating the crystalline nature of all samples and confirming that the Cr^{3+} has substituted in the crystal lattice structure. However, as the content of Cr increases to 0.5, a small peak relating to the Cr_2O_3 phase and broadening of peaks can be detected. It indicates that after a certain limit, Cr^{3+} is not able to replace Ti^{4+} in the crystal lattice. Figure 5.1(b) shows the narrow range enlarged diffraction peak of the (111) plane corresponding to the diffraction angle (2Θ), 18.3° for all the samples which confirms the incorporation of Cr^{3+} slightly shifts the peak towards the higher angle side, suggesting the decrease in lattice constant as compared to pristine LZTO. Additionally, 0.3Cr doped LZTO shows sharp peaks compared to other samples, which suggests that this particular doping stabilizes the LZTO structure well. The lattice parameters of pristine and Cr-doped LZTO are calculated and tabulated in Table 5.1. It is observed that the lattice parameter decreases from 8.3689 to 8.3610 which could be associated with the smaller size of Cr^{3+} (0.064 nm) in comparison to Ti^{4+} (0.068 nm). As a result, crystal lattice could be contracted, causing the defects/distortions within the lattice structure, and therefore, it is expected doping increases the lithium-ion diffusivity as well as electronic conductivity of the LZTO samples [53], [100], [101].

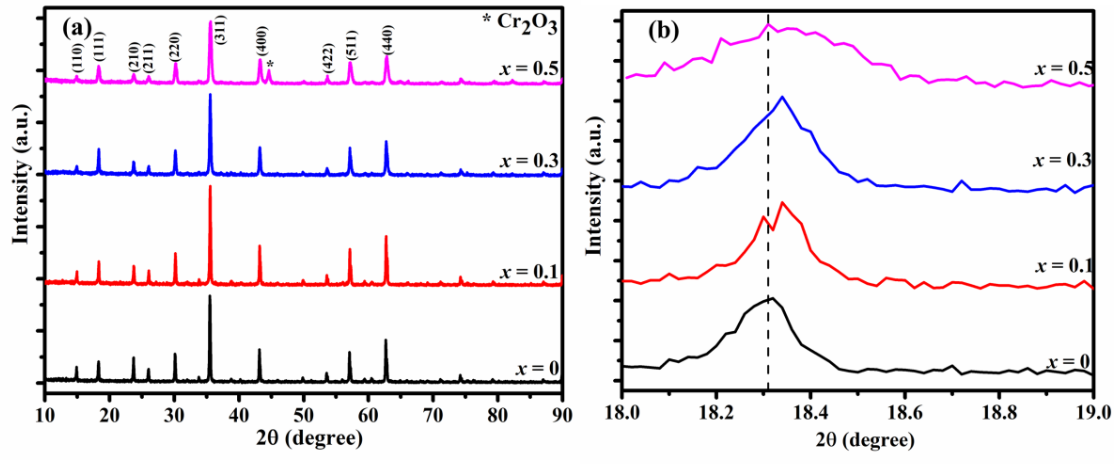

Figure 5.1 (a) Wide range XRD patterns of pristine LZTO (x=0) and doped LZTO with Cr (x=0.1, 0.3, 0.5) prepared at 800 ^{0}C for 5 h, **(b)** Narrow range enlarged peak (111) of synthesized $Li_2ZnTi_{3-x}Cr_xO_8$(x = 0, 0.1, 0.3, 0.5) anode.

Further, for confirmation of size reduction, crystallite size corresponding to the dominant (311) peak has been calculated using Scherrer's formula as described by equation (2.2) in the chapter 2 section 2.2.2.1. Table 5.1 shows that as the content of Cr^{3+} increases, crystallite size decreases linearly which makes Cr^{3+} doping favorable for improved electrochemical performance.

Table 5.1 Structural parameters calculated for undoped and Cr-doped $Li_2ZnTi_{3-x}Cr_xO_8$ (x= 0, 0.1, 0.3, 0.5)

Sample name	Lattice Constant (a=b=c) (Å)	Volume V (cm^{-3})	Crystallite size 'd' (nm)
$Li_2ZnTi_3O_8$	8.3689	586.14	47.25
$Li_2ZnCr_{0.1}Ti_{2.9}O_8$	8.3675	585.86	46.39
$Li_2ZnCr_{0.3}Ti_{2.7}O_8$	8.3629	585.43	35.48
$Li_2ZnCr_{0.5}Ti_{2.5}O_8$	8.3610	584.48	23.60

5.2.3 Scanning Electron Microscopy (SEM) and Transmission Electron Microscopy (TEM) Analysis

SEM micrographs of calcined pristine (0Cr) LZTO and Cr-doped samples (0.1Cr, 0.3Cr, 0.5Cr) are shown in Fig. 5.2(a-d). It is visible from SEM micrographs that the pristine LZTO shows prismatic-shaped agglomerated particles in the sub-micrometer range with a particle size of, 0.1-0.35 μm as calculated by Image-J software. It is noticed that on doping of Cr, there is a decrement in the size of particles as 80-200 nm. It can also be seen that Cr doping also decreases the agglomeration of particles and increases the homogeneity of particles in the material LZTO. The Transmission Electron Microscopy (TEM) images for undoped (0Cr) and doped (0.3Cr) samples are displayed in Fig. 5.3(a-b). The TEM image (Fig. 5.3 a) shows the dense facets of a spherical-shaped polyhedron of pristine LZTO particles which is further modified into clear shape and faces of these spherical polyhedron facets with reduced size and less agglomeration of particles after the doping of 0.3Cr. This improvement in the morphology and particle size could be advantageous in enhancing the electrical conductivities and electrochemical characteristics of LZTO after Cr doping.

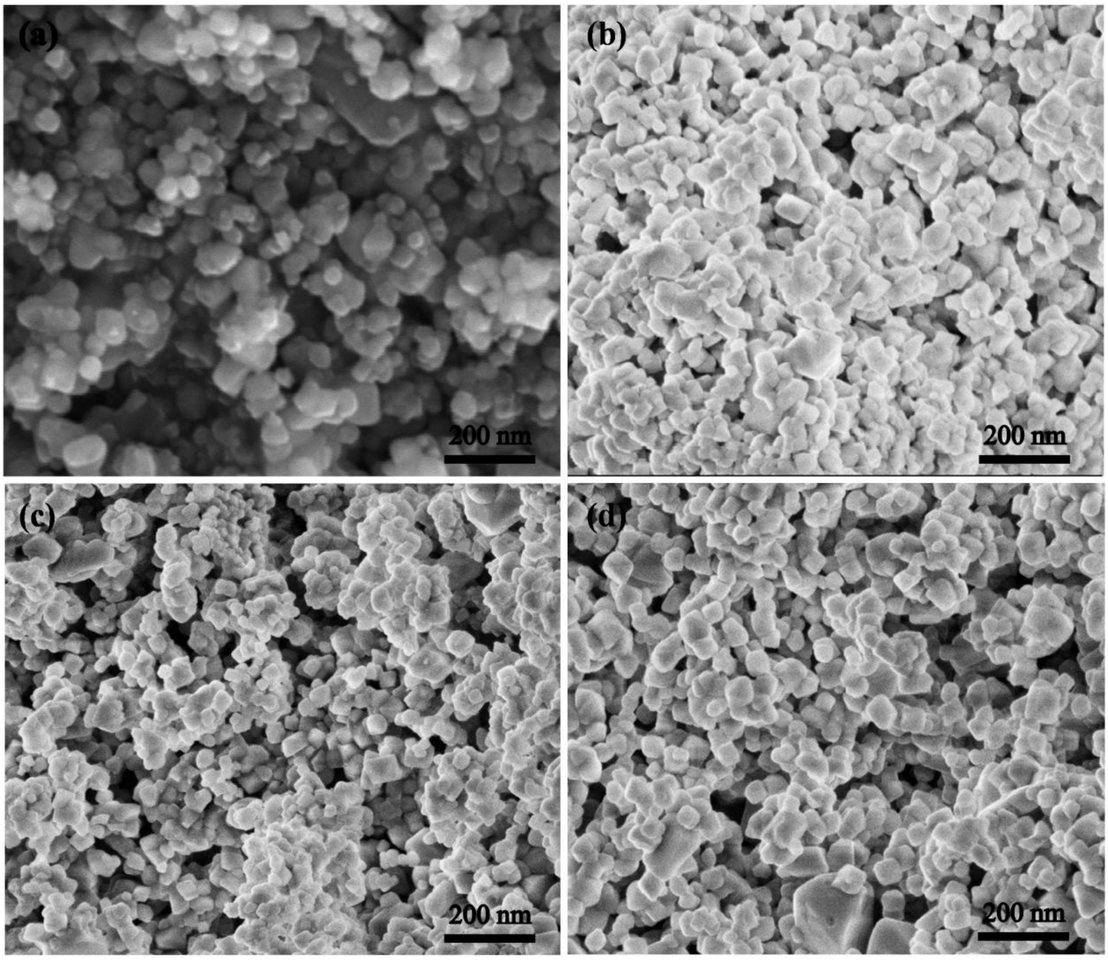

Figure 5.2 (a-d) SEM images at 50X magnification for **(a)** pristine LZTO; Cr doped LZTO at **(b)** x = 0.1, **(c)** x = 0.3, and **(d)** x = 0.5 synthesized at 800 ^{0}C for 8 h in air.

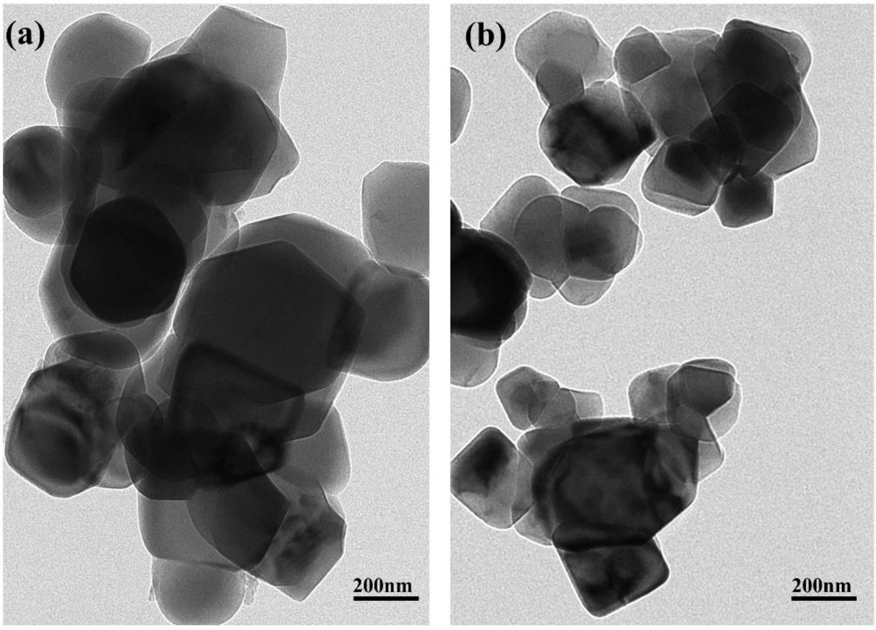

Figure 5.3 TEM micrographs observed for **(a)** pristine LZTO, **(b)** 0.3Cr doped LZTO synthesized at 800 ^{0}C for 8 h in air.

5.2.4 Electrical Measurements

The D.C. conductivity measurement is performed for all the pristine and Cr-doped LZTO samples on the pellets of size and dimensions as given in chapter 2 section 2.2.5 and conductivity is calculated using the equation (2.5) as described in chapter 2; section 2.2.5.1. Activation energy (E_a) is also calculated using the Arrhenius equation (2.6), which is described in chapter 2 section; 2.2.5.1. Table 5.2 displays the electronic conductivity and activation energy for all the samples. It is observed that as the content of Cr doping increases, the activation energy for all the samples decreases, and electronic conductivity increases. This suggests that enhanced electronic conductivity could be favorable for improved electrochemical performance synthesized material as an anode.

Table 5.2 Electrical parameters calculated for $Li_2ZnTi_{3-x}Cr_xO_8$ (x= 0, 0.1, 0.3, 0.5)

Sample	Activation Energy (meV)	D.C. resistance (Ω)	Electronic conductivity (S/cm)
$Li_2ZnTi_3O_8$	997.9	2.60×10^{7}	9.14×10^{-9}
$Li_2ZnCr_{0.1}Ti_{2.9}O_8$	979.2	3.16×10^{8}	6.39×10^{-10}
$Li_2ZnCr_{0.3}Ti_{2.7}O_8$	957.1	1.70×10^{6}	7.46×10^{-8}
$Li_2ZnCr_{0.5}Ti_{2.5}O_8$	991.8	5.70×10^{6}	2.18×10^{-8}

5.2.5 Electrochemical Measurements

5.2.5.1 Cyclic Voltammetry (CV) Analysis

The electrochemical performance of the synthesized samples of pristine and Cr-doped LZTO has been carried out in terms of CV, EIS, and GCD tests. Figure 5.4 (a) and (b) show the CV curves for cycles 1 and 3 of Cr-doped and undoped samples measured between 0.05-3.0 V at 0.05 mV s^{-1} scan rate. Both cathodic and anodic peaks of Cr-doped samples are similar to the pristine LZTO sample, suggesting that doping does not alter the primary electrochemical mechanism of the LZTO material. In the initial cycle, all the curves show cathodic and anodic pair peaks around 1.0-2.0 V, which could be associated with the oxidation reaction of Ti^{4+}/Ti^{3+} during the lithiation/de-lithiation process [63], [74], [95]. Also from the third cycle, it can be observed that peaks shifting toward higher potential is associated with the transition of phase from spinel to rock salt phase [74], [94], [100]. Additionally, from the first to third cycle, the same pattern has been followed by all the CV curves, suggesting that after the initial cycle material stabilizes for further cycles. However, from both curves it can be analyzed that after Cr doping cathodic/anodic peaks current intensifies which indicates that the kinetics of lithium-ion intercalation and de-intercalation improves, thereby increasing the specific capacity of the material. There is also a reduction in peak intensity of around 0.4-0.5 V that is observed for all samples. It is associated with the multiple restoration of Ti^{4+}, which is in good accordance with the other reports [94], [95], [99], [100], [131].

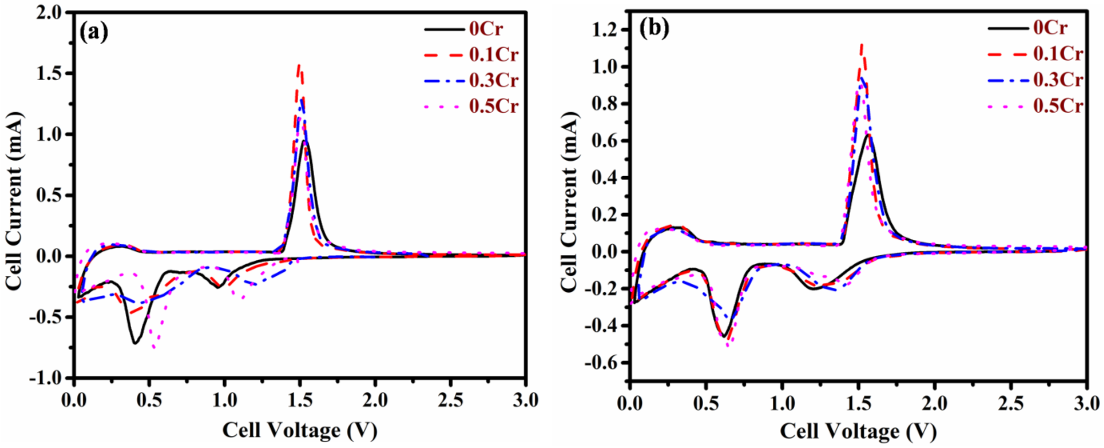

Figure 5.4 Cyclic Voltammograms for **(a)** first cycle, **(b)** third cycle of synthesized $Li_2ZnTi_{3-x}Cr_xO_8$(x= 0, 0.1, 0.3, 0.5) as anode material.

Further, to examine the degree of polarization of the electrodes, potential difference values between the peaks of cathodic and anodic scan for all samples are tabulated in Table 5.3, where V_a and V_c are the potentials of anodic and cathodic peaks, respectively. It can be concluded that Cr doping provides stability during the insertion-extraction process of Li^+, thereby improving the reversibility of electrodes. Among all undoped and Cr-doped sampels, doping of 0.3Cr has the lowest potential difference (320 mV) which shows at this particular doping LZTO possesses the lowest polarization. Therefore, CV curves imply that Cr-doped LZTO improves the kinetic performance as well as has higher reversibility in comparison with the pristine LZTO electrode.

5.2.5.2 Electrochemical impedance spectroscopy (EIS) Analysis

To study the kinetics of lithium ions movement from electrode surface to electrolyte and vice-versa EIS has been performed on all prepared cells of pristine and Cr-doped LZTO. Figure 5.5 shows the Nyquist plots for all the samples before the cycling. The equivalent circuit diagram and narrow range enlarged region of Nyquist plots for better display of impedances of electrodes are shown as the inset in Fig. 5.5. All the plots have depressed semicircles in the high-frequency region and low-frequency region relating to the charge transfer resistance and the diffusion of lithium ions in the electrode material respectively [132], [133]. The Nyquist plots are fitted based on the equivalent circuit which represents solution resistance (R_1), charge transfer resistance (R_2), constant phase element (Q_2), and element used to describe restricted diffusion (M_2). The values of resistances are computed using the line of best fit and provided in Table 5.3. As shown in Table 5.3, sample 0.3Cr has low solution resistance as well as low charge transfer resistance which suggests that this particular doping has low ohmic resistances between electrode/electrolyte interface and has higher electrochemical activity relative to undoped LZTO. Interestingly, 0.1Cr sample resistance values indicate that diffusion of lithium ions is poor at a lower current rate same as 0Cr which can be validated from rate capability results. However, sample 0.5Cr shows intermediate results between both of the doping concentrations. Therefore, it is reasonable that the optimized 0.3Cr sample has the best electrochemical results as compared to the pristine LZTO electrode.

Table 5.3 Potentials and EIS parameters calculated for $Li_2ZnTi_{3-x}Cr_xO_8$ (x= 0, 0.1, 0.3, 0.5)

Samples	**V_a (V)**	**V_c (V)**	**V_{ac} (mV)**	**R_1 (ohm)**	**R_2 (ohm)**	**D_{Li} ($cm^2.s^{-1}$)**
$Li_2ZnTi_3O_8$	1.53	0.95	580	4.19	375.5	1.6×10^{-17}
$Li_2ZnCr_{0.1}Ti_{2.9}O_8$	1.49	0.99	500	6.61	315.9	9.5×10^{-17}
$Li_2ZnCr_{0.3}Ti_{2.7}O_8$	1.51	1.19	320	3.80	68.86	1.8×10^{-16}
$Li_2ZnCr_{0.5}Ti_{2.5}O_8$	1.50	1.09	410	4.60	116.0	8.6×10^{-16}

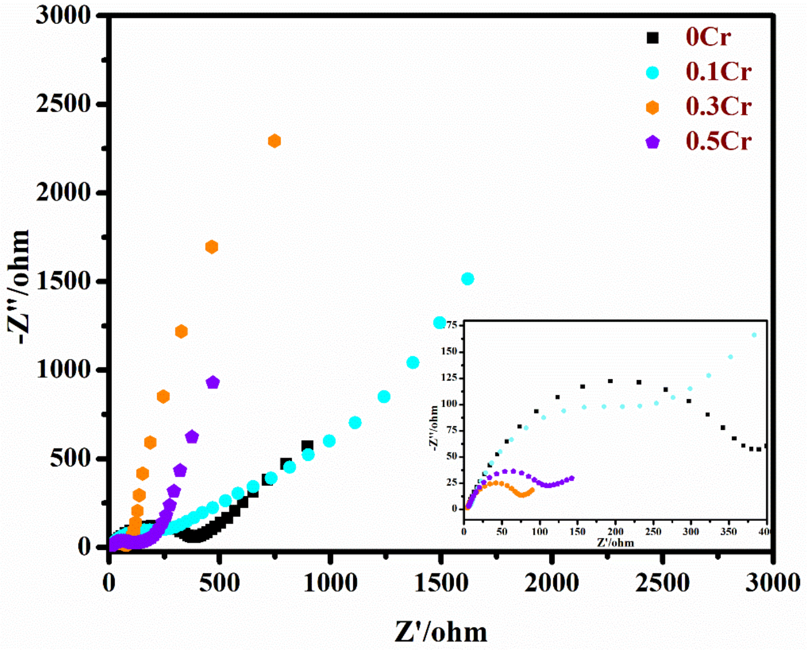

Figure 5.5 Nyquist Plot measured at AC pulse signal of amplitude 5 mV of all samples of $Li_2ZnTi_{3-x}Cr_xO_8$(x = 0, 0.1, 0.3, 0.5) anode.

Diffusion coefficient (D_{Li+}) for all the samples can be calculated based on the relation of restricted linear diffusion which depends on the thickness of the electrode (δ) and diffusion time constant (τ_d) which are related by the equation (5.1) described as:

$$D_{Li^+} = \frac{\delta^2}{\tau_d} \tag{5.1}$$

The calculated diffusion coefficient for all the samples is tabulated in Table 5.3. The diffusivity of lithium ions in electrode material escalates as the content of Cr^{3+} increases thereby improving the chemical kinetics of the reaction during charge/discharge cycles [63], [101].

5.2.5.3 Galvanostatic Charge-Discharge (GCD) Analysis

To study whether those electrodes can function at high-power applications, they are being subjected to varied current rates. Figure 5.6 shows the rate capability of $Li_2ZnCr_xTi_{3-x}O_8$ (x = 0, 0.1, 0.3, 0.5) samples measured at variable scan rates ranging from 0.1C to 2C. There is a difference between first and second-cycle discharge capacities for all samples and after, that capacities are almost the same. This loss in capacity is ascribed to the irreversible reactions that occurred on the electrodes surface or the SEI layer formation which thereby reduces the diffusion of lithium-ion through the material [134]. The first and second cycle's discharge capacity results at different C-rates are tabulated in Table 5.4. Conversely, at 0.5Cr doping, the first discharge capacity is 163.18 mAh g^{-1} at 0.1C which is lower than the pristine (0Cr) LZTO sample. As majorly of lithium ions contribute to the electrochemical energy during the insertion/de-insertion process, it may be possible that there could be the presence of Cr^{3+} at the Li^+ octahedral site rather than Ti^{4+}, which could be a reason to deduct the amount of lithium ions and thereby reduces the initial discharge capacity [135]. However, on increasing the rate of current, 0.5Cr LZTO sample capacity improved while the capacity of pristine LZTO decreased rapidly. It has been noticed from the results shown in Table 5.4 that Cr doping not only boosts the capacity but also stabilizes the electrochemical performance of the material. On comparing the discharge capacities of all the samples of pristine and Cr-doped LZTO, sample 0.3Cr displays improved specific discharge capacities of 251.73±4, 184.34±5, 157.42±5, and 119.03±4 mAh g^{-1} at 0.1C, 0.5C, 1C, and 2C, respectively. These specific discharge capacities at different rates are better as compared to the pristine (0Cr) of specific discharge capacities of 204.59±4, 165.57±4, 139.61±3, and 97.49±3 mAh g^{-1} at 0.1C, 0.5C, 1C, and 2C, respectively. Therefore, it can be observed that the doping of Cr significantly enhances the performance of LZTO material.

Table 5.4 Galvanostatic Discharge capacity of $Li_2ZnTi_{3-x}Cr_xO_8$ at variable C-rate (x = 0, 0.1, 0.3, 0.5) through the first and second cycles.

Sample	**Discharge capacity (mAh g^{-1}) at 0.1C**		**Discharge capacity (mAh g^{-1}) at 0.5C**		**Discharge capacity (mAh g^{-1}) at 1C**		**Discharge capacity (mAh g^{-1}) at 2C**	
	First	**Second**	**First**	**Second**	**First**	**Second**	**First**	**Second**
$Li_2ZnTi_3O_8$	204.59 (±4)	173.10 (±4)	165.57 (±4)	148.96 (±4)	139.61 (±3)	116.45 (±3)	97.19 (±3)	44.63 (±4)
$Li_2ZnCr_{0.1}Ti_{2.9}O_8$	221.51 (±5)	165.91 (±6)	160.26 (±7)	151.45 (±3)	140.61 (±6)	130.76 (±3)	107.10 (±3)	89.78 (±7)
$Li_2ZnCr_{0.3}Ti_{2.7}O_8$	251.73 (±4)	235.34 (±4)	184.34 (±5)	170.37 (±4)	157.42 (±5)	144.41 (±4)	119.03 (±4)	81.28 (±4)
$Li_2ZnCr_{0.5}Ti_{2.5}O_8$	163.18 (±)5	151.41 (±)5	179.51 (±5)	162.13 (±6)	157.64 (±4)	147.4 (±5)	127.21 (±5)	89.21 (±5)

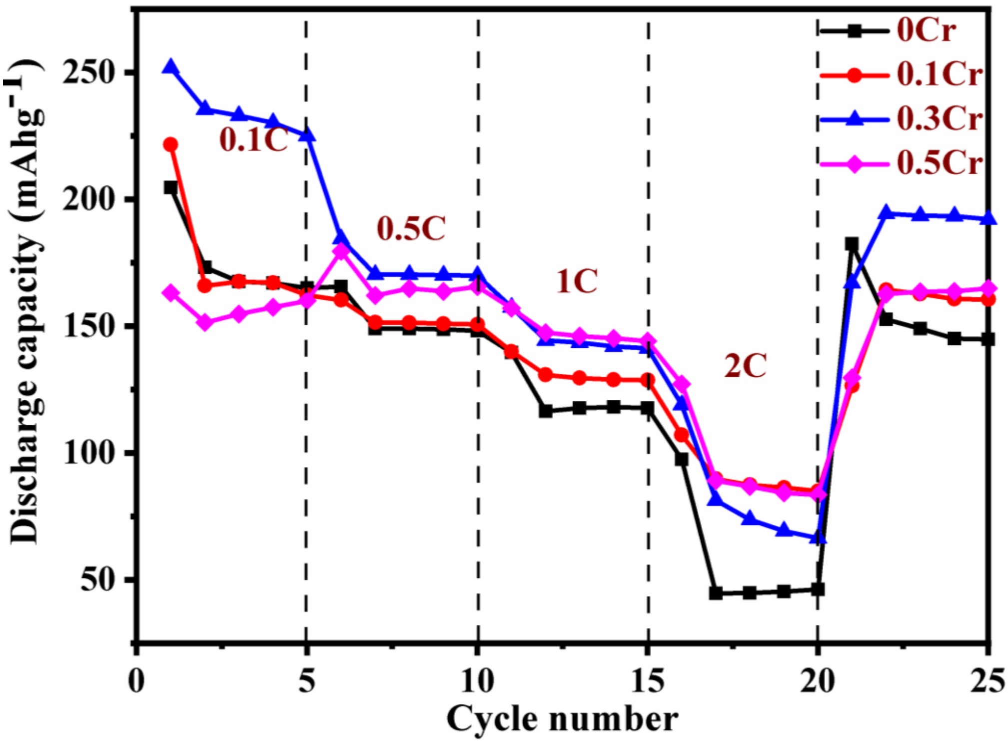

Figure 5.6 Rate performance of $Li_2ZnTi_{3-x}Cr_xO_8$(x = 0, 0.1, 0.3, 0.5) anode recorded at different C-rate ranging from 0.1C to 2C.

Cycling performances and stability are major features to study for battery applications. Figure 5.7 (a) and (b) display the discharge capacities of pristine (0Cr) LZTO and 0.3Cr LZTO at a constant C-rate of 0.1 C. For the first cycle, the discharge capacity is found to be 255.12 mAh g^{-1} for cells made by sample 0.3Cr, which is improved as compared to the pristine sample and discussed in detail in GCD studies. In both cases, it has been observed that due to the formation of the SEI layer, there was a capacity loss after the initial cycle. To investigate the change in capacity with respect to voltage, differential capacities plots are studied. Figure 5.7 (c) and (d) show the corresponding dQ/dV plots for the 2nd, 20th and 50th cycles. From both the curves, it can be observed that there is a shift of dQ/dV peaks (~1.50 V) towards higher potential (~1.72 V) in the case of extraction of Li^+, simultaneously, dQ/dV peaks (~1.30 V) shifts towards lower potentials (~1.21V) during insertion of Li^+. These shifts could be resulted due to the formation of the SEI layer after 2nd cycle at the electrode surface [136]–[138]. Moreover, there is also a reduction peak around ~0.5-0.6 V which could be ascribed to multiple restoration of Ti^{4+}[138] However, from Fig. 5.7(d), in the case of 0.3Cr, this potential shift predominantly decreases which indicates that doping of Cr stabilizes the electrode structure. Additionally, the potential for the 20th and 50th cycles are nearly the same, i.e., 1.50 V and 1.48 V respectively which suggests the improved electrochemical performance after the doping of Cr. Furthermore, it can be seen that as the cycle number increases, the intensity of dQ/dV peaks reduces for both cases, which may be ascribed to the fading of active material electrodes [136]. However, after the doping of Cr, high intense and sharp peaks show the improved reversible nature of the LZTO electrode. Furthermore, the polarization of LZTO material, i.e., ΔV reduces after the doping of Cr ions which is also confirmed by CV results.

Figure 5.7 (e) shows the cycling performance vs. cycle number of both electrodes, depicting that as the number of cycles increases, charge and discharge capacity are almost the same. However, in the case of 0Cr, it can be observed there is a loss in capacity while 0.3Cr shows improved electrochemical performance. To study the efficiency of electrodes to transfer charge during the electrochemical reaction, coulombic efficiency (C.E.) is estimated for 0Cr and 0.3Cr LZTO electrodes as shown in Fig. 5.7(f). C.E. is represented as the ratio of discharge capacity after a full charge to the charge capacity for the same cycle. From Fig. 5.7 (f), it can be seen that the coulombic efficiency is maintained at ~98-99% after the 3rd cycle for the 0.3Cr LZTO sample, while, for 0Cr it varies. To study the ability of the material to retain the stored charge, capacity retention (C.R.) is calculated for both electrodes which is given as the ratio of the measured discharged capacity of two successive cycles, i.e., cycles n+1 and n. Fig. 5.7(f) also displays the C.R. for 0Cr and 0.3Cr electrodes. For the 40th cycle, $Li_2ZnTi_{2.7}Cr_{0.3}O_8$ sample still holds 211.64 mAh g^{-1} with ~99% capacity retention. The discharge capacity of 0.3Cr is higher and more stable in comparison to 0Cr, which may be due to the reasons: (1) reduction in particle size shortens the pathlength for lithium ions and electrons migration within the active electrode, and (2) enhanced electronic conductivity and lowering in the resistances allows the rapid Li^+ intercalation/de-intercalation. This result reveals that the Cr-doped sample exhibits a higher discharge capacity than the pristine sample.

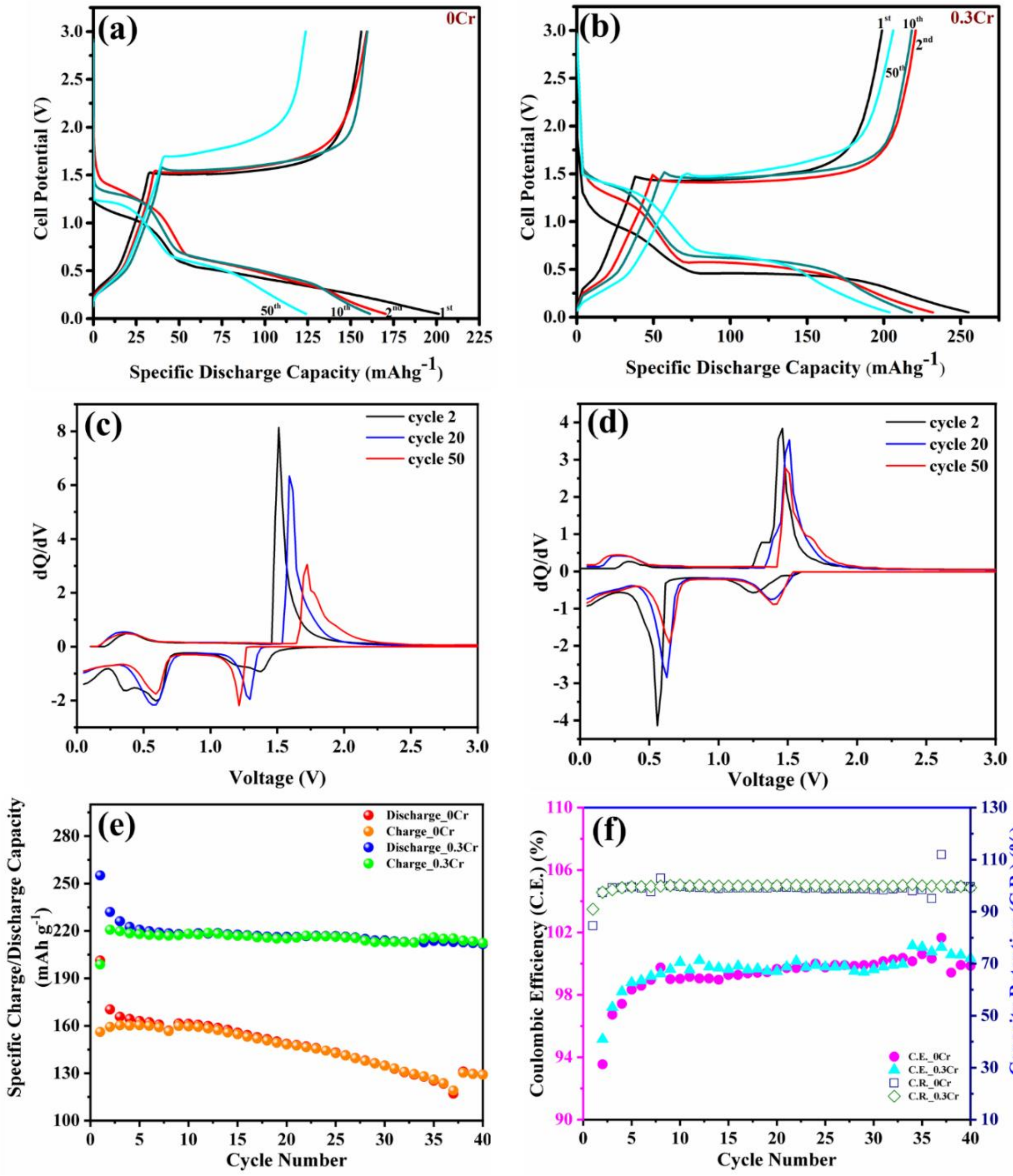

Figure 5.7 First cycle charge-discharge performance of cell tested for cycling analysis: **(a-b)** Pristine (0Cr) and 0.3Cr doped LZTO samples at 0.1C respectively, **(c-d)** Corresponding dQ/dV plots of 2nd, 20th, and 50th cycle of 0Cr and 0.3Cr doped LZTO, **(e)** Cycling performance, and **(f)** Coulombic efficiency vs. cycle number and capacity retention vs. cycle number of 0Cr and 0.3Cr LZTO anode.

Therefore, in this chapter, effect of Cr-doping in $Li_2ZnTi_3O_8$ samples was investigated. The structural analysis shows that doping of Cr does not affect the crystalline nature of pristine LZTO to a certain limit. Morphological analysis displays that as the content of

Cr increases in LZTO, it results in spherical polyhedron-shaped facets with reduced size and agglomeration. From electrical results, it is confirmed that 0.3Cr doped sample attains better electrical performance as compared to pristine LZTO. The electrochemical analysis reveals that $Li_2ZnCr_{0.3}Ti_{2.7}O_8$ shows improved specific capacity for LIBs.

Chapter 6

Investigation of MoS_2 and $NiMn_2O_4$-MoS_2 composite as anode material

This chapter is divided into two parts. In the initial part, pristine MoS_2 structural, morphological, and electrochemical studies have been investigated. In the second part, $NiMn_2O_4$-$NiMnO_3$@MoS_2 composite structural, morphological, and electrochemical studies have been studied.

6.1 Introduction

In recent years, transition metal disulfides such as AS_2 (where A is Mo, Sn, W and Zr) have been attracted attention to replace commercialized graphite due to its similar layered structure to graphite in which S-A-S atoms are held up by weak van der Waals forces [139]–[141]. Among them, MoS_2 have been much explored because of its transfer of four electrons during redox reactions at lower potential. Additionaly, weak interlayer arrangement of spacing which is around ~0.7 nm gives the path for lithium ions to transport between them giving high theoretical capacity (~670 mAh g^{-1}) [139], [140].

In general, MoS_2 exists in many phases (1H, 2H, 1T, and 3R) but two of them have been extensively studied for LIBs i.e. 2H trigonal prismatic and 1T metallic octahedral structure [142]. 1T phase of MoS_2 has the 10^5-10^7 times higher electrical conductivity in comparison to the 2H phase, however, 2H MoS_2 has been mostly studied because of its structural stability [142], [143]. Although, the 2H structure is the most stable but it still suffers from loss in capacity due to its poor conductivity [143], [144]. On the other hand, the 1T phase improves the diffusion of Li^+ and e^- but it has a metastable state [143], [144]. Therefore, the mixture of both phases 2H/1T has been explored as an anode for LIBs.

Contrary, conversion mechanism-based transition metal oxides (TMOs) show potential towards LIBs, attaining high capacities (700-1200 mAh g^{-1}) [145]. Among the other TMOs, Mn-Ni based oxides have been much explored in this research work because of their superior theoretical capacities, low lithiation potential (~0.4 V), and cost-effectiveness. However, its disadvantages such as poor conductivity and volume expansion, result in capacity fading and poor rate performances occur. One way to solve these difficulties is to synthesize nano-sized structures which can provide increased surface area for the insertion of Li^+ and lessen the diffusion path of Li^+. Another solution is to make a composite with other conductive materials. MoS_2 2D-layered structure can provide more space for Li^+ insertion and its high theoretical capacity makes it an ideal candidate for the composite. However, the aggregation and re-stacking of MoS_2 nano-sheets compromised its rate capability. Thus, a novel and innovative composite of both materials could be studied to overcome the limitations of materials. The designing of $NiMnO_3$-MoS_2 composite electrodes resolves the single material shortcomings in terms of stability, cyclability, and rate performance. $NiMn_2O_4$ (NMO) nanoparticles between the MoS_2 sheets suppress the volume expansion of NMO and it may solve the issues regarding the restacking in MoS_2 as well.

In this investigation, the one-step hydrothermal process of the mixed phase (2H/1T) MoS_2 nanoflowers has been reported. Duraisamy and their team reported that the ratio of Mo and S precursors and temperature have great effects on the final products. In this study, the 1:4 molar ratio of precursors of Mo and S are hydrothermally treated at 200 ^oC. After that, synthesis of $NiMn_2O_4$-$NiMnO_3$@MoS_2 nano-composite has been attempted using the facile and low-cost two-step strategy. Hence, we have studied the structural, morphological and electrochemical properties of MoS_2 and $NiMn_2O_4$-$NiMnO_3$@MoS_2 composite as an anode material for LIBs.

Synthesis of MoS_2 has been carried out by hydrothermal route as mentioned in Chapter 2 section 2.1.3.1. Physico-chemical, electrical, and electrochemical characterizations of

MoS_2 and $NiMn_2O_4$-$NiMnO_3$@MoS_2 materials are performed as mentioned in Chapter 2 section 2.2.

6.2 Part A: Electrochemical Studies of hydrothermally synthesized mixed-phase MoS_2 nano-flowers for Lithium-ion Batteries

6.2.1 Results and Discussion

6.2.1.1 X-ray Diffraction Analysis (XRD)

XRD result of the as-prepared MoS_2 is displayed in Fig. 6.1 (a). It can be seen that sharp and intense peaks present at 14.14º, 49.83º, 32.5º, and 39.5º corresponding to (002), (105), (100), and (103) planes were indexed to the hexagonal phase MoS_2 (JCPDS card no.: 00-037-1492) with space group P63-mmc respectively. The sharp peak at the (002) plane with an interlayer spacing of 6.15 Å indicates the crystalline layered structure of pure MoS_2 [146]. Additionally, the peak corresponding to the plane (100) depicts the Mo-S edges stacking in vertical planes and number of S active ions present at edges [146]. In general, annealed samples show crystallinity but in this study, as-prepared samples show pure and crystalline MoS_2 which could be due to the ratio of Mo and S precursors.

However, the main focus is to check the formation of the 1T phase, Raman spectroscopy has been performed after the phase purity. From literature review, Raman spectroscopy is the fingerprint tool to differentiate between both the 2H and 1T phases of MoS_2. Figure 6.1 (b) shows the Raman spectrum observed in the range of 100-700 cm^{-1} recorded at ambient temperature. It can be observed that the multiple peaks confirm the presence of both the 2H and 1T phases. Peaks observed at 376 cm^{-1} and 403.6 cm^{-1} were associated with the E^1_{2g} and A_{1g} in-plane and out-of-plane vibrational modes of 2H-MoS_2, respectively [147], [148]. The octahedral arrangement of Mo atoms in the 1T phase is represented by an E^1_g peak at 279 cm^{-1} [143]. The peaks at 145 cm^{-1}, 235 cm^{-1}, and 334 cm^{-1} corresponding to the longitudinal acoustic J_1, J_2, and J_3 phonon modes, respectively and reveal the formation of 1T metallic phase [147], [148]. The J_1 vibration mode is ascribed to the in-plane and out-of-plane Mo motion inside and in the zig-zag chain, respectively [143]. While the J_2 and J_3 modes related to the S atom layer motion and tendency of the zig-zag chains broken respectively [143]. A small peak at 662 cm^{-1} is associated with the B_{2g}/B_{3g} characteristic mode corresponding to the asymmetrical stretching of O-Mo-O bonds revealing the slight existence of intermediate product MoO_3 [143]. Hence, the presence of both phases of MoS_2 could be advantageous in improving the electrochemical performance of LIBs.

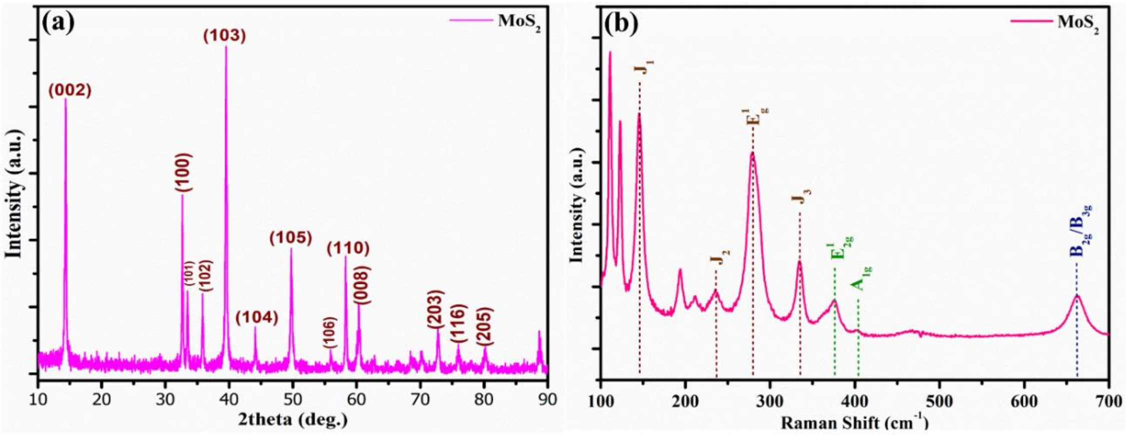

Figure 6.1 a) Wide range XRD pattern of as-prepared MoS_2 recorded from 10º-90º, and b) Raman spectrum of MoS_2 observed in the range of 100-700 cm^{-1} at ambient temperature.

6.2.1.2 Scanning Electron Microscopy (SEM) and Energy-Dispersive X-ray Spectroscopy (EDX) Analysis

SEM micrographs of as-prepared MoS_2 at different magnifications are displayed in Fig. 6.2 (a-c). It can be observe that nanosheets are structured together to form nanoflowers with slight agglomeration. The formation of a flower-like structure and its aggregation is due to surface energy [148]. As the ratio of thiourea precursor is taken greater, the final solution is basic which blocks the lamellar growth in the <100> direction. Thus, nanosheets formed due to the MoS_2 growth in two directions only and are connected by van der Waal forces [149], [150].

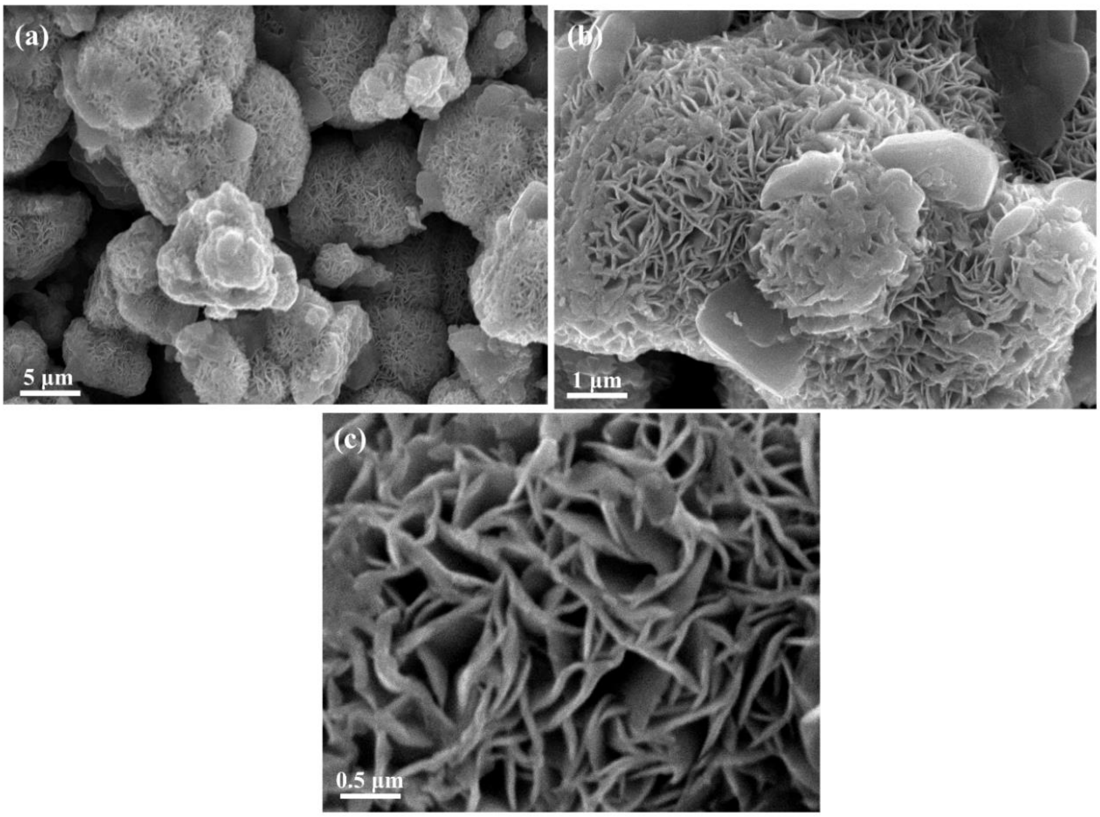

Figure 6.2 (a-c) SEM micrographs of as-prepared MoS_2 recorded at different magnifications.

Based on the reported literature [139], [149], [151], the formation of nanoflowers involved a complex process involved in experiments. Firstly, hydrolysis of thiourea and Na_2MoO_4 occurs to form H_2S and MoO_3 respectively, as given in equation (6.1). In this experiment, thiourea acts as a sulfur source as well as a reducing agent, which helps in the reduction of Mo(VI) to Mo(IV) as given in equation (6.2). At last, the formation of MoS_2 occurs according the reaction given in equation (6.3);

$$\mathrm{NH_2CSNH_2 + 2H_2O \rightarrow H_2S + 2NH_3 + CO_2} \qquad (6.1)$$

$$\mathrm{Na_2MoO_4 + H_2O \rightarrow MoO_3 + 2NaOH} \qquad (6.2)$$

$$\mathrm{4Na_2MoO_4 + 15CS(NH)_2 + 6H_2O \rightarrow 4MoS_2 + Na_2SO_4 + 6NaSCN + 24NH_3 + 9CO_2} \qquad (6.3)$$

Hence, the nanoflowers channels like structure may provide more electrolyte penetration and consequently, improve the electrochemical performance of LIBs.

To confirm the existence of elements and their distribution, EDX is conducted. Figure 6.3 (a-b) shows the EDX mapping and spectrum respectively, revealing the presence of Mo, S, and O elements. From Fig. 6.3 (a) and wt.% (or at.%), it can be seen that the presence of O is very minute in comparison to Mo and S elements which validates the small peak of MoO_3 in the Raman analysis.

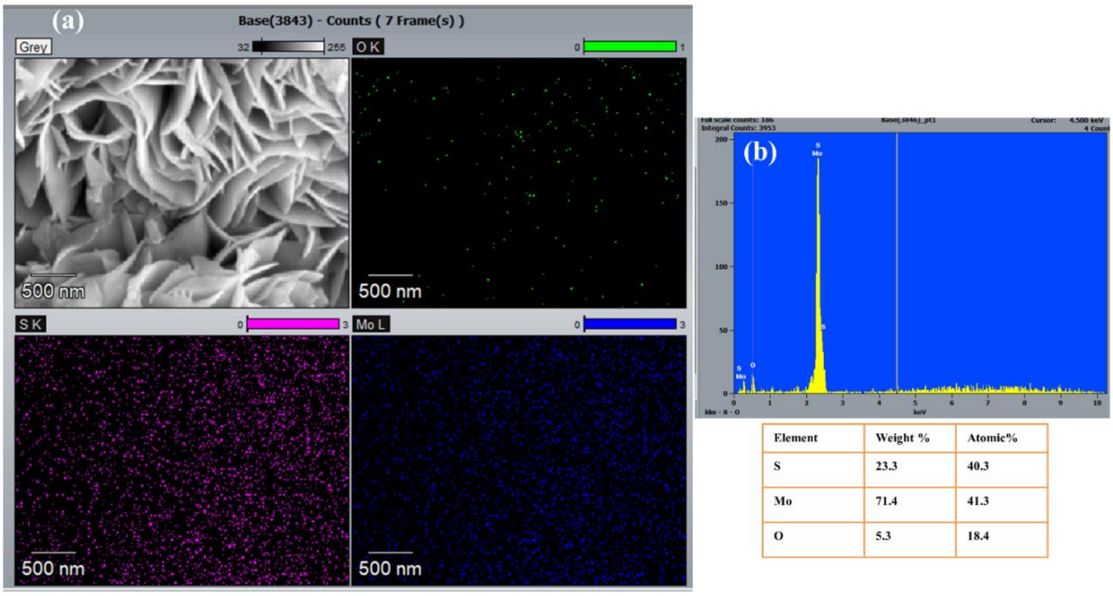

Element	Weight %	Atomic%
S	23.3	40.3
Mo	71.4	41.3
O	5.3	18.4

Figure 6.3 (a) EDX mapping of Mo, S, O and (b) Spectrum with atomic% and weight% of as-prepared MoS_2.

6.2.1.3 Electrochemical Measurements

6.2.1.3.1 Cyclic Voltammetry (CV) Analysis

The electrochemical properties of MoS_2 nanoflowers are investigated using cyclic voltammograms (CVs). Figure 6.4 (a) shows the typical CV curve of 1T-2H MoS_2 nanoflowers for three cycles recorded at 0.05 mV s^{-1} within the potential range of 0.01-3.0 V. In the initial cycle, there exist two peaks at ~0.4 and ~1.4 V in the cathodic scan. The highly intense peak at ~0.4 V attributed to the conversion mechanism of Li_xMoS_2 to metallic Mo and amorphous Li_2S [140], [150], [152]. The peak around ~1.4 V depicted the Li^+ intercalation into the of MoS_2 layers of the formed Li_xMoS_2, consisting the coordination polyhedron of Mo atoms which transforms from trigonal prism to an octahedron [153]. In case of anodic scan, two oxidation peaks appears at ~1.7 and ~2.3 V which is alike for the further cycles which are associated with the oxidation of Mo into MoS_2 and Li_2S to S respectively [152]–[155]. However, in the second cathodic scan, peak centered at ~0.4 V vanishes and different peak appear around ~1.9 V corresponding to the reduction of elemental S with Li to form Li_2S [148], [152], [154]. Furthermore, after first cycle, CV curves are quite similar which suggest the MoS_2 material delivers outstanding reversibility following the electrochemical reaction mechanism equations (6.4 - 6.7) [155]:

$$\mathrm{MoS_2 + xe^- + xLi^+ \rightarrow Li_xMoS_2} \tag{6.4}$$

$$\mathrm{Li_xMoS_2 + (4-x)e^- + (4-x)Li^+ \rightarrow 2Li_2S + Mo} \tag{6.5}$$

$$\mathrm{2Li_2S + Mo \rightarrow MoS_2 + 4e^- + 4Li^+} \tag{6.6}$$

$$\mathrm{2Li_2S \rightarrow 2S + 4Li^+ + 4e^-} \tag{6.7}$$

To further study the electrochemical performance, pseudocapacitive contribution analysis was examine via diffusion and capacity controlled contribution involved in reaction kinetics of the cycling performance of MoS_2 electrodes. CV was performed at different scan rates of 0.05, 0.1, 0.2, 0.3, and 0.4 mV s^{-1} in the potential window of 0.01-3.0 V as shown in Fig. 6.4 (b). It can be observe that as the scan rate increased, the area under the CV curve increased. To examine the current contributions, the following equations (2.9 – 2.13) was used as described in chapter 2; section 2.2.6.4; which depicts the relation between peak current (i) and scan rate (v).

The value of b, if close to 0.5, shows the reaction is dominated by diffusion-controlled while if it's close to 1, it depicts the pseudocapacitive behaviour [155]. The plot of log scan rate and log peak current was plotted to find the value of b using the slope as shown in Fig. 6.4 (c). The values of b obtained were to be 0.52, 0.78, 0.64, 0.68 for cathodic peak 1 and 2, and anodic peak 1 and 2 respectively indicated the crystalline 2H/1T MoS_2 acquired pseudocapacitive behavior. For quantitative analysis of current contributions in the CV curves, equation (2.13) was used as mentioned in chapter 2; section 2.2.6.4. The values of k_1 and k_2 are calculated and percentage of capacitive and diffusive contributions for different scan rate is calculated.

Figure 6.4 (d) depicts the capacitive and diffusive contributions for 0.4 mV s^{-1} scan rate which is plotted using the values of k_1 and k_2. Furthermore, Fig. 6.4 (e) shows the variation of diffusive and capacitive contributions for varied scan rates. It can be observed that as the scan rate increases, capacitive contribution is increasing by reducing the diffusion controlled current which suggest that the majorly contribution of charge is due to the surface redox reaction occurring at MoS_2 electrodes.

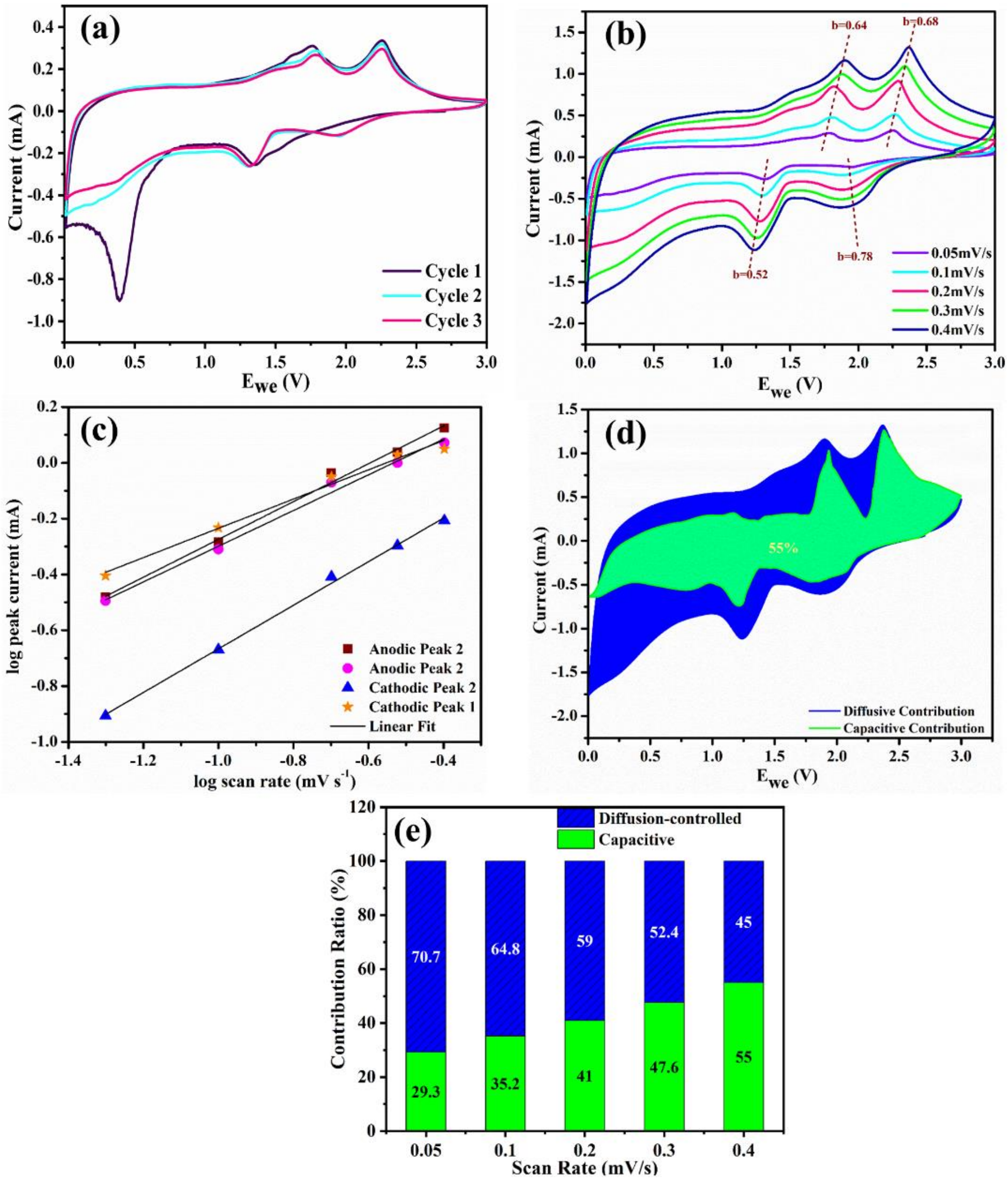

Figure 6.4 (a) Cyclic voltammograms of the 1T-2H MoS_2 electrodes at 0.1 mV/s for three cycles, (b) CV curves recorded at different scan rates from 0.05 – 0.4 mV/s, (c) plot of log (scan rate) vs. log (peak current) for anodic and cathodic peaks (d) the capacitive (green) and diffusive (blue) contribution of 1T-2H MoS_2 0.1 mV/s scan rate, and (e) the diffusive and capacitive contribution ratio calculated for different scan rates.

6.2.1.3.2 Galvanostatic Charge-Discharge (GCD) Analysis

Figure 6.5 (a) and (b) shows the gcd curves with corresponding dQ/dV plots recorded at current density of 500mA g^{-1} for 1st, 2nd, 10th, and 50th cycles within the voltage limit of 0.01 to 3 V. It can be observed that the voltage plateaus as shown in GCD curves and dQ/dV plots are following the CV curves. Additionally, as the cycle number increases, it can be observed that the intensity of dQ/dV curve reduces in anodic-cathodic reactions, confirming the decrement in the capacities. The initial discharge and charge capacity is around 1018.16 mAh g^{-1} and 718.8 mAh g^{-1} (± 10-12) at 500 mA g^{-1} with irreversible capacity loss of 29.5% and initial coulombic efficiency of 67.5%. In the initial cycle, the capacity loss is due to the solid electrolyte interphase layer formation during the charge-discharge process. It can also be seen that MoS_2 electrode still attain discharge capacity around 386.20 mAh g^{-1} at 500 mA g^{-1} even after 50 cycles which could be due to the morphology of nanoflower which allows intercalation of more active sites to Li ions.

Furthermore, to check the cyclability of MoS_2 electrode the cells are subjected to a current density of 500 mA g^{-1} for 500 cycles as shown in Fig. 6.5 (c). It can be observed that the discharge capacity is gradually decreasing till 200 cycles and after that the cycling performance is stable. In addition the inset of Fig. 6.5 (c) shows the reversible nature of MoS_2 electrode, it even maintained coulombic efficiency around ~98% even after 300 cycles.

In addition, to check whether the MoS_2 can operate at higher charge-discharge current rates, it is investigated at current densities varied from 100 to 2000 mA g^{-1} within the voltage window of 0.01-3.0 V as depicted in Fig. 6.5 (d). The initial discharge capacities are 882.76, 560.02, 442.54, 347.83, 240.35, and 438.70 mAh g^{-1} at varied current density of 100, 200, 500, 1000, 2000, and back to100 mA g^{-1} respectively. From Fig. 6.5 (d), it can be observe that after first cycle discharge and charge capacities are stable as well as nearly same, which shows the stable behaviour of MoS_2. These results confirms that MoS_2 electrode can be operated at higher current densities while maintaining the stability of structure and improving electrochemical performance as anode material.

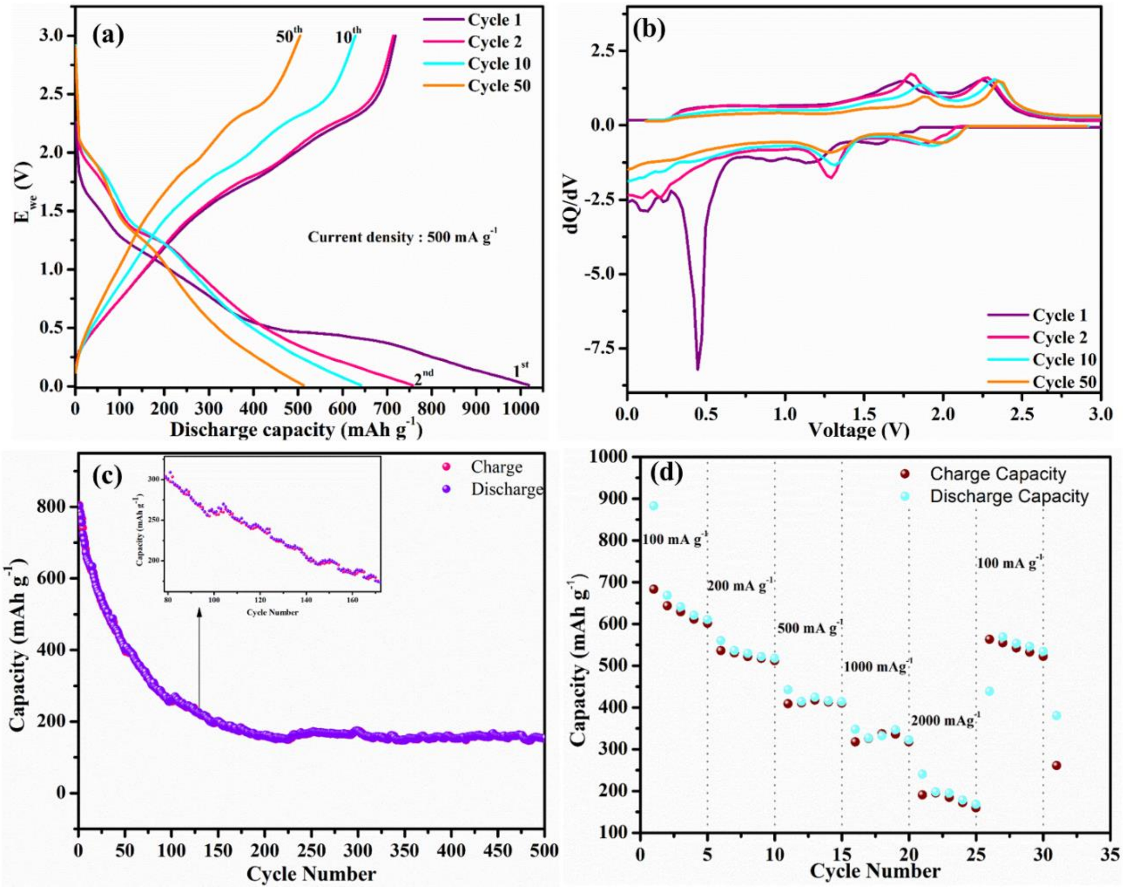

Figure 6.5 (a) Charge-discharge profiles of MoS_2 for 1st, 2nd, 20th, and 50th cycle numbers at the current density of 500 mA g^{-1}, **(b)** dQ/dV plot corresponding to gcd profiles, **(c)** Cyclability performance of MoS_2 electrode for 500 cycles, and **(d)** Rate capability test of MoS_2 electrode at different current rates.

In this section, we have successfully studied the physico-chemical and electrochemical properties of prepared 2H/1T MoS_2 material using the hydrothermal method. Morphological analysis confirms that the nanosheets are agglomerated together to form nanoflowers like structure. The presence of Mo, S and O elements is also confirmed using the EDX analysis. CV and charge-discharge curves confirms the reversible nature of MoS_2 electrodes when tested at varied scan rates and current densities respectively.

6.3 Part B : Preparation of $NiMn_2O_4$-$NiMnO_3$@MoS_2 nano-composites and investigation of electrochemical performances as anode material

6.3.1 Preparation of Composite

Initially, MoS_2 suspension was ultrasonically mixed with ethanol as solvent. The MoS_2 solution was aged for 3-4 days and after aging, NMO-pristine nanoparticles were mixed and dried at 80 °C. When the solution remains a little, it was dried at 80 °C overnight. The black-colored sample was grinded, and collected for testing as an anode without any further modifications.

6.3.2 Results and Discussion

6.3.2.1 X-ray Diffraction Analysis (XRD)

Figure 6.6 displays the wide range (10° - 90°) XRD pattern of $NiMn_2O_4$-$NiMnO_3$@MoS_2 at room temperature. For comparison, XRD patterns of pristine $NiMn_2O_4$ (NMO-pristine) and MoS_2 data are also displayed. All the peaks of composite and pristine samples are sharp in nature, it reveals the crystalline nature of the materials. NMO-pristine diffracted peaks are well indexed to JCPDS no. 01-074-1865, acquiring cubic structure with *Fd3m* space group. Similarly, MoS_2 diffracted peaks depict the formation of a hexagonal structure with a $P6_3mmc$ space group (JCPDS no. 00-037-1492).

However, after the treatment with MoS_2 suspension, the composite consists of diffracted peaks of NMO with a slight presence of rhombohedral $NiMnO_3$ phase (JCPDS no. 01-075-2089). Furthermore, a broad peak of MoS_2 at 14.14° corresponds to the (002) plane confirming the hybrid formation of phase. Hence, the prepared composite depicts a crystalline structure that may be advantageous for Li^+ and e- transportation by providing a short pathlength between the nanoparticles and nano-sheets.

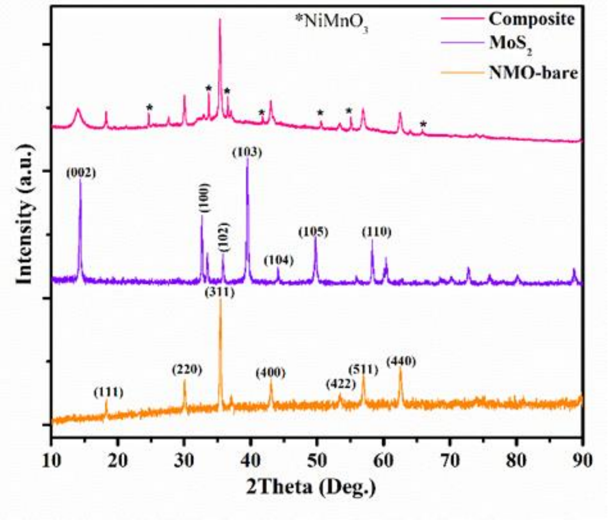

Figure 6.6 XRD pattern of $NiMn_2O_4$-$NiMnO_3$@MoS_2 composite recorded from 10 to 90°.

6.3.2.2 Scanning Electron Microscopy (SEM) and Energy-Dispersive X-ray Spectroscopy (EDX) Analysis

The prepared samples morphology was studied using Scanning Electron Microscopy (SEM) at varied magnifications as shown in Fig. 6.7 (a-d). Figure 6.7 (a) confirms the formation of MoS_2 nanosheets with slight agglomeration. These nanosheets are structured together to form nanoflowers. Figure 6.7 (b) shows the formation of $NiMn_2O_4$ (NMO) nanoparticles with particle size <100 nm. It can be observed that the particles are lengthened and agglomerated due to the synthesis route used. Figure 6.7 (c-d) displays the composite micrographs at two different magnifications. NMO nanoparticles and MoS_2 sheets are embedded together which could be due to the continuous mixing.

Elemental composition is validated via EDX as displayed in Fig. 6.8. From Fig. 6.8 (a-f), it is believed that the composite is uniformly formed and it is consistent with XRD results. The occurrence of elements, Ni, Mn, O, Mo, and S confirms the formation of the $NiMn_2O_4$-$NiMnO_3$@MoS_2 composite. From SEM and EDX results, it can be concluded that the formation of an NMO-MoS_2 composite with a unique structure may help in improving the electrochemical performance as an anode material for LIBs.

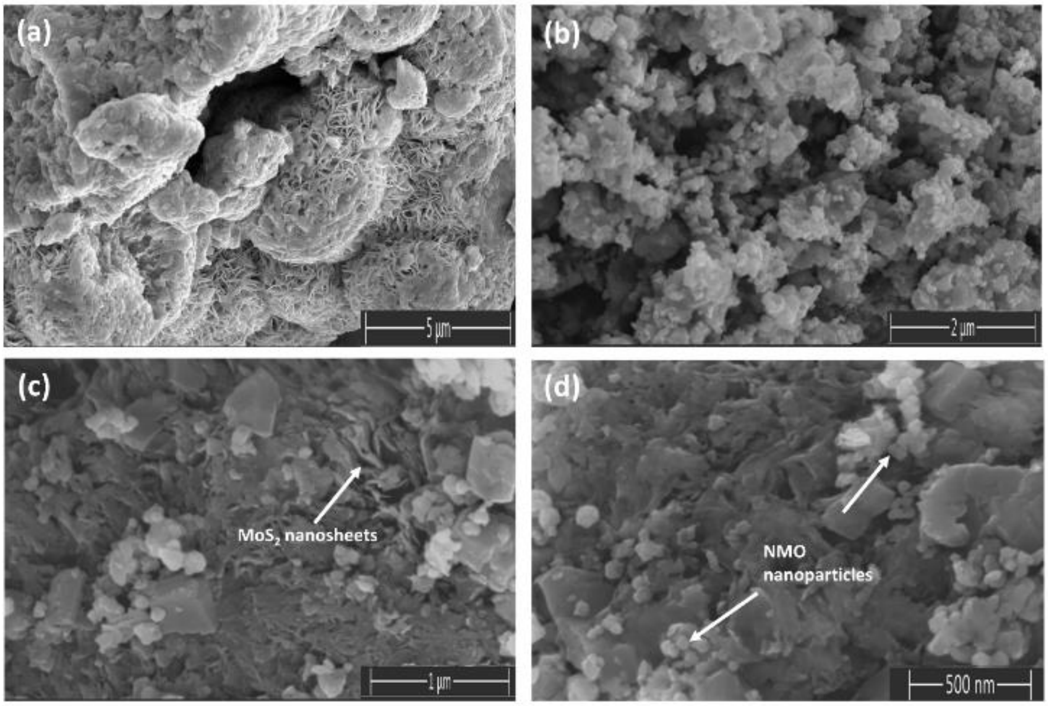

Figure 6.7 SEM images of (a) MoS_2 Nano-sheets, (b) Pristine $NiMn_2O_4$, and (c,d) $NiMn_2O_4$-$NiMnO_3$@MoS_2 composite recorded at different magnifications.

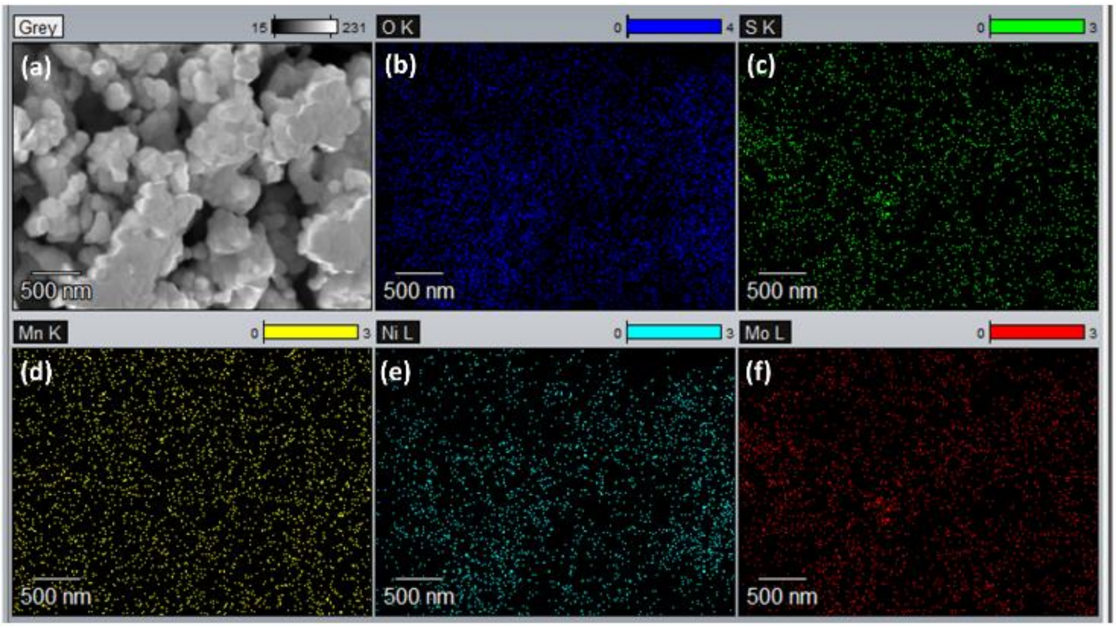

Figure 6.8 EDX mapping of $NiMn_2O_4$-$NiMnO_3$@MoS_2 composite recorded at room temperature.

6.3.2.3 Electrochemical Measurements

Cyclic Voltammetry (CV), and Galvanostatic Charge-Discharge (GCD) profiles were used to examine the electrochemical properties as anode. Figure 6.9 (a) and (b) show the CV curves of 1st and 3rd cycle recorded in the potential limit of 0.01-3.0 V at scan rate of 0.1 mV s^{-1} respectively. During the charging and discharging process, multiple broad peaks of $NiMn_2O_4$ as well as MoS_2 can be observed in Fig. 6.9 (a-b) which shows the redox reaction of the unique $NiMn_2O_4$-$NiMnO_3$@MoS_2 composite structure. The dominant reduction peak at ~0.5V in both cycles depicts the reduction of Ni^{2+} and Mn^{3+} to metallic Ni and Mn respectively [92]. In the third cycle, the strong peak at ~0.96 V, attributes the reduction of Mn^{3+} to Mn^{2+}, while small peak at ~1.8 V leads to the intercalation of Li^+ into MoS_2 and make it Li_2S phase [149]. The broad oxidation peaks at ~1.9 V, ~1.3 V, and ~2.3 V corresponds to the oxidation of Ni, Mn, and de-intercalation of Li$^+$ from Li_2S respectively [92], [149]. Furthermore, with the increased value of current from 3rd cycle, it is evident that the composite shows improved electrochemical performance than a single $NiMn_2O_4$ anode.

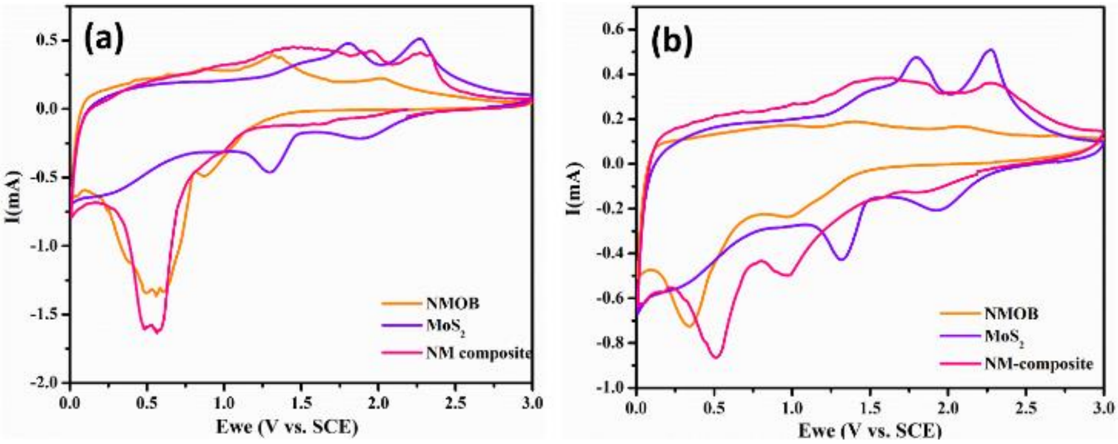

Figure 6.9 Cyclic voltammogram for **(a)** Cycle 1st**, (b)** Cycle 3rd recorded at scan rate of 0.1 mV s^{-1} within the potential limit of 0.01-3.0 V.

To study the Li$^+$ storage behavior, GCD was also attempted on the freshly prepared composite electrodes. Figure 6.10 (a-b) shows the GCD profiles of the composite for the 1st, 2nd, 10th, and 20th cycles with corresponding dQ/dV curves at a high 500 mA g^{-1} current density. The discharge voltage plateaus and reduction/oxidation peaks are consistent with CV curves, indicating the electrochemical reactions between $NiMn_2O_4$, MoS_2, and Li$^+$. From Fig. 6.10 (a-b), three discharge plateaus with corresponding reduction peaks exist at ~1.7, ~1.0, and ~0.5 V further validating that both the active materials i.e., $NiMn_2O_4$ and MoS_2 are involved in the electrochemical kinetics. The composite's 1st, 2nd, 10th, and 20th cycles discharge capacities at 500 mA g^{-1} current density are 1074.36, 1010.35, 734.28, and 517.75 mAh g^{-1} (±8-10) respectively. Figure 6.10 (c) displays the cycling tests of composite and pristine NMO for 300 cycles recorded at 500 mA g^{-1} current density. The composite structure attains discharge capacity of 306.42 mAh g^{-1} even after 300 cycles at such a high current density discharge rate. However, in comparison pristine NMO delivers 246.29 mAh g^{-1} discharge capacity (chapter 4 section 4.2.8.3) which depicts an improved electrochemical performance. This increment in the capacity could be due to the presence of NMO nanoparticles between the spaces of MoS_2 nanosheets and making both faces accessible to electrolyte penetration. Furthermore, MoS_2 nanosheets suppress the volume expansion of NMO nanoparticles due to which it can attain stable cycling performance.

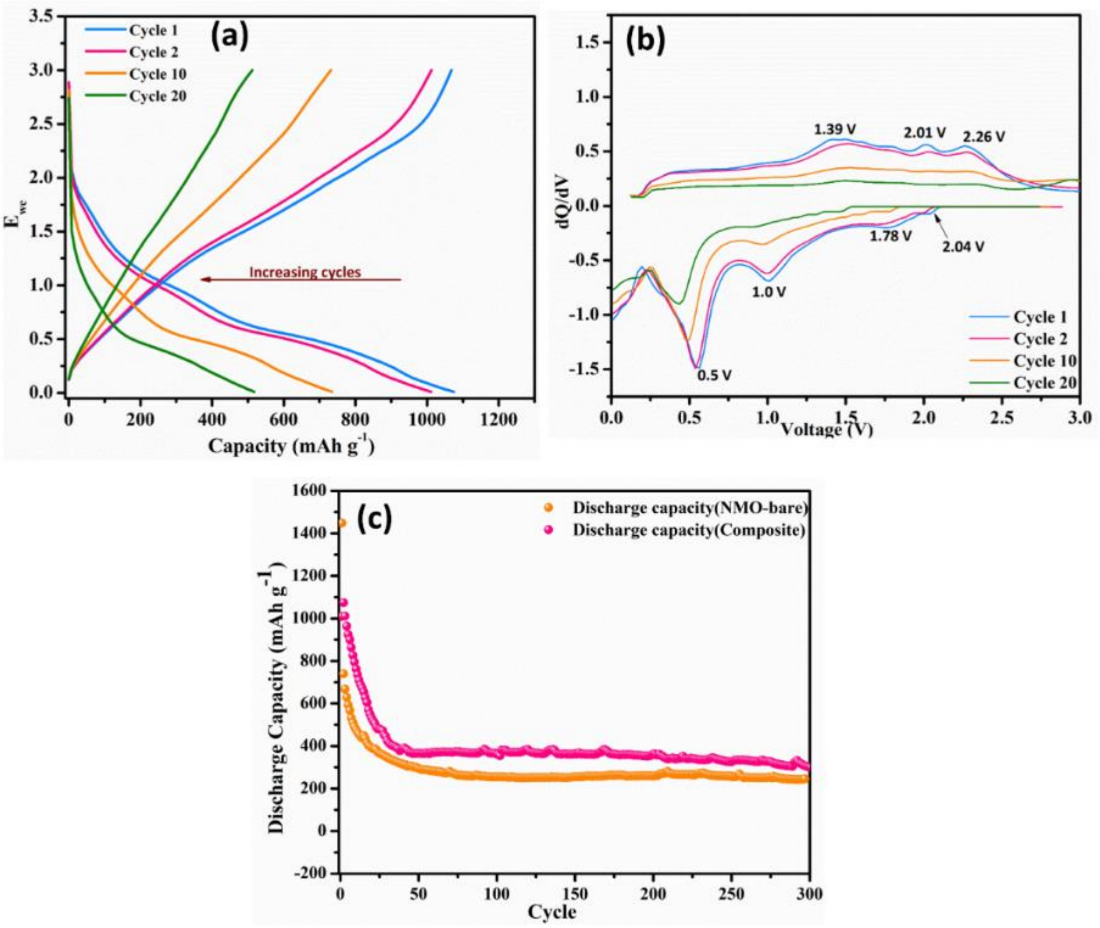

Figure 6.10 **(a)** Galvanostatic charge-discharge (GCD) profiles of 1st, 2nd, 10th, and 20th cycles **(b)** corresponding dQ/dV curves, and **(c)** cycle performance for 300 cycles recorded at 500 mA g^{-1} current density in the potential window ranging between 0.01-3.0 V.

In summary, we have studied the electrochemical performance of $NiMn_2O_4$-$NiMnO_3$@MoS_2 composites as an alternative anode material for LIBs. XRD confirms the unique composite formation with *Fd3m*, $P6_3mmc$, and rhombohedral space group. Morphological studies shows that the NMO nanoparticles are embedded in the MoS_2 nanosheets, however, the slight agglomeration could be seen due to the constant mixing. This unique structure facilitates the Li^+ more effectively and provides more surface area for electrolyte penetration. CV multiple oxidation-reduction peaks at ~2.3 V, ~1.8 V, ~0.5 V are consistent with GCD curves confirm the excellent electrochemical performances of composite which is due to the synergistic effect of both materials.

Chapter 7

Conclusion and Suggestion for future work

In this chapter, the summary of the research work presented in this thesis and future scope for further investigation are included.

7.1 Conclusion

In this study, physicochemical and electrochemical characterizations has been investigated for the spinel type $Li_2ZnTi_3O_8$ and $NiMn_2O_4$ anode materials using low cost and facile synthesis routes. Furthermore, doping, coating and composite studies has been also performed on them to investigate the electrochemical studies.

Initially, spinel type $Li_2ZnTi_3O_8$ (LZTO) and $NiMn_2O_4$ (NMO) pristine materials have successfully synthesized using high-temperature solid-state reaction method. XRD and Rietveld results confirm the formation of pure and crystalline phases of LZTO (space group: $P4_332$) and NMO (space group: Fd3m) without any additional impurities. Morphological studies performed by SEM discloses the unevenly shaped particles of LZTO with an average particle size of 100-200 nm. While in case of NMO, calcination temperature has a major effect on the shape of nanoparticles, NMO_700 and NMO_800 shows agglomerated particle clusters that are uneven in shape. Conductivity measurements shows that the LZTO has higher conductivity ($\sim10^{-8}$ S/cm) in comparison to other Titanate materials. While, NMO shows conductive nature with holding the negative temperature coefficient (NTC) behaviour as temperature varies. Electrochemical studies show that LZTO has a reasonable discharge plateau of about ~0.5 V as well as good capacity. In addition, CV and EIS results of NMO demonstrate that both materials have potential to use as alternative anode materials for LIBs.

To see the effect of synthesis routes, $NiMn_2O_4$ is successfully synthesized using sol-gel and solid-state reaction methods at two distinct temperatures. For NMO material synthesized by sol-gel route, XRD confirms the cubic structure with Fd3m space group. However, at lower calcination temperature in case of sol-gel samples, there is slight presence of $NiMnO_3$ phase. Crystallite size in both cases increases as the calcination temperature increases. SEM, TEM and EDX analysis confirms the hexagonal-shaped nanoparticles irrespective of synthesis routes. The involvement of multiple oxidation states of Mn and Ni in all the samples are also confirmed through the XPS study. BET confirms as the calcination temperature escalates, surface area is also decreases, however, NMOS_700 shows highest surface area which effects its electrochemical performance. AC electrical conductivity results confirmed that the major conduction phenomena that occur in all the samples are due to the grain boundaries. Also, grain resistances diminish as the operating temperature escalates. Among all samples, the sol–gel synthesized mixed phase sample (NMOS_700, $NiMn_2O_4$-$NiMnO_3$) shows excellent cycling performance due to the mixed phase, morphology, and higher surface area which allows more Li^+ interaction. CV and GCD results confirm that as the calcination temperature rises, electrochemical performances reduce irrespective of synthesis routes. Contrary, a ball-milled synthesized single-phase sample at 700 °C (NMOB_700) shows excellent electrical properties and stable cyclability as an anode. Without any additive, in this research work, it is observed that synthesized sample NMOB_700 can attain an excellent discharge and charge capacity of 363 and 343 mAh g^{-1} respectively even after 200 cycles which is near to graphite's theoretical capacity. Furthermore, the sol-gel synthesized sample (NMOS_700), confirms the presence of other phases, doping/coating would be beneficial for the further improvement in electrochemical properties of NMO.

To study the effect of doping, Cr-doped $Li_2ZnTi_3O_8$ samples were synthesized via high-temperature solid-state reaction method. The structural analysis by XRD results reveal that Cr doping does not affect the crystalline nature of pristine LZTO to a certain limit.

Morphological analysis using SEM and TEM displays that as the content of Cr increases in LZTO, it results in spherical polyhedron-shaped facets with reduced size and agglomeration. The activation energy and electronic conductivity are also improved and observed to be 957.1 eV and 7.46 X 10^{-8} S cm^{-1}, respectively, for the 0.3 Cr doped ($Li_2ZnCr_{0.3}Ti_{2.7}O_8$) sample confirms the better electrical performance as compared to pristine LZTO. The electrochemical analysis reveals that $Li_2ZnCr_{0.3}Ti_{2.7}O_8$ shows improved specific capacity of 251.73 ± 4, 184.34 ± 5, 157.42 ± 5, and 119.03 ± 4 mAh g^{-1} for this optimized sample of Cr doping at 0.1C, 0.5C, 1C, and 2C, respectively. Thus, it is reasonable to say that the optimized Cr doping drastically modifies all the parameters of electrodes and improves the electrochemical performance.

To study the effect of 2D materials composite, hydrothermally synthesized MoS_2 was used to further prepare $NiMn_2O_4$-MoS_2 composite. Wet chemical mixing method is used to form the NMO composite. XRD confirms the pure and crystalline phase of MoS_2. However, in composite, the presence of $NiMnO_3$ phase is detected. Raman analysis confirms the mixed phase 2H-1T phase of MoS_2. SEM analysis confirms the formation of nanosheets which are clubbed together to form nanoflowers. Furthermore, NMO-MoS_2 composite shows the presence of NMO nanoparticles as well. EDX confirms the uniform distribution of Mo, S elements in MoS_2 and Ni, Mn, O, Mo, and S elements in NMO-MoS_2 samples. To confirm the electrochemical properties, CV, GCD, rate and cycling test was performed at different test conditions which confirm that after the formation of composite with pristine NMO its performance is improved.

Based on the electrochemical performances of both the samples, it can be concluded that both materials have potential to replace the anode materials for LIBs. However, doping can significantly increase the electrical and electrochemical performance of the LZTO. In case of NMO, material preparation greatly effects the performance of NMO in terms of electrical and electrochemical properties. Therefore, optimization of materials is necessary for the fabrication of LIBs. In both cases, economical, industrial friendly technique were used to further enhance the electrochemical properties of both materials for the application of LIBs as prospective anode.

7.2 Future Scope

- For the future study, the investigation of NMO-MoS_2 composition at different weight ratio need to be further explored to improve the electrochemical and electrical properties of composite formation and see the best optimization as they provide the synergistic effect and more active sites for lithium ion interaction.
- Coating with different materials/carbon in case of LZTO could be also done to improve its electrical conductivity and thereby electrochemical performance.
- Both the optimized materials (LZTO and NMO) can be tested in full cell assembly to see the overall performance of LIBs for commercial applications.

References

References

[1] M. D. Bhatt and C. O'Dwyer, "Recent progress in theoretical and computational investigations of Li-ion battery materials and electrolytes," *Phys. Chem. Chem. Phys.*, vol. 17, no. 7, pp. 4799–4844, Feb. 2015, doi: 10.1039/C4CP05552G.

[2] J. B. Goodenough and K.-S. Park, "The Li-Ion Rechargeable Battery: A Perspective," *J. Am. Chem. Soc.*, vol. 135, no. 4, pp. 1167–1176, Jan. 2013, doi: 10.1021/ja3091438.

[3] M.-K. Tran *et al.*, "A Review of Range Extenders in Battery Electric Vehicles: Current Progress and Future Perspectives," *World Electric Vehicle Journal*, vol. 12, no. 2, Art. no. 2, Jun. 2021, doi: 10.3390/wevj12020054.

[4] C. D. Quilty *et al.*, "Electron and Ion Transport in Lithium and Lithium-Ion Battery Negative and Positive Composite Electrodes," *Chem. Rev.*, vol. 123, no. 4, pp. 1327–1363, Feb. 2023, doi: 10.1021/acs.chemrev.2c00214.

[5] M. Winter and R. J. Brodd, "What Are Batteries, Fuel Cells, and Supercapacitors? (Chem. Rev. 2003, 104, 4245−4269. Published on the Web 09/28/2004.)," *Chem. Rev.*, vol. 105, no. 3, pp. 1021–1021, Mar. 2005, doi: 10.1021/cr040110e.

[6] M. R. Palacín, "Recent advances in rechargeable battery materials: a chemist's perspective," *Chem. Soc. Rev.*, vol. 38, no. 9, pp. 2565–2575, Aug. 2009, doi: 10.1039/B820555H.

[7] W. Chen, J. Liang, Z. Yang, and G. Li, "A Review of Lithium-Ion Battery for Electric Vehicle Applications and Beyond," *Energy Procedia*, vol. 158, pp. 4363–4368, Feb. 2019, doi: 10.1016/j.egypro.2019.01.783.

[8] Y. Liang *et al.*, "A review of rechargeable batteries for portable electronic devices," *InfoMat*, vol. 1, no. 1, pp. 6–32, 2019, doi: 10.1002/inf2.12000.

[9] M. Winter, B. Barnett, and K. Xu, "Before Li Ion Batteries," *Chem. Rev.*, vol. 118, no. 23, pp. 11433–11456, Dec. 2018, doi: 10.1021/acs.chemrev.8b00422.

[10] S. Mahmud *et al.*, "Recent advances in lithium-ion battery materials for improved electrochemical performance: A review," *Results in Engineering*, vol. 15, p. 100472, Sep. 2022, doi: 10.1016/j.rineng.2022.100472.

[11] S. Choi, G. Jung, J. E. Kim, T. Kim, and K. S. Suh, "Lithium intercalated graphite with preformed passivation layer as superior anode for Lithium ion batteries," *Applied Surface Science*, vol. 455, pp. 367–372, Oct. 2018, doi: 10.1016/j.apsusc.2018.05.229.

[12] D. Deng, "Li-ion batteries: basics, progress, and challenges," *Energy Science & Engineering*, vol. 3, no. 5, pp. 385–418, 2015, doi: 10.1002/ese3.95.

[13] Y. Nishi, "Lithium ion secondary batteries; past 10 years and the future," *Journal of Power Sources*, vol. 100, no. 1, pp. 101–106, Nov. 2001, doi: 10.1016/S0378-7753(01)00887-4.

[14] Q. Li, J. Chen, L. Fan, X. Kong, and Y. Lu, "Progress in electrolytes for rechargeable Li-based batteries and beyond," *Green Energy & Environment*, vol. 1, no. 1, pp. 18–42, Apr. 2016, doi: 10.1016/j.gee.2016.04.006.

[15] J. Lu, Z. Chen, F. Pan, Y. Cui, and K. Amine, "High-Performance Anode Materials for Rechargeable Lithium-Ion Batteries," *Electrochem. Energ. Rev.*, vol. 1, no. 1, pp. 35–53, Mar. 2018, doi: 10.1007/s41918-018-0001-4.

[16] P. Roy and S. K. Srivastava, “Nanostructured anode materials for lithium ion batteries,” *J. Mater. Chem. A*, vol. 3, no. 6, pp. 2454–2484, Jan. 2015, doi: 10.1039/C4TA04980B.

[17] R. Mukherjee, R. Krishnan, T.-M. Lu, and N. Koratkar, “Nanostructured electrodes for high-power lithium ion batteries,” *Nano Energy*, vol. 1, no. 4, pp. 518–533, Jul. 2012, doi: 10.1016/j.nanoen.2012.04.001.

[18] R. Holze, “Jung-Ki Park: Principles and applications of lithium secondary batteries,” *J Solid State Electrochem*, vol. 17, no. 8, pp. 2375–2376, Aug. 2013, doi: 10.1007/s10008-013-2094-3.

[19] H. Cheng, J. G. Shapter, Y. Li, and G. Gao, “Recent progress of advanced anode materials of lithium-ion batteries,” *Journal of Energy Chemistry*, vol. 57, pp. 451–468, Jun. 2021, doi: 10.1016/j.jechem.2020.08.056.

[20] M. V. Reddy, G. V. Subba Rao, and B. V. R. Chowdari, “Metal Oxides and Oxysalts as Anode Materials for Li Ion Batteries,” *Chem. Rev.*, vol. 113, no. 7, pp. 5364–5457, Jul. 2013, doi: 10.1021/cr3001884.

[21] N. Mahmood, T. Tang, and Y. Hou, “Nanostructured Anode Materials for Lithium Ion Batteries: Progress, Challenge and Perspective,” *Advanced Energy Materials*, vol. 6, no. 17, p. 1600374, 2016, doi: 10.1002/aenm.201600374.

[22] P. U. Nzereogu, A. D. Omah, F. I. Ezema, E. I. Iwuoha, and A. C. Nwanya, “Anode materials for lithium-ion batteries: A review,” *Applied Surface Science Advances*, vol. 9, p. 100233, Jun. 2022, doi: 10.1016/j.apsadv.2022.100233.

[23] V. Pralong, “Lithium intercalation into transition metal oxides: A route to generate new ordered rock salt type structure,” *Progress in Solid State Chemistry*, vol. 37, no. 4, pp. 262–277, Dec. 2009, doi: 10.1016/j.progsolidstchem.2010.08.002.

[24] R. C. Massé, C. Liu, Y. Li, L. Mai, and G. Cao, “Energy storage through intercalation reactions: electrodes for rechargeable batteries,” *National Science Review*, vol. 4, no. 1, pp. 26–53, Jan. 2017, doi: 10.1093/nsr/nww093.

[25] Y. Yuan, K. Amine, J. Lu, and R. Shahbazian-Yassar, “Understanding materials challenges for rechargeable ion batteries with in situ transmission electron microscopy,” *Nat Commun*, vol. 8, no. 1, Art. no. 1, Aug. 2017, doi: 10.1038/ncomms15806.

[26] N. Nitta and G. Yushin, “High-Capacity Anode Materials for Lithium-Ion Batteries: Choice of Elements and Structures for Active Particles,” *Particle & Particle Systems Characterization*, vol. 31, no. 3, pp. 317–336, 2014, doi: 10.1002/ppsc.201300231.

[27] L. Ji, Z. Lin, M. Alcoutlabi, and X. Zhang, “Recent developments in nanostructured anode materials for rechargeable lithium-ion batteries,” *Energy Environ. Sci.*, vol. 4, no. 8, pp. 2682–2699, Aug. 2011, doi: 10.1039/C0EE00699H.

[28] K. Cao, T. Jin, L. Yang, and L. Jiao, “Recent progress in conversion reaction metal oxide anodes for Li-ion batteries,” *Mater. Chem. Front.*, vol. 1, no. 11, pp. 2213–2242, Oct. 2017, doi: 10.1039/C7QM00175D.

[29] S.-H. Yu, S. H. Lee, D. J. Lee, Y.-E. Sung, and T. Hyeon, “Conversion Reaction-Based Oxide Nanomaterials for Lithium Ion Battery Anodes,” *Small*, vol. 12, no. 16, pp. 2146–2172, 2016, doi: 10.1002/smll.201502299.

[30] R. Malini, U. Uma, T. Sheela, M. Ganesan, and N. G. Renganathan, “Conversion reactions: a new pathway to realise energy in lithium-ion battery—review,” *Ionics*, vol. 15, no. 3, pp. 301–307, Jun. 2009, doi: 10.1007/s11581-008-0236-x.

[31] M. D. Bhatt and J. Y. Lee, “High capacity conversion anodes in Li-ion batteries: A review,” *International Journal of Hydrogen Energy*, vol. 44, no. 21, pp. 10852–10905, Apr. 2019, doi: 10.1016/j.ijhydene.2019.02.015.

[32] D. Saritha, “A concise review on the advancement of anode materials for Li-ion batteries,” *Materials Today: Proceedings*, vol. 19, pp. 726–730, Jan. 2019, doi: 10.1016/j.matpr.2019.07.759.

[33] S. Goriparti, E. Miele, F. De Angelis, E. Di Fabrizio, R. Proietti Zaccaria, and C. Capiglia, “Review on recent progress of nanostructured anode materials for Li-ion batteries,” *Journal of Power Sources*, vol. 257, pp. 421–443, Jul. 2014, doi: 10.1016/j.jpowsour.2013.11.103.

[34] S. Yuan, Q. Lai, X. Duan, and Q. Wang, “Carbon-based materials as anode materials for lithium-ion batteries and lithium-ion capacitors: A review,” *Journal of Energy Storage*, vol. 61, p. 106716, May 2023, doi: 10.1016/j.est.2023.106716.

[35] J. Sun, L. Ye, X. Zhao, P. Zhang, and J. Yang, “Electronic Modulation and Structural Engineering of Carbon-Based Anodes for Low-Temperature Lithium-Ion Batteries: A Review,” *Molecules*, vol. 28, no. 5, Art. no. 5, Jan. 2023, doi: 10.3390/molecules28052108.

[36] S. Zhu and J. Ni, “The Critical Role of Carbon Nanotubes in Bridging Academic Research to Commercialization of Lithium Batteries,” *The Chemical Record*, vol. 22, no. 10, p. e202200125, 2022, doi: 10.1002/tcr.202200125.

[37] L. Li *et al.*, “Carbon-based materials for fast charging lithium-ion batteries,” *Carbon*, vol. 183, pp. 721–734, Oct. 2021, doi: 10.1016/j.carbon.2021.07.053.

[38] S. Choi and G. Wang, “Advanced Lithium-Ion Batteries for Practical Applications: Technology, Development, and Future Perspectives,” *Advanced Materials Technologies*, vol. 3, no. 9, p. 1700376, 2018, doi: 10.1002/admt.201700376.

[39] C. de las Casas and W. Li, “A review of application of carbon nanotubes for lithium ion battery anode material,” *Journal of Power Sources*, vol. 208, pp. 74–85, Jun. 2012, doi: 10.1016/j.jpowsour.2012.02.013.

[40] A. Mauger and C. M. Julien, “Critical review on lithium-ion batteries: are they safe? Sustainable?,” *Ionics*, vol. 23, no. 8, pp. 1933–1947, Aug. 2017, doi: 10.1007/s11581-017-2177-8.

[41] “Recent developments in advanced anode materials for lithium-ion batteries,” *Energy Materials*, vol. 1, no. 1, p. 100003, Sep. 2021, doi: 10.20517/energymater.2021.02.

[42] B. Moradi and G. G. Botte, “Recycling of graphite anodes for the next generation of lithium ion batteries,” *J Appl Electrochem*, vol. 46, no. 2, pp. 123–148, Feb. 2016, doi: 10.1007/s10800-015-0914-0.

[43] X. Meng *et al.*, “Internal failure of anode materials for lithium batteries — A critical review,” *Green Energy & Environment*, vol. 5, no. 1, pp. 22–36, Jan. 2020, doi: 10.1016/j.gee.2019.10.003.

[44] A. Eftekhari, “Low voltage anode materials for lithium-ion batteries,” *Energy Storage Materials*, vol. 7, pp. 157–180, Apr. 2017, doi: 10.1016/j.ensm.2017.01.009.

[45] X. L. Yao *et al.*, “Comparisons of graphite and spinel Li1.33Ti1.67O4 as anode materials for rechargeable lithium-ion batteries,” *Electrochimica Acta*, vol. 50, no. 20, pp. 4076–4081, Jul. 2005, doi: 10.1016/j.electacta.2005.01.034.

[46] M. M. Thackeray, “Spinel Electrodes for Lithium Batteries,” *Journal of the American Ceramic Society*, vol. 82, no. 12, pp. 3347–3354, 1999, doi: 10.1111/j.1151-2916.1999.tb02250.x.

[47] M. M. Thackeray, L. A. de Picciotto, A. de Kock, P. J. Johnson, V. A. Nicholas, and K. T. Adendorff, “Spinel electrodes for lithium batteries — A review,” *Journal of Power Sources*, vol. 21, no. 1, pp. 1–8, Aug. 1987, doi: 10.1016/0378-7753(87)80071-X.

[48] H. Kawai, M. Tabuchi, M. Nagata, H. Tukamoto, and A. R. West, “Crystal chemistry and physical properties of complex lithium spinels Li2MM′3O8 (M=Mg, Co, Ni, Zn; M′=Ti, Ge),” *J. Mater. Chem.*, vol. 8, no. 5, pp. 1273–1280, Jan. 1998, doi: 10.1039/A800234G.

[49] M. Zheng *et al.*, “Hierarchically Nanostructured Transition Metal Oxides for Lithium-Ion Batteries,” *Advanced Science*, vol. 5, no. 3, p. 1700592, 2018, doi: 10.1002/advs.201700592.

[50] G.-N. Zhu, Y.-G. Wang, and Y.-Y. Xia, “Ti-based compounds as anode materials for Li-ion batteries,” *Energy Environ. Sci.*, vol. 5, no. 5, pp. 6652–6667, Apr. 2012, doi: 10.1039/C2EE03410G.

[51] S. Wang, Y. Yang, Y. Dong, Z. Zhang, and Z. Tang, “Recent progress in Ti-based nanocomposite anodes for lithium ion batteries,” *J Adv Ceram*, vol. 8, no. 1, pp. 1–18, Mar. 2019, doi: 10.1007/s40145-018-0292-2.

[52] Z. Chen, I. Belharouak, Y.-K. Sun, and K. Amine, “Titanium-Based Anode Materials for Safe Lithium-Ion Batteries,” *Advanced Functional Materials*, vol. 23, no. 8, pp. 959–969, 2013, doi: 10.1002/adfm.201200698.

[53] T.-F. Yi, T.-T. Wei, Y. Li, Y.-B. He, and Z.-B. Wang, “Efforts on enhancing the Li-ion diffusion coefficient and electronic conductivity of titanate-based anode materials for advanced Li-ion batteries,” *Energy Storage Materials*, vol. 26, pp. 165–197, Apr. 2020, doi: 10.1016/j.ensm.2019.12.042.

[54] A. Farmann, W. Waag, and D. U. Sauer, “Application-specific electrical characterization of high power batteries with lithium titanate anodes for electric vehicles,” *Energy*, vol. 112, pp. 294–306, Oct. 2016, doi: 10.1016/j.energy.2016.06.088.

[55] C. Lin *et al.*, “Li4Ti5O12-based anode materials with low working potentials, high rate capabilities and high cyclability for high-power lithium-ion batteries: a synergistic effect of doping, incorporating a conductive phase and reducing the particle size,” *J. Mater. Chem. A*, vol. 2, no. 26, pp. 9982–9993, Jun. 2014, doi: 10.1039/C4TA01163E.

[56] Y.-R. Wu, J. Pan, S. Ren, Y. Xie, C. Yue, and T.-F. Yi, “Review and prospect of Li2ZnTi3O8-based anode materials for Li-ion battery,” *Ionics*, vol. 25, no. 2, pp. 373–397, Feb. 2019, doi: 10.1007/s11581-018-2818-6.

[57] F. Zhang *et al.*, “Interfacial electrostatic self-assembly in water-in-oil microemulsion assisted synthesis of Li4Ti5O12/Graphene for lithium-ion-batteries,” *Journal of Alloys and Compounds*, vol. 819, p. 153018, Apr. 2020, doi: 10.1016/j.jallcom.2019.153018.

[58] X. Xue, H. Yan, and Y. Fu, “Preparation of pure and metal-doped Li4Ti5O12 composites and their lithium-storage performances for lithium-ion batteries,” *Solid State Ionics*, vol. 335, pp. 1–6, Jul. 2019, doi: 10.1016/j.ssi.2019.02.016.

[59] W. Zhang, J. Ai, Y. Lei, Y. Li, C. Lai, and J. Xie, “Li4Ti5O12-TiO2/C hollow microspheres derived from nanoporous biomass carbon as anode materials for lithium ion batteries,” *Solid State Ionics*, vol. 344, p. 115132, Jan. 2020, doi: 10.1016/j.ssi.2019.115132.

[60] H. Tang, J. Zhu, C. Ma, and Z. Tang, “Lithium cobalt oxide coated lithium zinc titanate anode material with an enhanced high rate capability and long lifespan for lithium-ion batteries,” *Electrochimica Acta*, vol. 144, pp. 76–84, Oct. 2014, doi: 10.1016/j.electacta.2014.08.034.

[61] T. Liu *et al.*, “Improved electrochemical performance of Li2ZnTi3O8 using carbon materials as loose and porous agent,” *Electrochimica Acta*, vol. 259, pp. 28–35, Jan. 2018, doi: 10.1016/j.electacta.2017.10.139.

[62] H. Tang and Z. Tang, “Effect of different carbon sources on electrochemical properties of Li2ZnTi3O8/C anode material in lithium-ion batteries,” *Journal of Alloys and Compounds*, vol. 613, pp. 267–274, Nov. 2014, doi: 10.1016/j.jallcom.2014.06.050.

[63] L. Wang, Z. Meng, H. Wang, X. Li, and G. Zhang, “Effects of TiO2 starting materials on the synthesis of Li2ZnTi3O8 for lithium ion battery anode,” *Ceramics International*, vol. 42, no. 15, pp. 16872–16881, Nov. 2016, doi: 10.1016/j.ceramint.2016.07.184.

[64] A. I. Inamdar *et al.*, “Influence of operating temperature on Li2ZnTi3O8 anode performance and high-rate charging activity of Li-ion battery,” *Ceramics International*, vol. 44, no. 15, pp. 18625–18632, Oct. 2018, doi: 10.1016/j.ceramint.2018.07.087.

[65] W. Cheng *et al.*, “In situ topotactic preparation of porous plate-like Li2ZnTi3O8 as the lithium-ion batteries anode for enhancing electrochemical reaction kinetics and Li+ storage,” *Electrochimica Acta*, vol. 440, p. 141758, Feb. 2023, doi: 10.1016/j.electacta.2022.141758.

[66] Z. Li, Y. Cui, J. Wu, C. Du, X. Zhang, and Z. Tang, “Synthesis and electrochemical properties of lithium zinc titanate as an anode material for lithium ion batteries via microwave method,” *RSC Adv.*, vol. 6, no. 45, pp. 39209–39215, Apr. 2016, doi: 10.1039/C6RA05244D.

[67] P. A. Nikiforova, I. A. Stenina, T. L. Kulova, A. M. Skundin, and A. B. Yaroslavtsev, “Effect of particle size on the conductive and electrochemical properties of Li2ZnTi3O8,” *Inorg Mater*, vol. 52, no. 11, pp. 1137–1142, Nov. 2016, doi: 10.1134/S002016851611011X.

[68] J.-L. Qin, H.-L. Zhu, N. Lun, Y.-X. Qi, and Y.-J. Bai, “Li2ZnTi3O8/C anode with high initial Coulombic efficiency, long cyclic life and outstanding rate properties enabled by fulvic acid,” *Carbon*, vol. 163, pp. 297–307, Aug. 2020, doi: 10.1016/j.carbon.2020.03.029.

[69] Z. Meng, L. Wang, X. Li, G. Zhang, and H. Li, “Synthesis of high performance carbon-coated lithium zinc titanate via an EDTA-assisted route,” *International Journal of Hydrogen Energy*, vol. 42, no. 4, pp. 2177–2186, Jan. 2017, doi: 10.1016/j.ijhydene.2016.09.128.

[70] Y. Ren, P. Lu, X. Huang, J. Ding, and H. Wang, “Enhanced electrochemical properties of Li2ZnTi3O8/C nanocomposite synthesized with phenolic resin as carbon source,” *J Solid State Electrochem*, vol. 21, no. 1, pp. 125–131, Jan. 2017, doi: 10.1007/s10008-016-3330-4.

[71] H. Yang *et al.*, “Boosted electrochemical performance of Li2ZnTi3O8 enabled by ion-conductive Li2ZrO3 concomitant with superficial Zr-doping,” *Journal of Power Sources*, vol. 379, pp. 270–277, Mar. 2018, doi: 10.1016/j.jpowsour.2018.01.064.

[72] J. Qu, Y. Zhao, Y. Ji, Y. Zhu, and T. Yi, “Approaching high-performance lithium storage materials by constructing Li2ZnTi3O8@LiAlO2 composites,” *Int J Miner Metall Mater*, vol. 30, no. 4, pp. 611–620, Apr. 2023, doi: 10.1007/s12613-022-2532-2.

[73] Y. Xu, Z. Hong, L. Xia, J. Yang, and M. Wei, “One step sol–gel synthesis of Li2ZnTi3O8/C nanocomposite with enhanced lithium-ion storage properties,” *Electrochimica Acta*, vol. 88, pp. 74–78, Jan. 2013, doi: 10.1016/j.electacta.2012.10.044.

[74] X. Li, Q. Xiao, B. Liu, H. Lin, and J. Zhao, “One-step solution-combustion synthesis of complex spinel titanate flake particles with enhanced lithium-storage properties,” *Journal of Power Sources*, vol. 273, pp. 128–135, Jan. 2015, doi: 10.1016/j.jpowsour.2014.08.129.

[75] B. Chen, C. Du, Y. Zhang, R. Sun, L. Zhou, and L. Wang, “A new strategy for synthesis of lithium zinc titanate as an anode material for lithium ion batteries,” *Electrochimica Acta*, vol. 159, pp. 102–110, Mar. 2015, doi: 10.1016/j.electacta.2015.01.206.

[76] X. Wang *et al.*, “Nanostructured NiO electrode for high rate Li-ion batteries,” *J. Mater. Chem.*, vol. 21, no. 11, pp. 3571–3573, Mar. 2011, doi: 10.1039/C0JM04356G.

[77] S. A. Needham, G. X. Wang, and H. K. Liu, “Synthesis of NiO nanotubes for use as negative electrodes in lithium ion batteries,” *Journal of Power Sources*, vol. 159, no. 1, pp. 254–257, Sep. 2006, doi: 10.1016/j.jpowsour.2006.04.025.

[78] R. S. Kalubarme, S. M. Jadhav, B. B. Kale, S. W. Gosavi, C. Terashima, and A. Fujishima, “Porous Mn-doped cobalt oxide@C nanocomposite: a stable anode material for Li-ion rechargeable batteries,” *Nanotechnology*, vol. 29, no. 28, p. 285705, May 2018, doi: 10.1088/1361-6528/aac034.

[79] S. Shi, S. Deng, M. Zhang, M. Zhao, and G. Yang, “Rapid Microwave Synthesis of Self-Assembled Hierarchical Mn2O3 Microspheres as Advanced Anode Material for Lithium Ion Batteries,” *Electrochimica Acta*, vol. 224, pp. 285–294, Jan. 2017, doi: 10.1016/j.electacta.2016.12.080.

[80] Y. Zhao *et al.*, “Recent Developments and Understanding of Novel Mixed Transition-Metal Oxides as Anodes in Lithium Ion Batteries,” *Advanced Energy Materials*, vol. 6, no. 8, p. 1502175, 2016, doi: 10.1002/aenm.201502175.

[81] C. Yuan, H. B. Wu, Y. Xie, and X. W. (David) Lou, “Mixed Transition-Metal Oxides: Design, Synthesis, and Energy-Related Applications,” *Angewandte Chemie International Edition*, vol. 53, no. 6, pp. 1488–1504, 2014, doi: 10.1002/anie.201303971.

[82] L. Li *et al.*, “Porous Hollow Superlattice NiMn2O4/NiCo2O4 Mesocrystals as a Highly Reversible Anode Material for Lithium-Ion Batteries,” *Frontiers in*

Chemistry, vol. 6, 2018, Accessed: Jun. 17, 2023. [Online]. Available: https://www.frontiersin.org/articles/10.3389/fchem.2018.00153

[83] L. Ding, X. Zheng, R. Qin, P. Guo, X. Jiang, and M. Zeng, “Facile construction of C and TiO2 surface coating to improve the cycling stability of NiMn2O4 composite electrode materials,” *Materials Letters*, vol. 323, p. 132561, Sep. 2022, doi: 10.1016/j.matlet.2022.132561.

[84] A. Umar *et al.*, “Colloidal synthesis of NiMn2O4 nanodisks decorated reduced graphene oxide for electrochemical applications,” *Microchemical Journal*, vol. 160, p. 105630, Jan. 2021, doi: 10.1016/j.microc.2020.105630.

[85] N. Acharya and R. Sagar, “Structure and electrical properties characterization of NiMn2O4 NTC ceramics,” *Inorganic Chemistry Communications*, vol. 132, p. 108856, Oct. 2021, doi: 10.1016/j.inoche.2021.108856.

[86] J. Ryu, G. Han, J.-P. Lee, Y.-S. Lim, D.-S. Park, and D.-Y. Jeong, “Co and Fe Doping Effect on Negative Temperature Coefficient Characteristics of Nano-Grained NiMn2O4 Thick Films Fabricated by Aerosol-Deposition,” *Journal of Nanoscience and Nanotechnology*, vol. 13, no. 5, pp. 3422–3426, May 2013, doi: 10.1166/jnn.2013.7232.

[87] J. Ryu, D.-S. Park, and R. Schmidt, “In-plane impedance spectroscopy in aerosol deposited NiMn2O4 negative temperature coefficient thermistor films,” *Journal of Applied Physics*, vol. 109, no. 11, p. 113722, Jun. 2011, doi: 10.1063/1.3592300.

[88] J. Huang, W. Wang, X. Lin, C. Gu, and J. Liu, “Three-dimensional sandwich-structured NiMn2O4@reduced graphene oxide nanocomposites for highly reversible Li-ion battery anodes,” *Journal of Power Sources*, vol. 378, pp. 677–684, Feb. 2018, doi: 10.1016/j.jpowsour.2018.01.029.

[89] S. Zhao, H. Li, Z. Jian, Y. Xing, and S. Zhang, “Self-assembled hierarchical porous NiMn2O4 microspheres as high performance Li-ion battery anodes,” *RSC Adv.*, vol. 8, no. 73, pp. 41749–41755, Dec. 2018, doi: 10.1039/C8RA08080A.

[90] W. Kang *et al.*, “High interfacial storage capability of porous NiMn2O4/C hierarchical tremella-like nanostructures as the lithium ion battery anode,” *Nanoscale*, vol. 7, no. 1, pp. 225–231, Dec. 2014, doi: 10.1039/C4NR04031G.

[91] Y. Ma, C.-W. Tai, R. Younesi, T. Gustafsson, J. Y. Lee, and K. Edström, “Iron Doping in Spinel NiMn2O4: Stabilization of the Mesoporous Cubic Phase and Kinetics Activation toward Highly Reversible Li+ Storage,” *Chem. Mater.*, vol. 27, no. 22, pp. 7698–7709, Nov. 2015, doi: 10.1021/acs.chemmater.5b03288.

[92] S. J. Rajoba *et al.*, “Synthesis and Electrochemical Performance of Mesoporous NiMn2O4 Nanoparticles as an Anode for Lithium-Ion Battery,” *Journal of Composites Science*, vol. 5, no. 3, Art. no. 3, Mar. 2021, doi: 10.3390/jcs5030069.

[93] A. B. Yaroslavtsev and I. A. Stenina, “Carbon coating of electrode materials for lithium-ion batteries,” *Surface Innovations*, vol. 9, no. 2–3, pp. 92–110, Apr. 2021, doi: 10.1680/jsuin.20.00044.

[94] H. Tang, L. Zan, W. Mao, and Z. Tang, “Improved rate performance of amorphous carbon coated lithium zinc titanate anode material with alginic acid as carbon precursor and particle size controller,” *Journal of Electroanalytical Chemistry*, vol. 751, pp. 57–64, Aug. 2015, doi: 10.1016/j.jelechem.2015.05.033.

[95] L. Wang, B. Chen, Z. Meng, B. Luo, X. Wang, and Y. Zhao, “High performance carbon-coated lithium zinc titanate as an anode material for lithium-ion batteries,”

Electrochimica Acta, vol. 188, pp. 135–144, Jan. 2016, doi: 10.1016/j.electacta.2015.11.124.

[96] H. Yang *et al.*, “Uniform Surface Modification of Li2ZnTi3O8 by Liquated Na2MoO4 To Boost Electrochemical Performance,” *ACS Appl. Mater. Interfaces*, vol. 9, no. 50, pp. 43603–43613, Dec. 2017, doi: 10.1021/acsami.7b12208.

[97] H. Yang *et al.*, “Li2ZnTi3O8 coated with uniform lithium magnesium silicate layer revealing enhanced rate capability as anode material for Li-Ion battery,” *Electrochimica Acta*, vol. 315, pp. 24–32, Aug. 2019, doi: 10.1016/j.electacta.2019.05.087.

[98] X. Liu, Q. Weng, T. Liu, Z. Tang, and H. Tang, “A Li3PO4 coating strategy to enhance the Li-ion transport properties of Li2ZnTi3O8 anode material for Lithium-ion Battery,” *Electrochimica Acta*, vol. 447, p. 142151, Apr. 2023, doi: 10.1016/j.electacta.2023.142151.

[99] H. Tang, Z. Tang, C. Du, F. Qie, and J. Zhu, “Ag-doped Li2ZnTi3O8 as a high rate anode material for rechargeable lithium-ion batteries,” *Electrochimica Acta*, vol. 120, pp. 187–192, Feb. 2014, doi: 10.1016/j.electacta.2013.12.090.

[100] H. Tang, J. Zhu, Z. Tang, and C. Ma, “Al-doped Li2ZnTi3O8 as an effective anode material for lithium-ion batteries with good rate capabilities,” *Journal of Electroanalytical Chemistry*, vol. 731, pp. 60–66, Oct. 2014, doi: 10.1016/j.jelechem.2014.08.011.

[101] C. Chen, C. Ai, X. Liu, and Y. Wu, “Advanced electrochemical properties of Ce-modified Li2ZnTi3O8 anode material for lithium-ion batteries,” *Electrochimica Acta*, vol. 227, pp. 285–293, Feb. 2017, doi: 10.1016/j.electacta.2016.12.133.

[102] Z. Zhang, R. Xun, Z. Shen, L. Wang, S. Wang, and Z. Meng, “Synthesis of Nb-Doped Li2ZnTi3O8 Anode with Long Cycle Life and Applications in the LiMn2O4/Li2ZnTi3O8 Full Cell,” *ACS Sustainable Chem. Eng.*, vol. 8, no. 7, pp. 2763–2771, Feb. 2020, doi: 10.1021/acssuschemeng.9b06581.

[103] W. Chen *et al.*, “High performance Na-doped lithium zinc titanate as anode material for Li-ion batteries,” *RSC Adv.*, vol. 5, no. 62, pp. 49890–49898, Jun. 2015, doi: 10.1039/C5RA06365E.

[104] C. Jiang, E. Hosono, and H. Zhou, “Nanomaterials for lithium ion batteries,” *Nano Today*, vol. 1, no. 4, pp. 28–33, Nov. 2006, doi: 10.1016/S1748-0132(06)70114-1.

[105] C. Gong, Y.-J. Bai, Y.-X. Qi, N. Lun, and J. Feng, “Preparation of carbon-coated MgFe2O4 with excellent cycling and rate performance,” *Electrochimica Acta*, vol. 90, pp. 119–127, Feb. 2013, doi: 10.1016/j.electacta.2012.11.128.

[106] A. Jain, B. J. Paul, S. Kim, V. K. Jain, J. Kim, and A. K. Rai, “Two-dimensional porous nanodisks of NiCo2O4 as anode material for high-performance rechargeable lithium-ion battery,” *Journal of Alloys and Compounds*, vol. 772, pp. 72–79, Jan. 2019, doi: 10.1016/j.jallcom.2018.09.051.

[107] G. Qin, X. Wu, J. Wen, J. Li, and M. Zeng, “A Core-Shell NiFe2O4@SiO2 Structure as a High-Performance Anode Material for Lithium-Ion Batteries,” *ChemElectroChem*, vol. 6, no. 3, pp. 911–916, 2019, doi: 10.1002/celc.201801839.

[108] T. Ni, Y. Zhong, J. Sunarso, W. Zhou, R. Cai, and Z. Shao, “Optimal hydrothermal synthesis of hierarchical porous ZnMn2O4 microspheres with more

porous core for improved lithium storage performance," *Electrochimica Acta*, vol. 207, pp. 58–65, Jul. 2016, doi: 10.1016/j.electacta.2016.04.098.

[109] "Ionic Conductivity of Li2ZnTi3O8 Single Crystal | Scientific.Net." Accessed: Jun. 26, 2023. [Online]. Available: https://www.scientific.net/KEM.497.26

[110] H. Gao, C. Ma, and B. Sun, "Preparation and characterization of NiMn2O4 negative temperature coefficient ceramics by solid-state coordination reaction," *J Mater Sci: Mater Electron*, vol. 25, no. 9, pp. 3990–3995, Sep. 2014, doi: 10.1007/s10854-014-2118-5.

[111] T. Zhang *et al.*, "Nano-particle assembled porous core–shell ZnMn2O4 microspheres with superb performance for lithium batteries," *Nanotechnology*, vol. 28, no. 10, p. 105403, Feb. 2017, doi: 10.1088/1361-6528/aa5a49.

[112] T. Li, X. Li, Z. Wang, H. Guo, and Y. Li, "A novel NiCo2O4 anode morphology for lithium-ion batteries," *J. Mater. Chem. A*, vol. 3, no. 22, pp. 11970–11975, May 2015, doi: 10.1039/C5TA01928A.

[113] J. Sui *et al.*, "Facile synthesis of MWCNT–ZnFe2O4 nanocomposites as anode materials for lithium ion batteries," *J. Mater. Chem.*, vol. 22, no. 27, pp. 13674–13681, Jun. 2012, doi: 10.1039/C2JM31905E.

[114] Y. Xiao, J. Zai, and X. Qian, "Design and synthesis of the composites of multiporous NiMnO3 micro-nano structure spheres and graphene with alleviated side reaction and enhanced performances as anode materials for lithium ion batteries," *Journal of Alloys and Compounds*, vol. 716, pp. 270–277, Sep. 2017, doi: 10.1016/j.jallcom.2017.04.259.

[115] J. S. Sanchez, A. Pendashteh, J. Palma, M. Anderson, and R. Marcilla, "Synthesis and application of NiMnO3-rGO nanocomposites as electrode materials for hybrid energy storage devices," *Applied Surface Science*, vol. 460, pp. 74–83, Dec. 2018, doi: 10.1016/j.apsusc.2018.02.165.

[116] K. V. Sankar *et al.*, "Studies on the electrochemical intercalation/de-intercalation mechanism of NiMn2O4 for high stable pseudocapacitor electrodes," *RSC Adv.*, vol. 5, no. 35, pp. 27649–27656, Mar. 2015, doi: 10.1039/C5RA00407A.

[117] S. Sahoo, S. Zhang, and J.-J. Shim, "Porous Ternary High Performance Supercapacitor Electrode Based on Reduced Graphene Oxide, NiMn2O4, and Polyaniline," *Electrochimica Acta*, vol. 216, pp. 386–396, Oct. 2016, doi: 10.1016/j.electacta.2016.09.030.

[118] M. S. Song *et al.*, "Solvothermal synthesis of ZnMn2O4 as an anode material in lithium ion battery," *Electrochimica Acta*, vol. 137, pp. 266–272, Aug. 2014, doi: 10.1016/j.electacta.2014.05.126.

[120] B. P. Chandra, R. K. Chandrakar, V. K. Chandra, and R. N. Baghel, "Effect of particle size on activation energy and peak temperature of the thermoluminescence glow curve of undoped ZnS nanoparticles," *Luminescence*, vol. 31, no. 2, pp. 478–486, 2016, doi: 10.1002/bio.2985.

[121] Z. Cui, Y. Xue, L. Xiao, and T. Wang, "Effect of Particle Size on Activation Energy for Thermal Decomposition of Nano-CaCO3," *Journal of Computational and Theoretical Nanoscience*, vol. 10, no. 3, pp. 569–572, Mar. 2013, doi: 10.1166/jctn.2013.2735.

[122] C. Ma and H. Gao, “Preparation and characterization of single-phase NiMn2O4 NTC ceramics by two-step sintering method,” *J Mater Sci: Mater Electron*, vol. 28, no. 9, pp. 6699–6703, May 2017, doi: 10.1007/s10854-017-6361-4.

[123] S. I. Ahmad, A. Rauf, T. Mohammed, A. Bahafi, D. Ravi Kumar, and M. B. Suresh, “Dielectric, impedance, AC conductivity and low-temperature magnetic studies of Ce and Sm co-substituted nanocrystalline cobalt ferrite,” *Journal of Magnetism and Magnetic Materials*, vol. 492, p. 165666, Dec. 2019, doi: 10.1016/j.jmmm.2019.165666.

[124] C. Yang, Y. Qing, K. An, Z. Zhang, L. Wang, and C. Liu, “Facile synthesis of the N-doped graphene/nickel oxide with enhanced electrochemical performance for rechargeable lithium-ion batteries,” *Materials Chemistry and Physics*, vol. 195, pp. 149–156, Jul. 2017, doi: 10.1016/j.matchemphys.2017.04.029.

[125] Y. Yan, Y. Liu, W. Ni, J. Wu, M. Liu, and T. Liu, “Hierarchical Hybrids of Mesoporous NiCo2O4 Needles/Graphene/Carbon Nanotubes with High Performance for Lithium Ion Batteries and Oxygen Reduction Reactions,” *ChemNanoMat*, vol. 2, no. 12, pp. 1077–1085, 2016, doi: 10.1002/cnma.201600259.

[126] X. Yang, Z. Wen, X. Xu, B. Lin, and S. Huang, “Nanosized silicon-based composite derived by in situ mechanochemical reduction for lithium ion batteries,” *Journal of Power Sources*, vol. 164, no. 2, pp. 880–884, Feb. 2007, doi: 10.1016/j.jpowsour.2006.11.010.

[127] R. Saroha, A. K. Panwar, and Y. Sharma, “Physicochemical and electrochemical performance of LiFe1−xNixPO4 (0≤x≤1.0) solid solution as potential cathode material for rechargeable lithium-ion battery,” *Ceramics International*, vol. 43, no. 7, pp. 5734–5742, May 2017, doi: 10.1016/j.ceramint.2017.01.115.

[128] R. Sun, Z. Qin, Z. Li, H. Fan, and S. Lu, “Binary zinc–cobalt metal–organic framework derived mesoporous ZnCo2O4@NC polyhedron as a high-performance lithium-ion battery anode,” *Dalton Trans.*, vol. 49, no. 40, pp. 14237–14242, Oct. 2020, doi: 10.1039/D0DT03132A.

[129] F. Fu *et al.*, “Synthesis of single crystalline hexagonal nanobricks of LiNi1/3Co1/3Mn1/3O2 with high percentage of exposed {010} active facets as high rate performance cathode material for lithium-ion battery,” *J. Mater. Chem. A*, vol. 1, no. 12, pp. 3860–3864, Feb. 2013, doi: 10.1039/C3TA01618H.

[130] Y. Li *et al.*, “Surfactant-assisted solvothermal synthesis of NiCo2O4 as an anode for lithium-ion batteries,” *RSC Adv.*, vol. 7, no. 59, pp. 36909–36916, Jul. 2017, doi: 10.1039/C7RA06172B.

[131] F. Qie and Z. Tang, “Cu-doped Li2 ZnTi3 O8 anode material with improved electrochemical performance for lithium-ion batteries,” *Materials Express*, vol. 4, no. 3, pp. 221–227, Jun. 2014, doi: 10.1166/mex.2014.1166.

[132] R. Saroha, A. K. Panwar, Y. Sharma, P. K. Tyagi, and S. Ghosh, “Development of surface functionalized ZnO-doped LiFePO4/C composites as alternative cathode material for lithium ion batteries,” *Applied Surface Science*, vol. 394, pp. 25–36, Feb. 2017, doi: 10.1016/j.apsusc.2016.09.105.

[133] R. Saroha and A. K. Panwar, “Effect of in situ pyrolysis of acetylene (C2H2) gas as a carbon source on the electrochemical performance of LiFePO4 for

rechargeable lithium-ion batteries," *J. Phys. D: Appl. Phys.*, vol. 50, no. 25, p. 255501, May 2017, doi: 10.1088/1361-6463/aa708c.

[134] C. Chen, C. Ai, and X. Liu, "Ti(III) self-doped Li2ZnTi3O8 as a superior anode material for Li-ion batteries," *Electrochimica Acta*, vol. 265, pp. 448–454, Mar. 2018, doi: 10.1016/j.electacta.2018.01.159.

[135] Q. Zhang, C. Zhang, B. Li, S. Kang, X. Li, and Y. Wang, "Preparation and electrochemical properties of Ca-doped Li4Ti5O12 as anode materials in lithium-ion battery," *Electrochimica Acta*, vol. 98, pp. 146–152, May 2013, doi: 10.1016/j.electacta.2013.03.006.

[136] S. Liu, L. Xiong, and C. He, "Long cycle life lithium ion battery with lithium nickel cobalt manganese oxide (NCM) cathode," *Journal of Power Sources*, vol. 261, pp. 285–291, Sep. 2014, doi: 10.1016/j.jpowsour.2014.03.083.

[137] H. Tang, Y. Zhou, L. Zan, N. Zhao, and Z. Tang, "Long cycle life of carbon coated lithium zinc titanate using copper as conductive additive for lithium ion batteries," *Electrochimica Acta*, vol. 191, pp. 887–894, Feb. 2016, doi: 10.1016/j.electacta.2016.01.141.

[138] L. Wang, Z. Han, Q. Weng, T. Liu, Z. Tang, and H. Tang, "Cyclodextrin polymers as effective water-soluble binder with enhanced cycling performance for Li2ZnTi3O8 anode in lithium-ion batteries," *Ionics*, vol. 28, no. 2, pp. 669–682, Feb. 2022, doi: 10.1007/s11581-021-04374-6.

[139] C. Feng, J. Ma, H. Li, R. Zeng, Z. Guo, and H. Liu, "Synthesis of molybdenum disulfide (MoS2) for lithium ion battery applications," *Materials Research Bulletin*, vol. 44, no. 9, pp. 1811–1815, Sep. 2009, doi: 10.1016/j.materresbull.2009.05.018.

[140] H. Li, W. Li, L. Ma, W. Chen, and J. Wang, "Electrochemical lithiation/delithiation performances of 3D flowerlike MoS2 powders prepared by ionic liquid assisted hydrothermal route," *Journal of Alloys and Compounds*, vol. 471, no. 1, pp. 442–447, Mar. 2009, doi: 10.1016/j.jallcom.2008.03.133.

[141] X. Wang, Z. Zhang, Y. Chen, Y. Qu, Y. Lai, and J. Li, "Morphology-controlled synthesis of MoS2 nanostructures with different lithium storage properties," *Journal of Alloys and Compounds*, vol. 600, pp. 84–90, Jul. 2014, doi: 10.1016/j.jallcom.2014.02.127.

[142] O. Samy, S. Zeng, M. D. Birowosuto, and A. El Moutaouakil, "A Review on MoS2 Properties, Synthesis, Sensing Applications and Challenges," *Crystals*, vol. 11, no. 4, Art. no. 4, Apr. 2021, doi: 10.3390/cryst11040355.

[143] Y. Tian *et al.*, "Microwave-assisted synthesis of 1T MoS2/Cu nanowires with enhanced capacity and stability as anode for LIBs," *Chemical Engineering Journal*, vol. 374, pp. 429–436, Oct. 2019, doi: 10.1016/j.cej.2019.05.174.

[144] X. Lin *et al.*, "In-situ growth of 1T/2H-MoS2 on carbon fiber cloth and the modification of SnS2 nanoparticles: A three-dimensional heterostructure for high-performance flexible lithium-ion batteries," *Chemical Engineering Journal*, vol. 356, pp. 483–491, Jan. 2019, doi: 10.1016/j.cej.2018.08.208.

[145] J. Zhu, Y. Ding, Z. Ma, W. Tang, X. Chen, and Y. Lu, "Recent Progress on Nanostructured Transition Metal Oxides As Anode Materials for Lithium-Ion Batteries," *J. Electron. Mater.*, vol. 51, no. 7, pp. 3391–3417, Jul. 2022, doi: 10.1007/s11664-022-09662-z.

[146] M. Kr. Singh *et al.*, “Diffusion mechanism and electrochemical investigation of 1T phase Al–MoS2@rGO nano-composite as a high-performance anode for sodium-ion batteries,” *Chemical Engineering Journal*, vol. 454, p. 140140, Feb. 2023, doi: 10.1016/j.cej.2022.140140.

[147] S. Duraisamy, A. Ganguly, P. K. Sharma, J. Benson, J. Davis, and P. Papakonstantinou, “One-Step Hydrothermal Synthesis of Phase-Engineered MoS2/MoO3 Electrocatalysts for Hydrogen Evolution Reaction,” *ACS Appl. Nano Mater.*, vol. 4, no. 3, pp. 2642–2656, Mar. 2021, doi: 10.1021/acsanm.0c03274.

[148] S. Venkateshwaran, T. Partheeban, M. Sasidharan, and S. M. Senthil Kumar, “Mesoporous Silica Template-Assisted Synthesis of 1T-MoS2 as the Anode for Li-Ion Battery Applications,” *Energy Fuels*, vol. 35, no. 3, pp. 2683–2691, Feb. 2021, doi: 10.1021/acs.energyfuels.0c03296.

[149] P. Sun, W. Zhang, X. Hu, L. Yuan, and Y. Huang, “Synthesis of hierarchical MoS2 and its electrochemical performance as an anode material for lithium-ion batteries,” *J. Mater. Chem. A*, vol. 2, no. 10, pp. 3498–3504, Feb. 2014, doi: 10.1039/C3TA13994H.

[150] C. P. Veeramalai, F. Li, H. Xu, T. W. Kim, and T. Guo, “One pot hydrothermal synthesis of graphene like MoS2 nanosheets for application in high performance lithium ion batteries,” *RSC Adv.*, vol. 5, no. 71, pp. 57666–57670, Jun. 2015, doi: 10.1039/C5RA07478A.

[151] S. Wang *et al.*, “Hydrothermal Synthesis of Molybdenum Disulfide for Lithium Ion Battery Applications,” *Chinese Journal of Chemical Engineering*, vol. 18, no. 6, pp. 910–913, Dec. 2010, doi: 10.1016/S1004-9541(09)60147-6.

[152] Y. Liu *et al.*, “Synthesis of severe lattice distorted MoS2 coupled with hetero-bonds as anode for superior lithium-ion batteries,” *Electrochimica Acta*, vol. 262, pp. 162–172, Feb. 2018, doi: 10.1016/j.electacta.2018.01.023.

[153] M. Wang, G. Li, H. Xu, Y. Qian, and J. Yang, “Enhanced Lithium Storage Performances of Hierarchical Hollow MoS2 Nanoparticles Assembled from Nanosheets,” *ACS Appl. Mater. Interfaces*, vol. 5, no. 3, pp. 1003–1008, Feb. 2013, doi: 10.1021/am3026954.

[154] U. K. Sen and S. Mitra, “High-Rate and High-Energy-Density Lithium-Ion Battery Anode Containing 2D MoS2 Nanowall and Cellulose Binder,” *ACS Appl. Mater. Interfaces*, vol. 5, no. 4, pp. 1240–1247, Feb. 2013, doi: 10.1021/am3022015.

[155] W. Wu, J. Wang, Q. Deng, H. Luo, Y. Li, and M. Wei, “Low crystalline 1T-MoS2@S-doped carbon hollow spheres as an anode material for Lithium-ion battery,” *Journal of Colloid and Interface Science*, vol. 601, pp. 411–417, Nov. 2021, doi: 10.1016/j.jcis.2021.05.146.